| | |
|---|---|
| **Titre:** Title: | Investigation of Dipole Sources in the Biceps Brachii as Upper Limb Position is Modified |
| **Auteur:** Author: | Peyman Aghajamaliaval |
| **Date:** | 2015 |
| **Type:** | Mémoire ou thèse / Dissertation or Thesis |
| **Référence:** Citation: | Aghajamaliaval, P. (2015). Investigation of Dipole Sources in the Biceps Brachii as Upper Limb Position is Modified [Master's thesis, École Polytechnique de Montréal]. PolyPublie. https://publications.polymtl.ca/1919/ |

## Document en libre accès dans PolyPublie
Open Access document in PolyPublie

| | |
|---|---|
| **URL de PolyPublie:** PolyPublie URL: | https://publications.polymtl.ca/1919/ |
| **Directeurs de recherche:** Advisors: | Michael J. Corinthios, & Pierre A. Mathieu |
| **Programme:** Program: | génie électrique |

UNIVERSITÉ DE MONTRÉAL

INVESTIGATION OF DIPOLE SOURCES IN THE BICEPS BRACHII AS
UPPER LIMB POSITION IS MODIFIED

PEYMAN AGHAJAMALIAVAL

DÉPARTEMENT DE GÉNIE ÉLECRIQUE

ÉCOLE POLYTECHNIQUE DE MONTRÉAL

MÉMOIRE PRÉSENTÉ EN VUE DE L'OBTENTION

DU DIPLÔME DE MAÎTRISE

(GÉNIE ÉLECTRIQUE)

AOÛT 2015

UNIVERSITÉ DE MONTRÉAL


ÉCOLE POLYTECHNIQUE DE MONTRÉAL



Cette thése intitulée:



# INVESTIGATION OF DIPOLE SOURCES IN THE BICEPS BRACHII AS UPPER LIMB POSITION IS MODIFIED



présenté par : AGHAJAMALIAVAL Peyman

en vue de l'obtention du diplôme de : Maîtrise ès sciences appliquées


 a été dûment accepté par le jury d'examen constitué de :

M. BRAULT Jean-Jules, Ph. D., président

M. CORINTHIOS Michael, Ph. D., membre et directeur de recherche

M. MATHIEU A. Pierre, Ph. D., membre et codirecteur de recherche

M. SAUVÉ Rémy, Ph. D., membre

# DEDICATION

*Dedicated to my lovely parents Nahid and Latif, my beloved soul mate Eli,*

*and my fantastic grandmas Soofi and Fezeh.*

# ACKNOWLEDGEMENTS

I would like to express my deepest gratitude and appreciation to my director of research Professor Michael J. Corinthios and my co-director Professor Pierre A. Mathieu for their continuous supports, contribution, guidance, and constant encouragement throughout this research work. It has been an honour and pleasure to work with them. Their immense patience and incredible meticulous consideration have left indelible effect on me. The financial support through this research is also greatly acknowledged.

I would also like to express my deepest gratefulness to Professor Michel Bertrand for his supports, guidance, contribute, and encouragement.

I am most grateful to the members of my committee, Professor Jean-Jules Brault and Professor Rémy Sauvé for their time, encouragement, and expertise throughout this project.

My special thanks to the faculty and staff of Electrical Department at Polytechnique de Montréal and Institute of Biomedical Engineering of Université de Montréal who have been always helpful and co-operative.

I would like to thank Etienne Bouffard-Cloutier and Pierre-Yves Sirois C., students from Polytechnique who worked at EMG lab with me during their summer internship. I also gratefully acknowledge Jean L. Laurier for his contribution in our weekly meetings throughout this project.

Last but not least, I would like to thank my parents, Nahid Vafai and Latif Aghajamaliaval, and my beloved wife Elmira for their endless support, encouragement and prayers. Without their support this work would not have been possible.

# RÉSUMÉ

Pour une personne ayant subi une amputation au niveau du bras, les prothèses myoélectriques modernes offrent la possibilité de reproduire plusieurs mouvements nécessaires dans la vie quotidienne. Pour ce faire, plusieurs signaux de contrôle sont toutefois nécessaires pour pouvoir en bénéficier pleinement. Dans la partie supérieure du bras, le biceps brachial (BB) est un muscle important où on trouve sur sa surface intérieure des divisions suggérant la présence de 3 compartiment dans le chef court (SH) et 3 dans le chef long (LH). Comme chacun d'eux est innervée par une branche nerveuse, il est possible que ces compartiments puissent être activés individuellement permettant ainsi d'obtenir jusqu'à six signaux de contrôle pour se servir d'une prothèse myoélectrique. Pour explorer cette possibilité, quelqu'un de notre groupe (NN) avait il y a 3 ans, fait des enregistrements de 10 signaux électromyographiques (EMG) obtenus au-dessus du biceps droit de jeunes sujets. Ces derniers, en position assise ou debout avec la main en différentes positions, avaient mis leur biceps en contraction isométrique et isotonique. Pour chaque position testée, la valeur quadratique moyenne (RMS) de chacun des 10 signaux obtenus lors d'une contraction a été calculée à leur moyenne obtenue à partir de 3 essais consécutifs. Avec une méthode de détection de crêtes parmi chaque ensemble de 10 valeurs RMS, ont a associé la présence de dipôles à l'intérieur du biceps. Pour vérifier comment les caractéristiques des dipôles identifiés permettaient de reproduire les résultats expérimentaux, des simulations ont été réalisées avec le logiciel COMSOL. Le bras a été modélisé par un cylindre à 4 couches concentriques représentant la peau, la couche de graisse, le tissu musculaire et l'os et la conductivité de ces tissus à 100 Hz a été utilisée dans les calculs de simulation et l'anisotropie du tissu musculaire a été prise en considération. Faisant l'hypothèse que les 6 compartiments à l'intérieur du biceps sont de surface égale et séparés par des parois verticales, la plupart des dipôles identifiés se sont retrouvés dans un de ces compartiments ou à la démarcation entre deux d'entre eux. Quelques dipôles se sont toutefois retrouvés à l'extérieur des contours du biceps. En position assise, les dipôles se sont retrouvés plus fréquemment dans les compartiments du chef court (SH) alors qu'en positon debout, ils étaient plus nombreux à se retrouver dans ceux du chef long (LH). Les changements dans la position de la main ne semblent pas induire un déplacement important de la position des dipôles. Dans les positions testées, il ne semble pas possible d'activer un seul compartiment du biceps à la fois. On espère que des résultats plus satisfaisants pourront être obtenus avec des données obtenues dans d'autres positions expérimentales qui n'ont pas encore été analysées. Sinon, il sera nécessaire

de recourir à un traitement de signal afin d'obtenir du biceps plus que les deux signaux de contrôle: un pour chacun des deux chefs de ce muscle.

**Mots-clés:** biceps brachial, compartiments, EMG, dipôles, problème direct.

# ABSTRACT

For an upper arm amputee person, modern myoelectric prostheses offer the possibility to produce many movements needed in a daily life. To do this, various control signals are needed to be able to fully take benefit from them. In the upper arm, the biceps brachii (BB) is an important muscle where in its inner surface, divisions suggest the presence of 3 compartment in its short head (SH) and 3 in its long head (LH). Since each of them is individually innervated by a nerve branch, there is a possibility that they could be activated independently to produce up to 6 control signals for operating a myoelectric prosthesis. To explore that possibility, three years ago, someone of our group (NN) collected 10 electromyographic (EMG) signals across the right biceps of 10 healthy young subjects. While either seated or standing up with the arm in different positions, they produced isometric and isotonic contractions of their biceps. For each tested position, the mean square (RMS) of each of the 10 signals obtained during a contraction was calculated a mean set was obtained from three consecutive contractions. With a peak detection method, the presence of dipoles within the biceps was associated to each mean set of 10 RMS values. To check how well the identified dipoles could reproduce the experimental data, simulations were done with COMSOL. In the software, the upper arm was modelled as a cylinder composed of 4 concentric layers representing the skin, the fat layer, muscular tissue and the bone and conductivity values of these tissues at 100 Hz was used in the simulations; anisotropy of muscle tissue was also considered. Assuming that the 6 compartments inside the biceps were of equal surface and separated by a vertical wall, most of the dipoles were found to be located within one compartment of the biceps or at the border of two adjacent ones. Some of the dipoles were found outside the biceps but in its vicinity. In the seated position, dipoles were more often located in a compartment of the short head (SH) while in the standing up position dipoles were most often in the long head (LH). Changes in hand position does not seem to significantly alter the dipole positions within each head. For the seating and standing up analyzed positions, it does not seem possible to individually activate a compartment. More satisfying results may be obtained from other data collected in other experimental positions that have not yet been analyzed. If this does not happen, some signal processing will be needed to extract more than one control signal from its SH and from its LH.

**Keywords:** Biceps Brachii, compartments, EMG, dipoles, forward problem

# TABLE OF CONTENTS

# LIST OF TABLES

# LIST OF FIGURES

# LIST OF SYMBOLS AND ABBREVIATIONS

| | |
|---|---|
| AP | Action potential |
| API | Application programing interfaces |
| BB | Biceps brachii |
| BF | Biceps femoris |
| CAD | Computed-aided design |
| DOF | Degrees of freedom |
| ECRL | Extensor carpi radialis longus |
| FCR | Flexor carpi radialis |
| IAP | Intracellular action potentials |
| L&T | Lambin and Troquet |
| LG | Lateral gastrocnemius |
| LH | Long head |
| MG | Medial gastrocnemius |
| MRI | Magnetic resonance image |
| MU | Motor unit |
| MUAP | Motor unit action potential |
| MUAPTMUAP train | |
| MUP | Motor unit potentials |
| MVC | Maximum voluntary contraction |
| PCA | Principal component analysis |
| PDE | Partial differential equation |
| PM | Pectoralis major |
| PMNB | Primary muscle nerve branches |
| RMS | Root mean square |
| SFAP | Single fiber action potential |
| SH | Short head |
| TA | Tibialis anterior |
| TB | Triceps brachialis |
| TFL | Tensor fasciae latae |

# CHAPTER 1   INTRODUCTION

Our upper limb is very important in our daily life activities and loosing part of it has a large impact on our regular affairs: besides physical discomfort it also affects mental health. Due to an accident, a disease or a war consequence, amputation may become necessary. The best approach to recover some of the lost functions is the use of a prosthesis. While body-powered prosthesis are simple to operate (through the bending of back muscles or the elevation of the shoulder), the number of different movements that can be produced with them is rather restricted. In other types, such as the myoelectric prostheses, the electrical signal electromyogram (EMG) collected above contracted muscles are used to control them. Within such prostheses, a battery is feeding electronic circuits which are used to process the EMG signal and activate motors by which movements are produced. In general, two muscles are used to produce a movement: one muscle is used to clench the fist while the other one serves to open it.

Modern prostheses are now capable of many degrees of freedom (DOFs) and thus require the availability of many control signals in order to use them at their full capabilities. Because an amputation reduces the number of muscles available to control a prosthesis, signal processing is frequently used for multiplying the number of control signals that can be obtained from the limited number of available muscles. In addition to this technical approach, we consider that the presence of compartments in some large skeletal muscles offers a great opportunity to increase the number of control signals that an amputee person could use to operate a performing prosthesis.

Among such large muscles, we focused on the biceps brachii (BB) for the following reasons: 1) it is an important muscle involved in the control of the forearm; 2) anatomically, from cadaver dissections, the presence of 6 compartments each innervated by a nerve branch was observed on its inner surface (part close to the humerus bone); 3) physiologically, activity within part of the muscle was associated to a particular movement of the limb. It thus appears possible that each of those compartments they could be individually controlled for the production of 6 control signals.

Interested in the physical readaptation of upper-limb amputee persons and considering the recent increased availability of myoelectric prostheses with many DOFs, our group began few years ago to investigate activity of the biceps under various conditions. Our research hypothesis is at the effect that the biceps compartments could be individually put under tension when the muscle is appropriately solicited.

In a previous master degree research project, 5 pairs of equidistant electrodes were placed across the biceps short head (SH) and 5 others across its long head (LH). EMG signals of 5 s long were recorded across the right biceps of 5 healthy females and 5 healthy males (20 to 33 year old) while they performed various contractions. In our present project we analyzed the data collected when the subjects were either in sitting or standing-up positions with their hand was pronated, in neutral position or supinated.

Our goal was to find a relation between the 10 root mean square (RMS) values distribution obtained from the 10 surface recorded signals and the presence of electric dipoles within the muscular tissue which could have been at the origin of the recorded potentials. To start solving this inverse problem, a previously designed peak fitting method was used to find an initial 2D evaluation of the dipoles characteristics (number, position, and relative intensity). With those information, the COMSOL software was used to build a finite element model (FEM) of the upper arm. AC/DC module and stationary (or frequency) solvers were used in COMSOL and some characteristics of the upper arm of each subject (circumference, length of the muscle) were also considered to model the upper arm alike a cylinder. Using 'livelink for MATLAB', which works as a local server, the simulated results then were sent to MATLAB software for postprocessing. Comparison was made between amplitude of the simulated results and the experimental RMS data. To validate our modelling approach, literature results aiming at dipole location within a cylinder were simulated with $z$-oriented, $\rho$-oriented and $\varphi$-oriented dipoles.

In our simplest model (1-layer), only isotropic muscle tissue was filling the whole cylinder and simulations were carried out on a 3D model. The obtained result of simulations being somewhat different from the experimental RMS values, a more realistic 4-layer model was developed. It consisted of 4 concentric cylinders representing the skin, the subcutaneous fat, the muscular tissue

and the humerus bone. Various 4-layer models were experimented by varying the thickness of the layers and by introducing the muscular anisotropy. To illustrate the results, within a horizontal slice of the upper arm at the level where electrodes were placed in the experimental data acquisition, the biceps with its 2 heads was represented as a semicircle. Without any published information on the shape of the 6 compartments and their respective position within the biceps, we assumed that they had the same area, and were vertically separated within the biceps semicircle: 3 compartments making the SH and 3 others making the LH.

Following this introduction chapter, the literature review provides some information on upper limb and the biceps physiology which is followed by the available information on the biceps compartments anatomy. Information is provided on modern myoelectric prostheses capable of producing many movements as long as the required control signals are available. It is to increase that number of control signals that we are investigating how to individually activate the 6 compartments of the biceps. To study activity in those compartments, we associated the presence of dipoles to the 10 signals that have been recorded across the biceps. This is why various articles related to the direct and inverse problems in electrophysiology are presented in this chapter.

In the third chapter, methods for the EMG signal acquisition and for the peak fitting method to initially located dipoles from the experimental data are presented. Our simulations having been done with COMSOL, the most important screen displays are briefly presented as well as the communication between the software and Matlab. The different upper arm models we considered are briefly described as well as the scaling factor to display the results. In the Results chapter, initial simulations were used to validate the use of COMSOL in our project. This being done, we identified the most appropriate arm model to use for the analysis of our 10 subjects data. Dipoles were found more frequently in the short head (SH) of the biceps when subjects were seating while more dipoles were observed in the long head (LH) for the standing up position. In the Discussion, limitation of the arm model as well as the hypothesized distribution of the compartments within the idealized biceps contours are presented. In the Conclusion, orientations are suggested for the continuation of that research on how to increase the number of control signals that would permit an amputee person to be again self-sufficient in most of his/her daily living activities.

# CHAPTER 2   LITTERATURE REVIEW

This chapter has two main sections. In the first section, anatomy of upper arm with mentioning its significant muscles and bones, muscle component, muscle contraction with its different types, various types of recording myoelectric signals, and conductivity of different tissues will consider briefly. In the second section, articles on analytical approach for direct and inverse methods as well as finite element modelling will be reviewed.

## Anatomy of the upper arm

A motion result when a skeletal muscle crossing an articulation is contracted. Articulations are joints where movements between two bones occur. At the upper limb, the bone linking the shoulder to the elbow articulation is the humerus while at the elbow joint, the radius and the ulna bones are in contact with the humerus (Figure 2.1A). The elbow articulation is composed of three joints: the, the humeroulnar and the radioulnar and the synovial joint (Figure 2.1B). The first two joints are involved in the elbow flexion and extension and the third one is associated to the wrist position which could go from pronation to supination (Figure 2.1C). The radius contributes mainly to the wrist joint while the ulna plays the same role for the elbow joint [1]. The radius moves the hand around a center of the rotation established by the ulna. Reference positions of the hand are pronation neutral position and supination (Figure 2.1C). In supination, radius is parallel to the ulna while to be   pronated, the radius turns around the ulna at both elbow and wrist joints and those two bones become crossed [2].

Six upper arm muscles are attached to bones (Figure 2.2): the deltoid gives a rounded shape to the shoulder with its three portions [4, 5]: the posterior one extend the humerus backward while its anterior portion moves it forward. The triceps brachialis (TB), located in the posterior section of the arm is the primary extensor of the elbow and also links the scapula and humerus to the ulna. Without attachment to the radius, TB plays no role in pronation and supination of the forearm [4, 5] which is not the case for the biceps brachii (BB) since part of its insertion is on the radius.
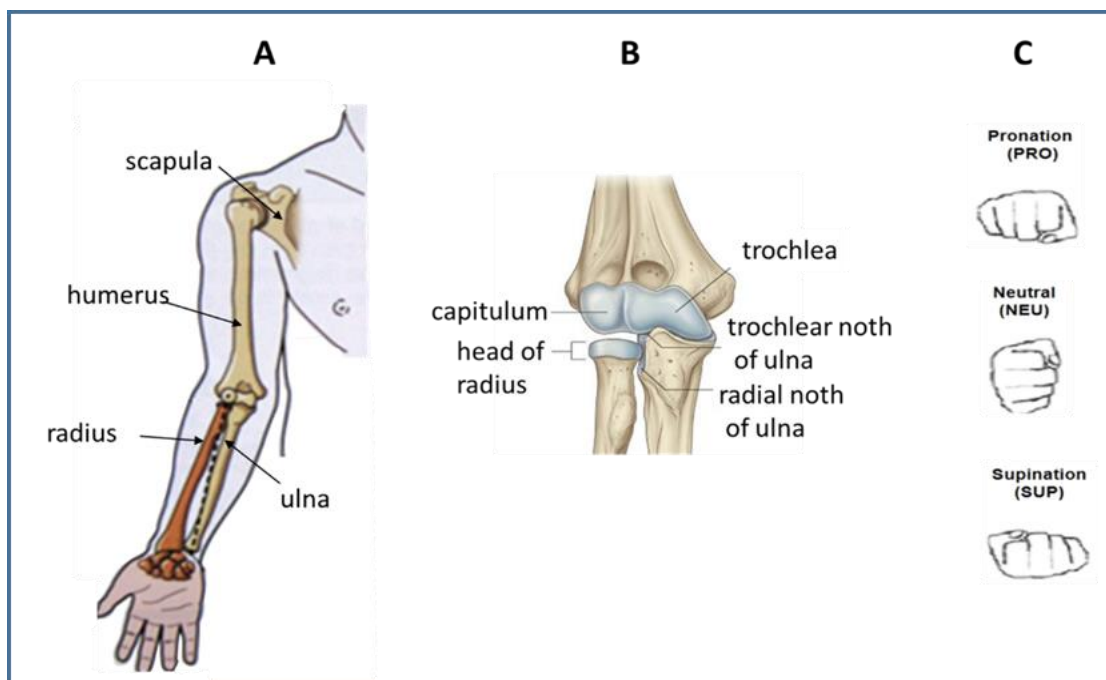
Figure 2.1: **A:** Upper limb bones (Neumann, p.187) [3]. **B:** Details on the elbow articulation. (from:https://www.studyblue.com/notes/note/n/anatomy-lecture-6-elbow-jointforearm/deck/1115 2529). **C:** Illustration of the hand in pronation (top), in neutral position (middle) and in supination (bottom).
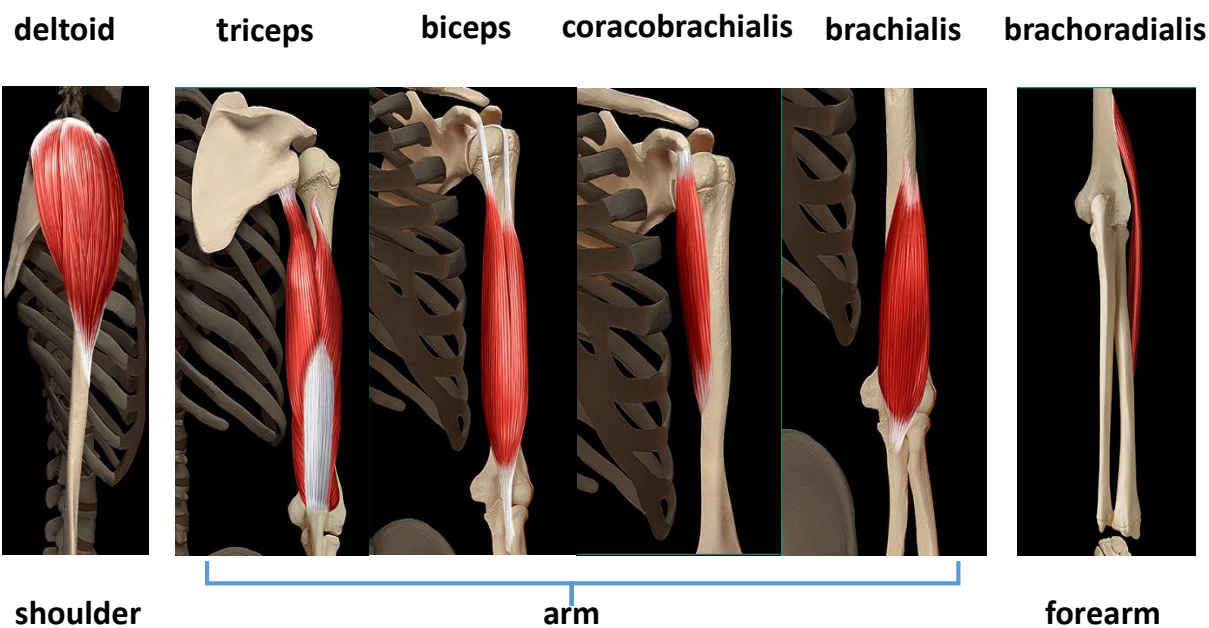


Figure 2.2: Upper arm muscles attached to the humerus and forearm bones. (Adapted from: Upper Limb Musculoskeletal Anatomy; a CD from Masson, 2003).

The brachialis (BR) is the strongest elbow flexor in every position of the forearm. Located underneath the BB it only links the humerus to the ulna and thus does not assist in pronation or The BB is the main flexor of the forearm. The small coracobrachialis (CBR) with its vertical line of pull near the shoulder joint contributes to stabilize the humerus head against the glenoid fossa [4] and to flex and abduct the arm [5]. supination of the forearm [4, 5]. The brachoradialis (BRR) facilitates the elbow flexion while the forearm is in neutral position and, although attached to the radius, does not play an important role in forearm pronation and supination.

Skeletal muscles represents 40-45% of the body mass and are made of a great quantity of muscle fibers. In adults, the diameter of a muscle fiber ranges between 10 to 100 µm and its length can reach 20 cm. Those muscles are attached to the skeleton by tendons which are connective tissues made of bundles of collagen fibers. Generally, muscle fibers are shorter than the length of a muscle but in some muscles, fibers extend throughout the entire length of the muscle. Figure 2.3 illustrates components of the biceps brachii (BB) with its tendons.
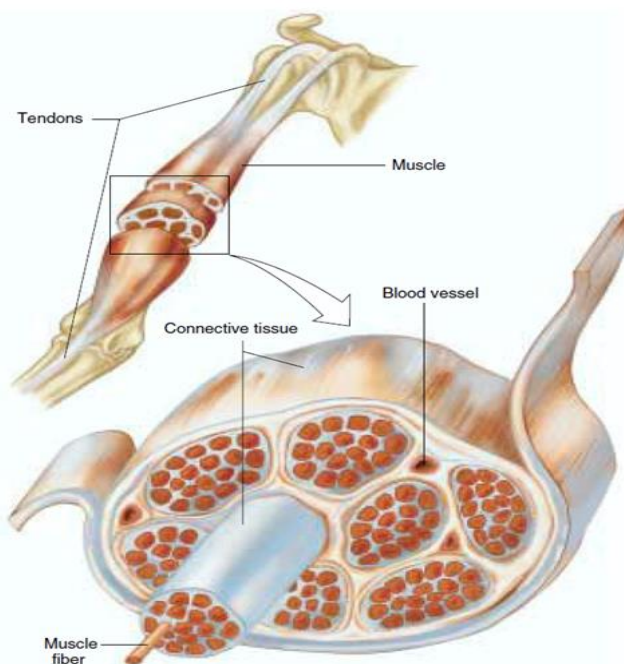


Figure 2.3: Illustration of the biceps brachii with its proximal tendon (at the shoulder level) and its distal one below the elbow joint. Connective tissues are enveloping the muscle as a whole, enveloping groups of muscles called fascicles (as the one shown in front of others) and enveloping each muscle fiber individually within a fascicle (from Vander et al. "Human Physiology: The Mechanism of Body Function", edition 8th, p.293) [6].

A muscle fiber is made of many cylindrical bundles, named myofibrils, extending all along the fiber length and fused within the tendons of the muscle. Myofibrils present repeating regular zones of black vertical lines separated by pale and darker zones which are shown as yellow and red in Figure 2.4A, The structure between 2 black vertical lines constitutes a sarcomere the length of which is 2-3 µm at rest. A myofibril is thus composed of many sarcomeres in series. The sarcomere pattern is due to 2 kinds of filaments: thick ones called myosin and thin ones called actin. The thick filaments are situated in the centre of every sarcomere with a parallel arrangement which leads to a dark and wide band called A-band. As shown in Figure 2.4B, the thin filaments are located at each end of a sarcomere. One end of the thin filaments is anchored to an interconnecting protein network known as Z-line. The I-band, crossed by the Z-line, includes the thin filaments located at the ends of the A-bands of the two neighbouring sarcomeres. There are also two additional bands: the H-zone is a tiny band located in the middle of the A-band while the M-line is a tiny and dark band located in the middle of the H-zone. Every thick filament is bounded with six thin filaments as a hexagonal array and also every thin filament is bounded with three thick filaments as a triangular shape.
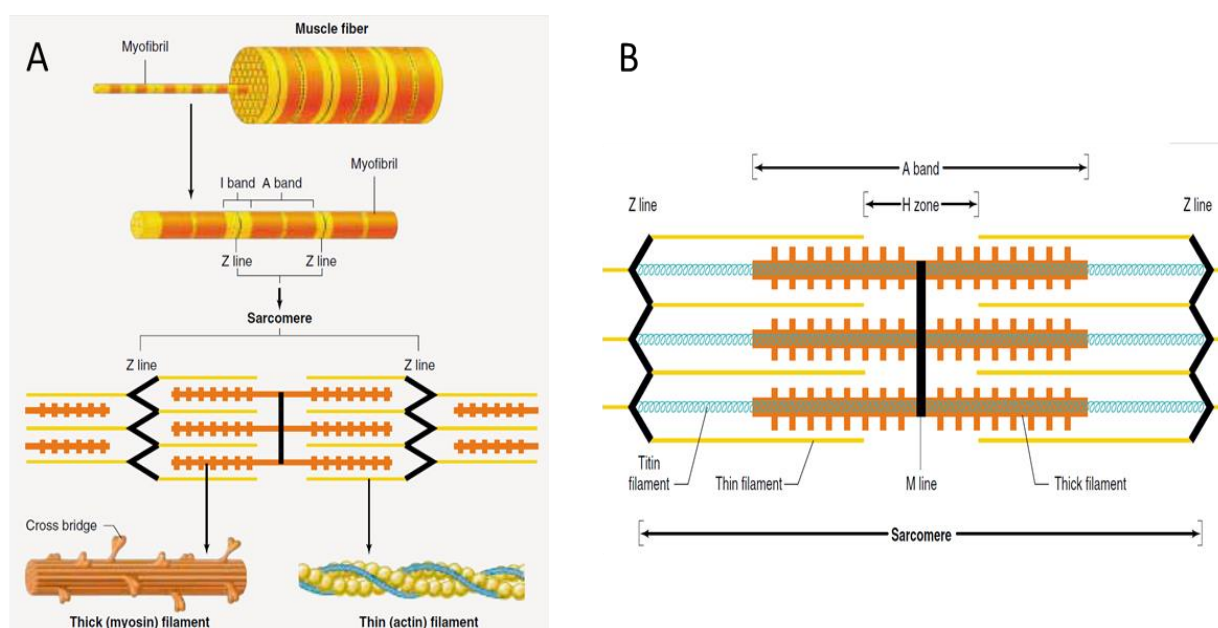


Figure 2.4: **A:** Structure of a muscle fiber **B:** Different bands of one sarcomere (from Vander et al. "Human Physiology: The Mechanism of Body Function" edition 8th, p. 295).

A contraction in a fiber occurs when in each of its sarcomeres, the thick and thin filaments move along each other (Figure 2.5A). This occurs when there is interaction between the many cross-bridges present over the surface of a thick myosin filament interact with a thin myosin filament (Figure 2.5B), each cross-bridge has a tail made of two heads which lengthen out to bind with actin. While an action potential (AP) travels along a muscle fiber, it also penetrates within the fiber through the release of $Ca^{++}$ ions which are stored in the sarcoplasmic reticulum Figure 2.5C & D). With the presence of $Ca^{++}$ ions, binding sites on the actin filaments are liberated permitting an interaction between actin and myosin (Figure 2.6). With the energy liberated by the ATP molecules, a sliding movement occurs between actin and myosin and each sarcomere length is reduced. The muscle shortening results from the many individual sarcomere contraction. After the passage of an AP, the $Ca^{++}$ ions are pumped back in the sarcoplasmic reticulum and the sarcomere length gets back to its relaxed length.
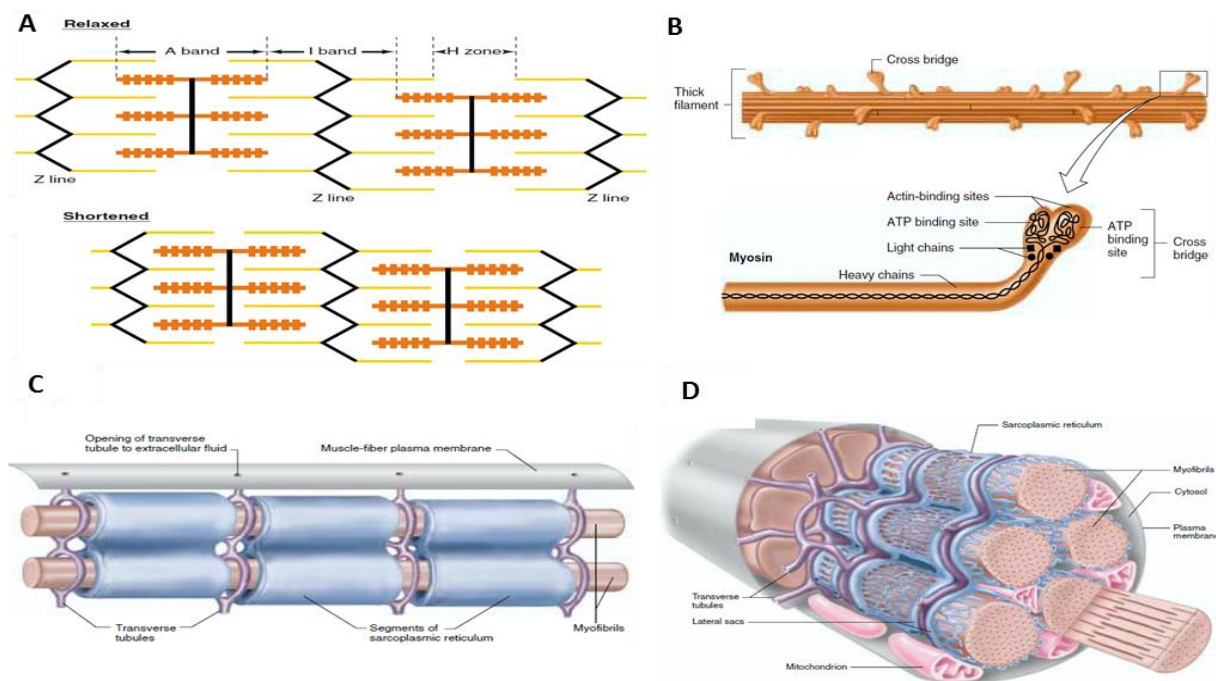


Figure 2.5: **A:** Sarcomeres in a relaxed condition (upper part) and in a contracted state (lower part). Contraction is associated to a shortening of the H-zone and the I-band occurs while the thick or the thin filaments keep their original length. **B:** The thick myosin contains many cross-bridges (upper part). The 2 heads of a myosin cross-bridge which can interact with actin (lower part) **C:** Illustration of the sarcoplasmic reticulum and transverse tubules with myofibrils. **D:** Perspective view of the transverse tubules and sarcoplasmic reticulum in a single skeletal-muscle fiber (from Vander et al. "Human Physiology: The Mechanism of Body Function" edition 8th, p. p. 298, 299,303).
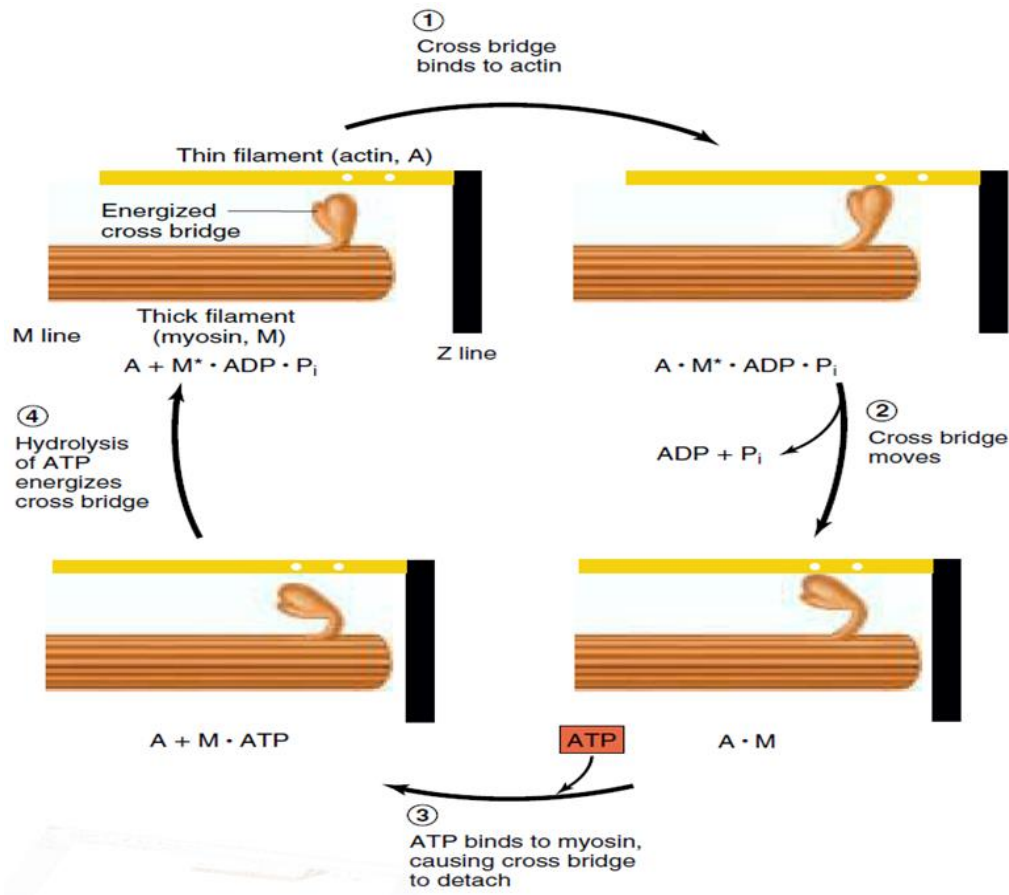
Figure 2.6: Contraction of a muscle fiber starts when a cross bridge connects to the actin in thin filament (step 1). As for step 2) the cross bridge moves and produces tension in the thin filament. Step 3) the cross bridge detaches from the thin filament. Step 4) the cross bridge obtains energy so that it can attach to the thin filament to start a new cycle (from Vander et al. "Human Physiology: The Mechanism of Body Function" edition 8th, p. 300).

## Types of contraction

There are two main types of contraction: isometric and isotonic. An isometric contraction occurs when the muscle's length is constant as when the tension generated is not enough to lift a given charge. Isotonic contraction happens when the charge is smaller than the generated force, the muscle's length shortens but the tension produced is constant. Besides those two main conditions, another one is called "eccentric" (lengthening) which occurs while the muscle length is increasing and the load against the muscle is greater than the generated muscle tension (occurs when going down a flight of stairs) [6] while its opposite is called "concentric" contraction which increases

tension on the muscle while it shortens. This contraction occurs most frequently in a gym when an athlete lifts a weight [7].

## Motor units

A motor unit (MU) is an entity constituted by a motoneuron (MN) and all the muscle fibers it innervates (Figure 2.7A). When an AP is triggered in a MN located in the spinal cord, it propagates along it axon toward the periphery where contact is made at the neuromuscular junction (NMJ) of each of its innervated muscle fibers (Figure 2.7B). NMJs are usually located in the middle of each fiber. Depending on its size, a muscle may contain few or many hundreds MUs. Generally, muscle fibers of a MU are dispersed within the muscle (Figure 2.7C).

## Types of Muscle Fibers

Muscle fibers are classified by their maximal velocities of shortening during a contraction and by their energy pathways which is: oxidative or glycolytic. Fibers shortening velocity is associated with myosin isozymes which determines their maximal rate of cross-bridge cycling: fast fibers are those having myosin with high ATPase activity while slow fibers are those with a myosin of low ATPase activity. While the rate of cross-bridges cycling in fast fibers is 4 times faster than in slower ones, the force produced by both types of fibers is roughly the same. As for the machinery used for synthesizing ATP, oxidative fibers are surrounded by numerous blood vessels which give them their dark-red color and their ATP production depends on blood flow. As for the glycolytic fibers which are surrounded by few blood vessels, they contain limited amount of myoglobin which gives them a white pale color. Based on these two criteria there are three types of skeletal muscle fibers (Figure 2.7D) and each of them offers marked difference in their ability to resist to muscular fatigue: while slow-oxidative fibers are fatigue resistant the fast-glycolytic fibers are very easily fatigable while fast-oxydative one stand in the middle of the 2 others. In general, the diameter of the glycolytic fibers are much larger than oxidative fibers. In all types of skeletal muscle fibers, the number of thick and thin filaments per unit in cross-section of a muscle is almost the same.
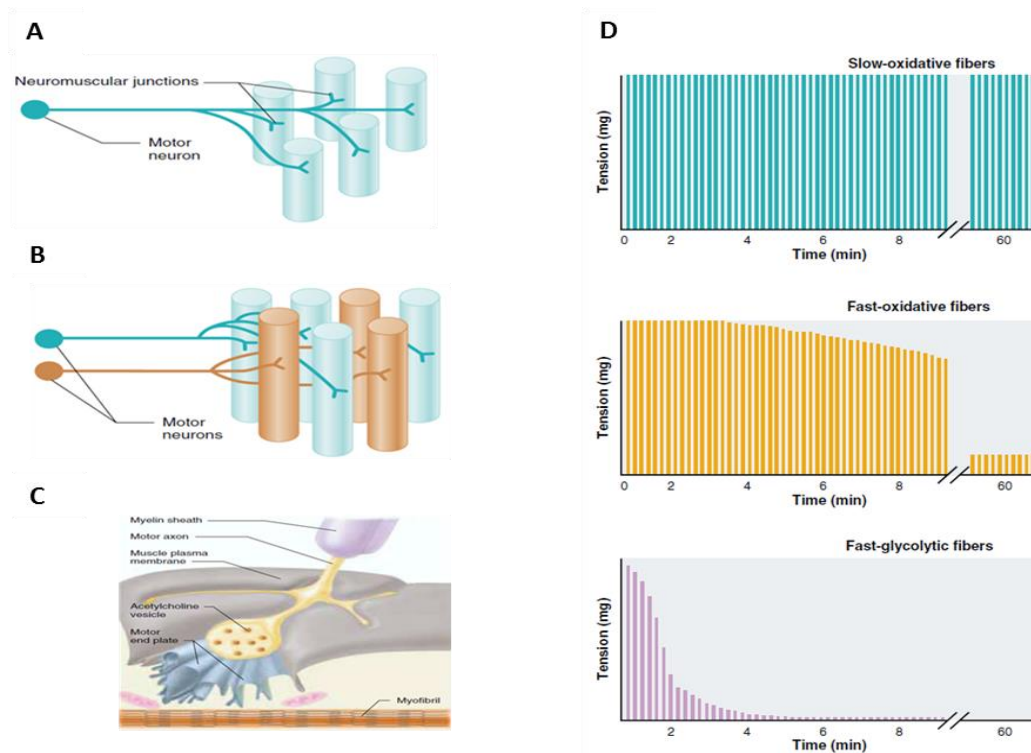
Figure 2.7: **A:** a motor unit is composed of a motor neuron and the muscle fibers it innervates through neuromuscular junctions. **B:** two motor units with their scattered muscle fibers. **C:** details of a neuromuscular junction where the motor axon terminal is inserted in grooves at the surface of a muscle fiber. **D:** various fatigue development rate for the 3 different types of muscle fibers. Each vertical lines is the response to a brief tetanic stimulus (from Vander et al. "Human Physiology: The Mechanism of Body Function" edition 8th, p. 305, 316).

## Electromyographic (EMG) signal

Various body organs generate electrical signals as for instances, the electroencephalogram (EEG) which is associated to the brain activity of the brain neurons, the electrocardiogram (ECG) which results from the cardiac cells activity and the electromyogram (EMG) which is generated when many muscle fibers are under contraction. All those signals are associated to the movement of ionic charges and to record them, electrodes are used to transform those ionic currents into electronic ones which can be amplified, filtered, digitized and stored before processing. To record EMG activity, intramuscular electrodes are used when information on a local region of a muscle is searched while surface electrode, i.e. electrodes placed over the skin, are more appropriate when a more global information on a given muscle is needed.

In 1829, Adrian and Bronk were the first to use an intramuscular needle [8]. Such an electrode is made of a hypodermic needle where recording occurs between the cannula and a conducting core (Figure 2.8A). The outer diameter of the cannula ranges between 0.3 to 0.7 mm while the diameter of the core section is generally 0.1 mm. The cannula is made of stainless steel and the core of silver or platinum [8]. As for surface electrodes which are applied directly on the skin over the muscle to be studied, they are usually made of Ag/AgCl pellets (Figure 2.8B) or from metal such as gold (Figure 2.8C). Surface electrodes are much more frequently used than intramuscular ones since they are not invasive, totally painless and there is no risk of infection. In addition, they can be simply used without special expertise and long term recording is possible.
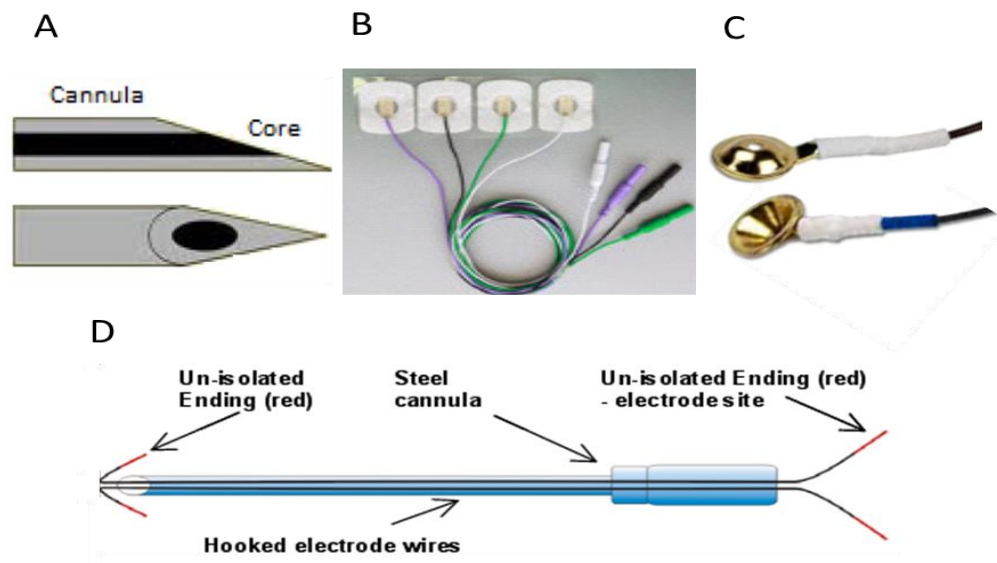


Figure 2.8: **A**: intramuscular needle electrode [9]. **B:** surface Ag/AgCl pallets (from: http://cdn.shopify.com/s/files/1/0150/1454/products/2021_medium.jpg?v=1335040383). **C:** gold cup surface electrode (from: http: //www.mvapmed.com/Catalog/2014-EEG-Web.pdf). **D:** Fine wire (from: http:// www. Noraxon .com /wp -content/uploads/2015/01/kinesilogical-fine-wire-emg-booklet.pdf).

## Compartments in muscles

Within some animals or human muscles, subdivisions known as neuromuscular compartments can be found. In 1953, Cohen [10] stretched a tiny strip of a cat rectus femoris muscle and observed a contraction in that strip but not in the rest of the muscle. When Weeks and English [11] examined the cat lateral gastrocnemius (LG) muscle to determine behaviour of its anatomical organization, an extensive overlap at the spatial distribution of motoneurons (MNs), that innervate its various primary muscle nerve branches), was found. MNs supplying each PMNB were also of considerably

different sizes. Those supplying proximal compartments were located in the more rostral portions of the LG and they were among the largest in the pool; small MNs innervated the proximal compartments and their number was small. Neurons that mainly supplied the distal compartments were found in the more caudal parts of the pool and their size was either large or small.

Chanaud et al. [12] studied cat hindlimb to determine the roles of the semitendinosus (ST), the tibialis anterior (TA), the biceps femoris (BF) and the tensor fasciae latae (TFL). Using chronic recording techniques, they collected EMG activity from various sites of every muscle during treadmill locomotion, ear scratch and paw shake. In the BF and TFL, separate neuromuscular compartments were shown to contribute to mechanical movements at the hip and knee joints. For the ST and TA during slow-moderate gait speeds, a region with muscle fibers of type I was active. Increasing speed resulted in additional fibers recruitment. Regions of the muscle with many muscle fibers of type II and III units got active at moderate and high gait speeds. Widmer et al. [13] examined the rabbit's masseter to determine if its compartments were activated differently during different jaw displacements. Fine wire electrodes were inserted in each of the 9 compartments in the right masseter, in some compartments of the left masseter, at two sites of the right digastric and in one on the left one finally one in each right and left pterygoid muscles. Using principal component analysis (PCA), signals from the 16 recording sites were separated in groups containing 3 to 6 EMG signals. A pair-wise comparison was done to compare activities between the 9 masseter compartments. They demonstrated that during jaw movements similar to those made during rhythmic chewing, the rabbit masseter muscle's compartments were functional. Such activity in the masseter muscle appears to be related to the unique mechanical actions of the compartments which is required during mastication. As for Lucas-Osma and Collazos-Castro [14] who investigated the triceps brachii of the rat, they found for each of its 3 heads, a region within the spinal cord where their innervating MNs were clustered. The long head had the largest motoneuron pool followed by the medial and lateral heads. While MNs of the medial and lateral heads were mainly located in the rostral part of the spinal motor column, those of the long head occupied mainly its caudal part.

In human lower limb, Wakeling [15] investigated the soleus, the lateral (LG) and medial gastrocnemius (MG) activity during cycling on a stationary bicycle. The LG and MG muscle belly

was divided in 4 quadrants in which a pair of surface electrodes were put. From low cross-correlation values between every raw EMG signal recorded from a pair of electrodes, it was concluded that the different regions of the gastrocnemius was populated by different MUs. Studying the tensor facia latae of ten normal subjects with inserted fine-wire electrodes, Paré et al. [16] demonstrated a functional different role for its anteromedial and posterolateral fibers. Those findings coupled with anatomical dissections they made on 6 cadavers indicated that TFL activity can be explained by their mechanical advantages on the hip: anteromedial fibers had a superior mechanical advantage for hip flexion comparing to the posterolateral fibers while posterolateral ones have a better mechanical benefit for hip abduction and internal rotation. So, near heel-strike during walking, anteromedial fibers were silent while posterolateral ones were active.

At the trunk level, Paton et al. [17] placed six miniature surface electrodes along each segment (compartment) of pectoralis major (PM) and reported that in an isotonic test, they were independently controlled. The most inferior segments of that muscle were activated when the subjects performed shoulder extension action starting from a flexed position. Inversely, the superior segments of PM were activated in shoulder flexion motion. For horizontal flexion of the shoulder joint, the middle segments of the muscle were activated and this was regardless of the degree of the shoulder flexion.  In the back, Holtermann et al. [18] found that each of the  4 anatomical subdivisions (compartments) of the trapezus could be individually activated by voluntary command. At the shoulder level, Wickham and Brown ([19], [20], [21]) investigated the human deltoid and from its 7 compartments, it was found that activity of at least 6 of them could be controlled. The compartment's activation timing and intensity were dependent upon the muscle compartment's line of action in a given movement. In a given movement, more active muscle compartments can be functionally considered as principal mover.

When Segal et al. [22] studied the hand flexor carpi radialis (FCR), the extensor carpi radialis longus (ECRL) and the lower limb lateral gastrocnemius (LG), they found that the 3 subdivisions (compartments) of the FCR were individually innervated while 2 nerves innervated at least two different ECRL sections that where not identical to its architecture. In the LG, a single nerve divided into two branches which further subdivide to innervate its 3 heads; thus each head may not be innervated by a private nerve branch.

In the upper limb, Lee et al. [23], investigated 56 fresh cadaveric arms to determine the spatial location of intramuscular motor nerve endings on the biceps brachii (BB) and brachialis muscles. For the BB (Figure 2.9), they found 3 musculocutaneous nerve branching patterns: type I with one main motor branch which divided into two sub-nerve branches to innervate the LH and SH of the BB; type II with two main motor branches where the proximal branch innervates the SH, and distal one innervates the LH; type III, with one main motor branch that divides into two sub-nerve branches which separately innervate LH and SH (type III is a variation of type I).



Type I            Type II            Type III
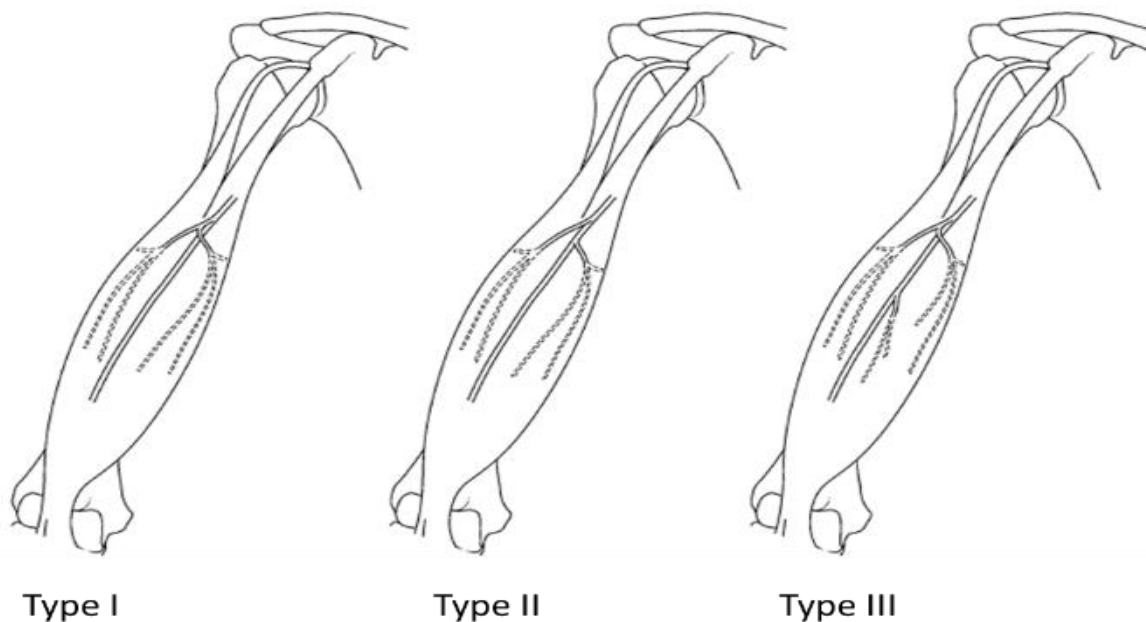
Figure 2.9: Three types of nerve branch patterns for BB muscle. In Type I, from a main motor nerve, a branch is separated then it is subdivided into two different parts to innervate SH and LH. In Type II, from a main motor nerve two individual nerve branches innervate SH and LS separately. Type III, which is a variation of type I, from a main motor nerve a branch separates and this branch innervates SH and LH individually (from Figure3 of Lee et al., 2010).

From the BB dissection of cadavers Segal [24] found, on the posterior view of the muscle, signs indicating the presence of up to 6 compartments individually innervated by a nerve branch (Figure 2.10). Being interested in the control of upper-limb myoelectric prostheses, capable of many movements such as some mentioned in the following section which needed many control signals to use them, our attention was focused to this muscle.
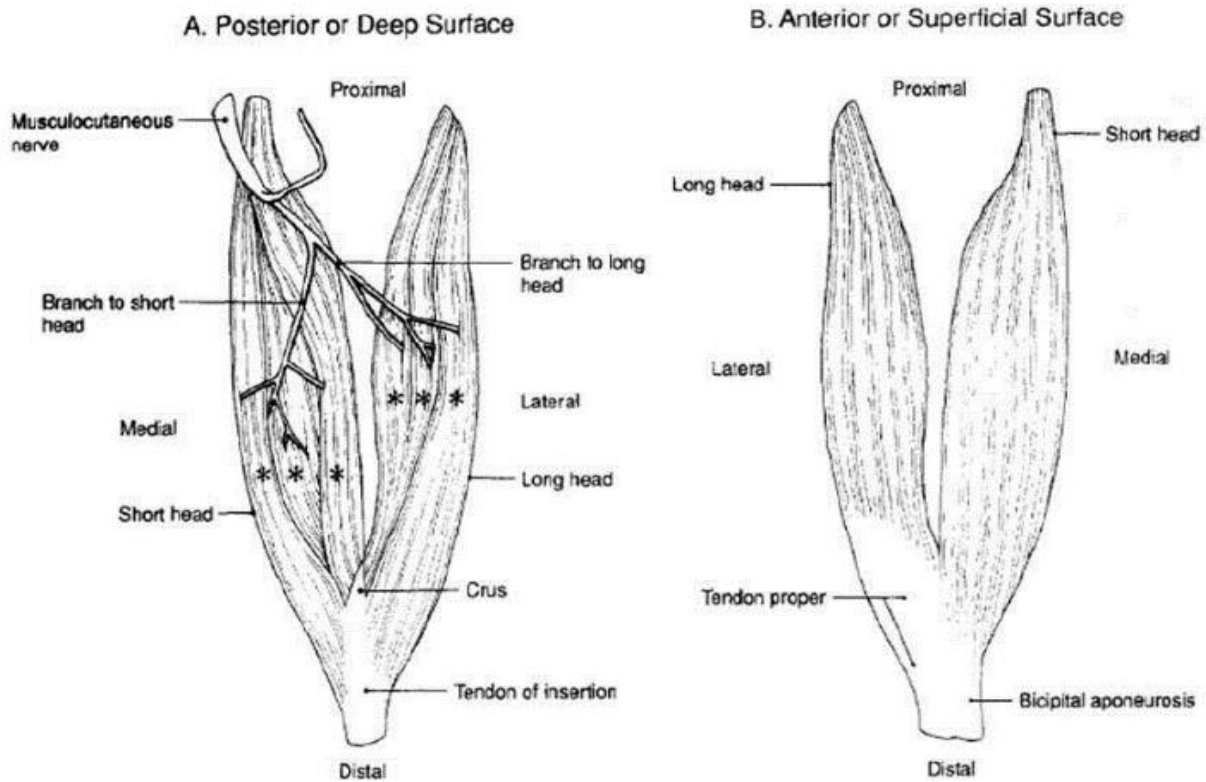
Figure 2.10: **A:** sketch of the posterior view of biceps brachii illustrating the 6 compartments innervated with an individual nerve branch. **B:** anterior view of the muscle devoid of any sign the compartments (from Segal, 1992).

## Conductivity[1]

Many sources are presenting conductivity values of the human body's tissues. On the web, reference [25] is paricularly interesting because a lot of biological tissues are considered with a frequency range varying from Hz to GHz. The conductivities we used in our simulations (Table 2.1), were gathered from Andreuccetti et al. [26] because this database was established with a collection of many references including the often cited Gabriel et al. [27].

---

[1] How RMS values were obtained from EMG records is presented in Appendix **C**

Table 2.1: Conductivity of different tissues of human body in 100 Hz. *includes cephalic, brachial and basilica veins and the brachial artery  (from [26]).

| Tissue | Conductivity (S/M) |
|---|---|
| Bone | 0.02 |
| Muscle | 0.26671 |
| Fat | 0.02081 |
| Nerve | 0.028042 |
| Blood Vessels* | 0.27789 |
| Skin | 0.0002 |

## Modern myoelectric prostheses

Following an amputation, the main purpose of an upper arm prosthesis is to restore the many movements needed daily and to have the appearance of the missing part. Besides prostheses used only for cosmetic concern, others are capable of producing a various number of movements. The simplest are body-powered: with a harness and cables, shoulder movements are used to move the forearm and open the hook to grasp and hold an object. Durable, their lack of natural appearance is compensated by their easy operation and low cost. For more versatile prostheses a rechargeable battery is used as the source of power to feed onboard electronics and to activate motors to produce movements as illustrated in Figure 2.11A. The socket is adapted to the anatomy of the amputated person. It includes windows where electrodes make contact with the skin over the muscles used to control the prosthesis: a contracted muscle generates and electric signal (EMG) which is processed by the electronic circuits and used to produce a movement.  Depending on the contracted muscle, an electrical motor at the elbow level flex or extend the arm while a second motor can be used to rotate clockwise or contraclockwise the artificial hand and a third one is used to close or open it.

On some prostheses, faster movements and more precise movements can be produced when intensity of the muscles contraction can be achieved by the amputee person. With accurate sensors and modern step-motors, even small objects like coins and keys can be grasped with modern

artificial hand as shown in Figure 2.11B. Since motors, battery and electronics are inside the prosthesis, they are heavier than cosmetic or body-powered prostheses and are more expensive.

As modern prostheses offer many degrees of freedom (DOF), more control signals are required to take full benefit of their capabilities. [28, 29]. It is why we are aiming at increasing the number of control sites that could be collected over the biceps by activating each of its compartments.
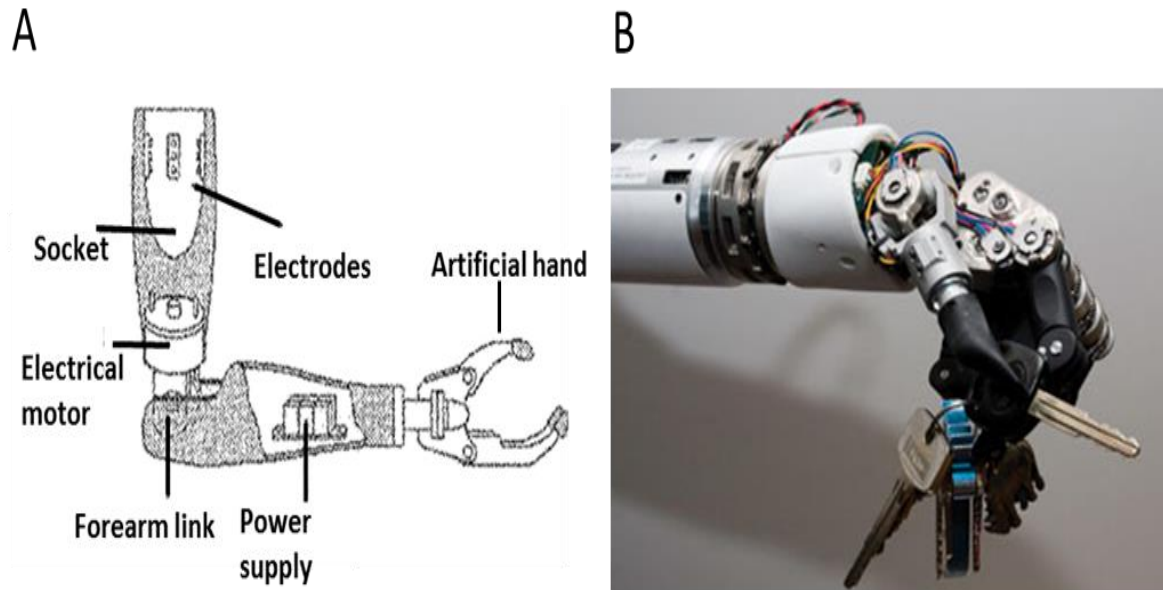


Figure 2.11: **A:** Illustration of a myoelectric prosthesis where forearm can be flexed and the hand rotated and close to grasp an object when the thumb and the 2 fingers are moved toward each other (from: http://www.rehab.research.va.gov/jour/98/35/3/bonivento.htm#top). **B:** Myoelectric prosthesis with several degrees of freedom (from: http:// spectrum.ieee.org /biomedical/ bionics/ dean-kamens-luke-arm-prosthesis-readies-for-clinical-trials).

It should be mentioned that commercially available modern upper limb myoelectric prostheses can have many degrees of freedom and produce many useful hand movements with high accuracy as can be seen in the following web pages:

- www.ottobock.ca
- www.touchbionics.com
- www.rslsteeper.com
- www.liberatingtech.com
- www.dekaresearch.com/deka_arm.shtml

## Direct and indirect model

In many situations, there is interest to explain an outside observable phenomena in terms of its internal origins. For instance, studying heart electrical behavior, Okada (1956) [30] proposed a theoretical  model capable of  reproducing the potential fields over the human trunk. To test his model, he conducted experiments where an eccentric z-oriented current dipole, simulating the heart was located in a finite length cylinder filled with a conducting medium (Figure 2.12). As can be seen in the B panel of that figure, the direct model provided a good fit with experiments data but the model did not converge on the border, at the top and at the bottom of the cylinder.
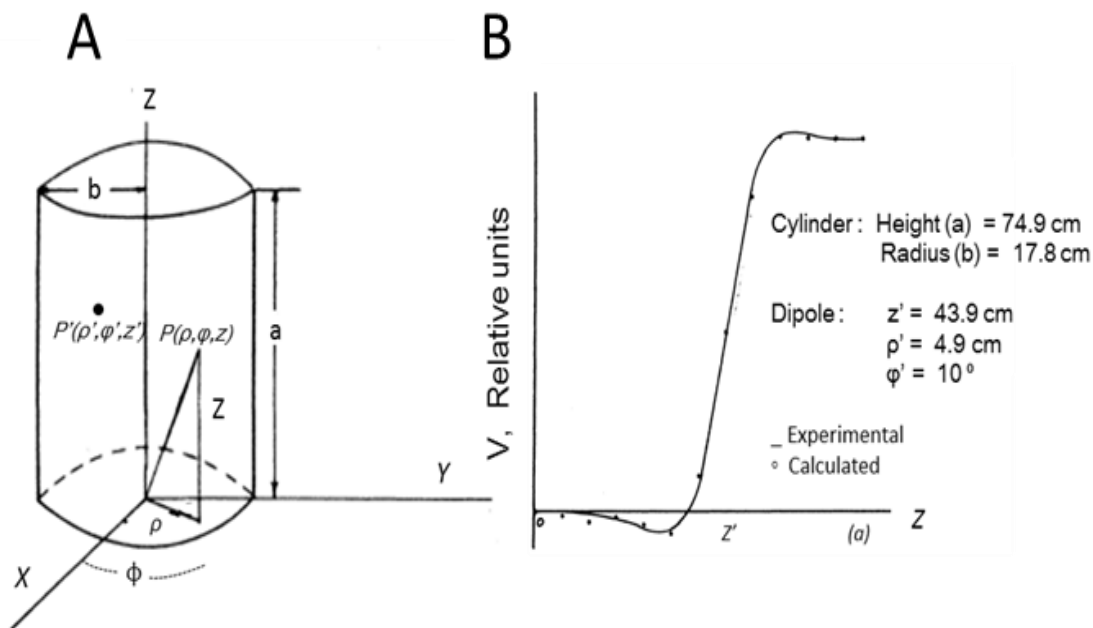


Figure 2.12: **A:** Cylindrical model of human trunk. The position of the eccentric current dipole was shown as $\rho'$ and other arbitrary locations can be shown as $\rho$. **B.** Comparison of experimental and calculated results. The eccentric z-oriented current dipole is placed along Z-axis at 58.5% of the total height of the cylinder (from: Okada Figs 1 and 2).

This lack of convergence in some conditions for the Okada's model as well for the model of  Frank [31] and the one of Burger et. al [32] was corrected by Lambin and Troquet in 1983 [33]. To get potentials everywhere with a finite cylinder model where the dipole could be oriented everywhere

in space, they used the Green's function to solve the Poisson's equation. Their results for different dipole orientations are shown Figure 2.13.
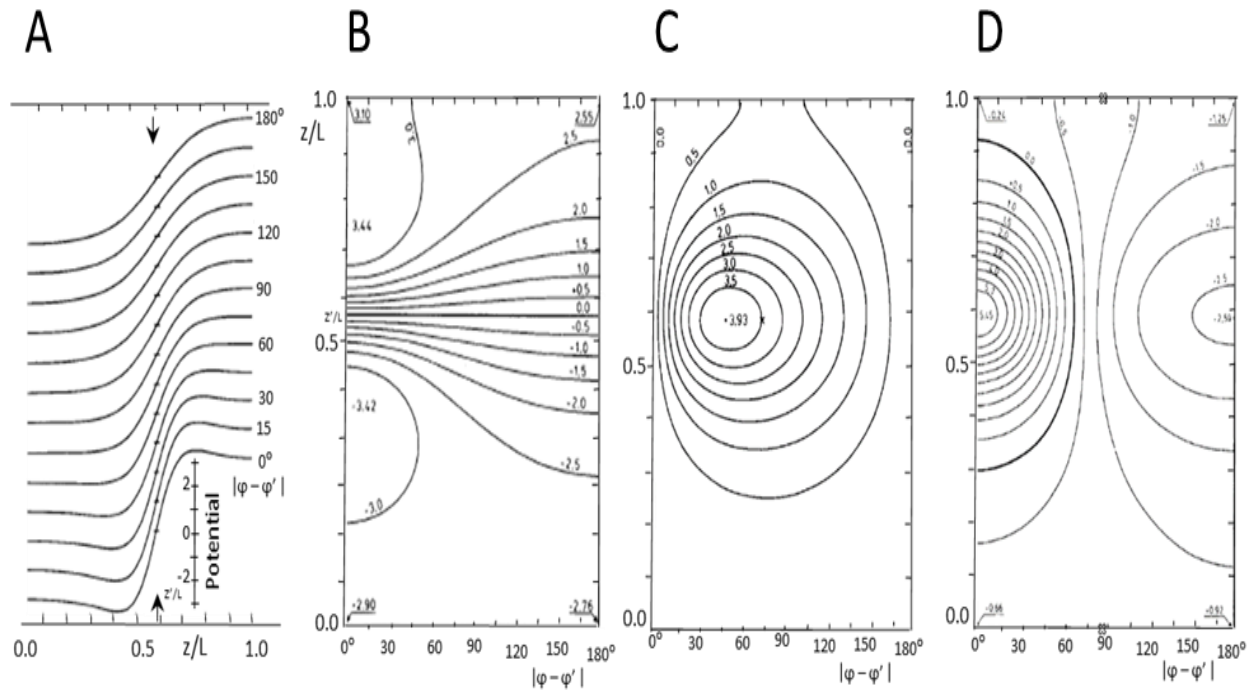


Figure 2.13: Potentials produced by an eccentric current dipole in a finite length cylinder. The height of cylinder is L= 74.9 cm and its radius is R= 17.8 cm and the dipole is located at $\frac{\rho'}{R}$ =0.227 and $\frac{z'}{L}$ = 0.586. The potential unit is arbitrary. **A:** Curves of potential for 0˚ to 180˚ (half of the surface layer of the cylinder) produced by an eccentric z-orientation current dipole. The small horizontal bars address the zero potential level in each angular curve. **B:** Curves of equipotential planes for z-oriented dipole **C:** Curves of equipotential planes for $\varphi$-oriented dipole **D:** Curves of equipotential planes for ρ-oriented dipole (from Lambin and Troquet Figs 2, 3, 5, and 6).

The direct model approach was also used by Saitou et al. in 1999 [34] to calculate over the BB the EMG potentials generated by current sources inside the arm considered as a semi-finite volume conductor. In their experimental results with 3 healthy subjects, 16 pairs of small electrodes were placed over the BB either distally or proximally of the innervation zone (left of Figure 2.14) and low-level isometric contractions were produced in order to be able to record activity of individual MUs. Using the image method and minimizing the differences between experimental results and model data, they estimated the depth and intensity of current sources at the origin of the surface potentials.
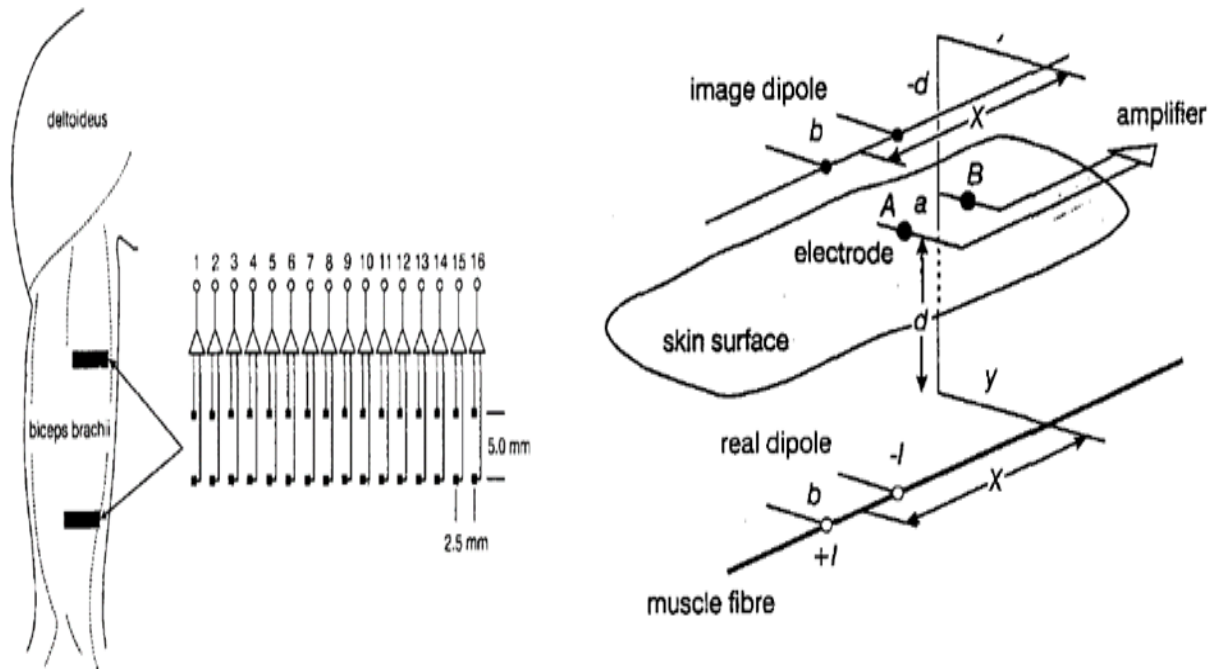
Figure 2.14: **Left:** 16 pairs of surface electrodes were placed over the BB. Along the fibers direction, electrodes were 5.0 mm apart while across the fibers, the inter-electrode distance was 2.5 mm (Figure3 of Saitou [34]). **Right:** Illustration of the image method used (from: Figure2 of Saitou [34]).

In their image method (right of Figure 2.14), a dipole represents a current source in the muscular tissue and the dipole is located in the center of the bipolar recording electrodes. In that figure, the Y-axis is perpendicular to the muscle fibers and X-axis is along the muscle fibers direction. Assuming that $b \approx 0$, the surface potential is given by their equation 4 which is:

$$\Phi = \frac{Ib}{2\pi\sigma}\left[\left\{(X+\tfrac{a}{2})^2 + y^2 + d^2\right\}^{-3/2}\left(X+\tfrac{a}{2}\right) - \left\{(X-\tfrac{a}{2})^2 + y^2 + d^2\right\}^{-3/2}\left(X-\tfrac{a}{2}\right)\right] \qquad (1)$$

where: I (A) = the intensity of the current dipole

X (m) $= x_0 - vt$

$x_0$ (m) = the location of the neuromuscular junction in the muscle fiber direction

v(m/s) = velocity of the muscle fiber conduction

t(s) = time

$\sigma$ (S/m) = the conductivity of the medium

a = the distance between the contacts of the bipolar electrode

b = the distance between the current sources of a dipole

X = the coordinate of the direction along the muscle fibers

Y = the coordinate of the direction across the muscle fibers

The muscular tissue was considered anisotropic: i.e. $\sigma_x = 0.5$ along the fiber and $\sigma_r = 0.1$ perpendicularly to the fiber direction. From Plonsey (1974), the X-axis along the muscle fibers then becomes:

$$X' = \sqrt{5}X \tag{2}$$

The velocity of the muscle fiber conduction was considered to be 4 m/s. The goodness of fit function G to be maximized was:

$$G = 1 - \frac{E}{S} \tag{3}$$

where E is the sum of the squared differences between experimental results of surface EMG ($M_{ij}$) and calculated results ($C_{ij}$) and S is the total power of the experimental records:

$$E = \sum_{1=1}^{16} \sum_{j=1}^{n} \left\{ M_{ij} - C_{ij} \right\}^2 \tag{4}$$

$$S = \sum_{1=1}^{16} \sum_{j=1}^{n} M_{ij}^2 \tag{5}$$

The numbers of dipoles were increased until G became less than 2% then the number of dipoles at that level was assumed to be optimum. To get more accurate estimation and also to avoid minima, the procedure was repeated 10 times while the initial values of parameters varied randomly. From the 3 subjects, 36 different MUs with different waveforms and distributions were analyzed. Three different types of results are depicted in Figure 2.15 where in each of them, the left-side panels show measured MUAPs while those on the right panels represent calculated MUAPs obtained with the image method. For them, each estimated current source was located at 2.7 ± 1.6 mm deep with 0.5± 0.9 nAm in intensity whereas, the total current intensity for a single MU was 2.4 ± 2.9 nAm.

**a.**

measured MUAP    Calculated MUAP (Goodness of fit 88.8%)

MUAPs in right-side were duplicated with five current dipoles with characterizations as: 1) Depth (D): 3.8 mm, current intensity (CI): 0.9 nAm 2) D: 4 mm, CI 3.3 nAm 3) D: 2.4 mm, CI:2.5 nAm 4) D: 1.7 mm, CI: 0.7 nAm 5) D: 3 mm, CI: 0.4 nAm

**b.**

measured MUAP    Calculated MUAP (Goodness of fit 82.6%)

1) D: 0.5 mm, CI: 0.1 nAm 2) D: 0.3 mm, CI: 0.1 nAm 3) D: 1.1 mm, CI: 0.2 nAm 4) D: 1.1 mm, CI: 0.2 nAm 5) D: 1.2 mm, CI: 0.1 Nam

**c.**

measured MUAP    Calculated MUAP (Goodness of fit 93.2%)

1) D: 2.2 mm, 0.1 nAm 2) D: 5.7 mm, CI: 0.8 nAm 3) D: 6.2 mm, 0.6 nAm 4) D: 3.7 mm, 0.6 nAm 5) D: 6.6 mm, 2.6 nAm 6) D: 3.7, CI: 0.8 nAm

Figure 2.15: **a.** MUAP with a single peak and symmetric distribution. **b.** MUAP with two distinguishable peaks. **c:** complex MUAP. The dipoles characteristics are shown under each different MUAP (from: Saitou [34] Figs 5, 6, 7).

As for Roeleveld et al. [35], they used five different types of volume conductors to investigate the motor unit potentials (MUPs) of the BB. The volume conductor represented by finite/infinite size of cylinders and the number of layers varied as 1, 2 or 3 layers demonstrating muscle, subcutaneous fat and skin. The simulation results of three-layer model was closest to the measured MUPs. The three-layer model is shown in Figure 2.16. The anisotropy condition was taken into account using independent conductivities in radial and axial directions where the radial ($\rho_z$) and axial ($\rho_r$) conductivity values for muscle tissue were given as 0.1 and 0.5 S/m.
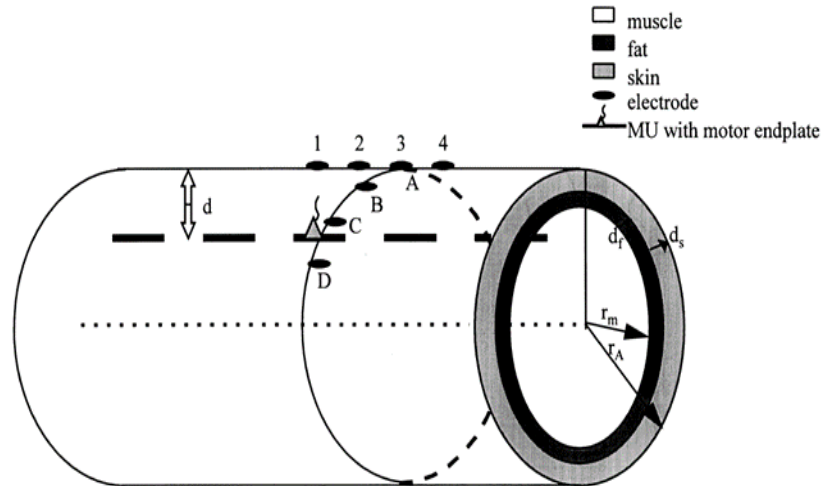
Figure 2.16: Three-layer model. The radius of muscle, air layer, and thickness of fat and skin were shown by $r_m$, $r_A$, $d_f$ and $d_s$ respectively. The MU was positioned as (d) distance inside the model and far from the skin layer. One row of electrodes (A to D) were positioned perpendicular and the other row (1 to 4) was located parallel to the muscle fiber. Inter-electrode distances was set to 12 mm. (from: Roeleveld *et al.* [35] Figure1).

The fat and skin tissues are considered as isotropic with ρ= 0.05 and 1 S/m respectively. The air medium with zero conductivity and 3 mm thickness surrounded the volume conductor to isolate the model. Based on experimental data the characterization of different models can be found in Table 2.2. The input was given as an arbitrary line source parallel to the skin surface. Two sources were positioned at the ends of the line source to show effects of start and end of the muscle fiber. Two perpendicular rows of electrodes with inter-electrode distances of 12 mm were positioned on the skin surface. One row of the electrodes was located along the muscle fiber and parallel to the skin layer and the second one was situated over the circumference of the model. Potentials were considered relative to a reference electrode (zero potential) located far away from active area. In order to get signals sufficiently higher than noise level during low force contractions, three MUs with different depths (the deepest 15 mm, 7.5 mm and the most superficial 5 mm below the skin layer) were considered. The calculated potentials from these three different depths motor units (Mus) were compared to the experimental recorded potentials which were approximately generated from MUs with the same depth from the skin layer. The results of three MUs along the fiber and perpendicular to the fiber (along the circumference) are shown in Figure 2.17 and Figure 2.18 respectively.

Table 2.2: Five model configurations (from: Roeleveld *et al.* [35] Table 1)

| | Volume | Number of layers | Layers (mm) |
|---|---|---|---|
| III | finite | 3 | $r_m = 32, d_f = 1, d_s = 2$ |
| IIa | finite | 2 | $r_m = 32, d_f = 0, d_s = 3$ |
| IIb | finite | 2 | $r_m = 32, d_f = 3, d_s = 0$ |
| Ia | finite | 1 | $r_m = 35$ |
| Ib | infinite | 1 | $r_m = \infty$ |

Simulated recordings are always made at $r_A = 35$ mm
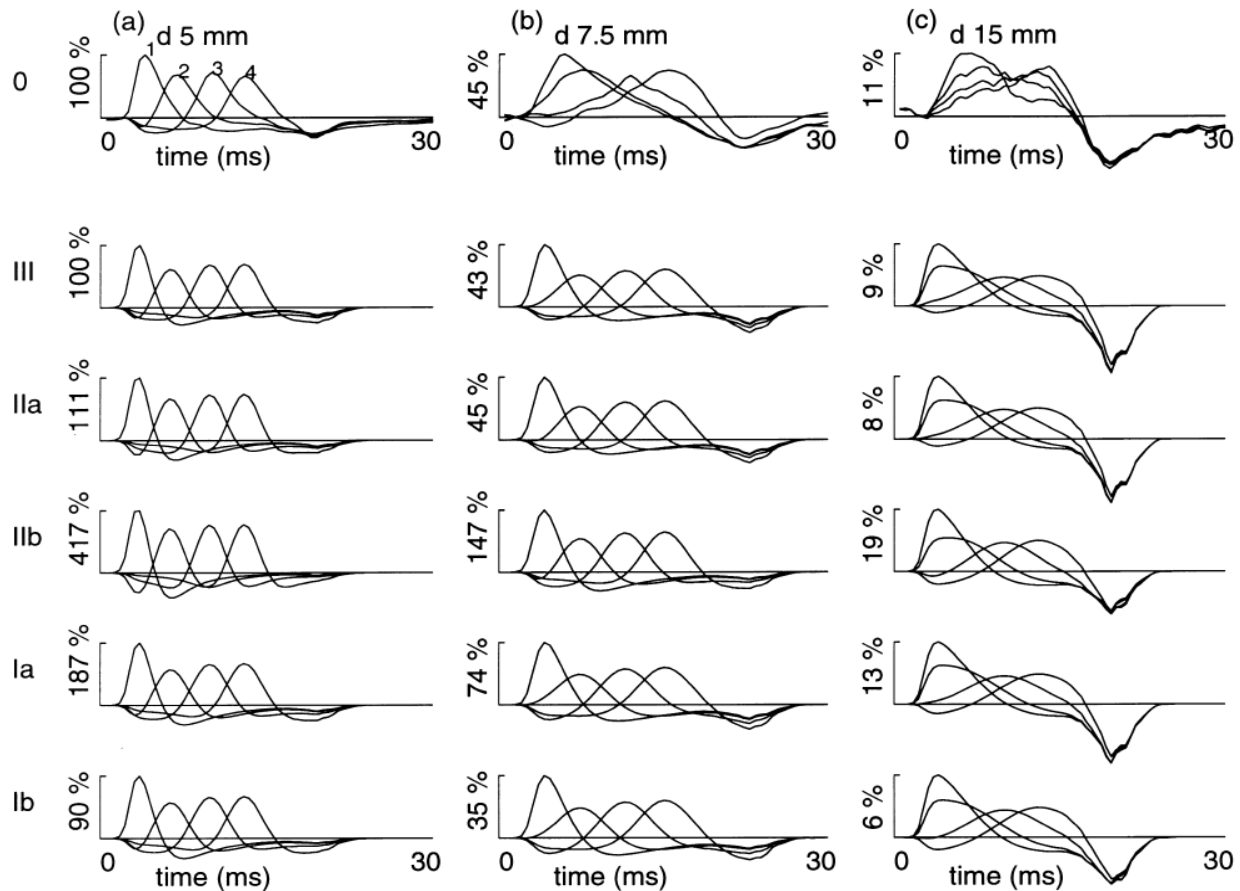


Figure 2.17: MUPs along the muscle fibers (1 to 4 refer to electrodes placed along model length in Fig2.16). For the experimental results shown in row 0, 100% of the vertical axis represents the highest value in that condition. Vertical axes in (b) and (c) are relative to the 100% of (a). Simulation results shown in the other rows are from the various models shown in Table 2.2 for a fiber at a specific depth. Amplitude of the maximum simulated result for model III at 5 mm represents 100% on the vertical axis. The % for the other simulated result are relative to that 100% (from: Roeleveld *et al.* [35] Figure4).
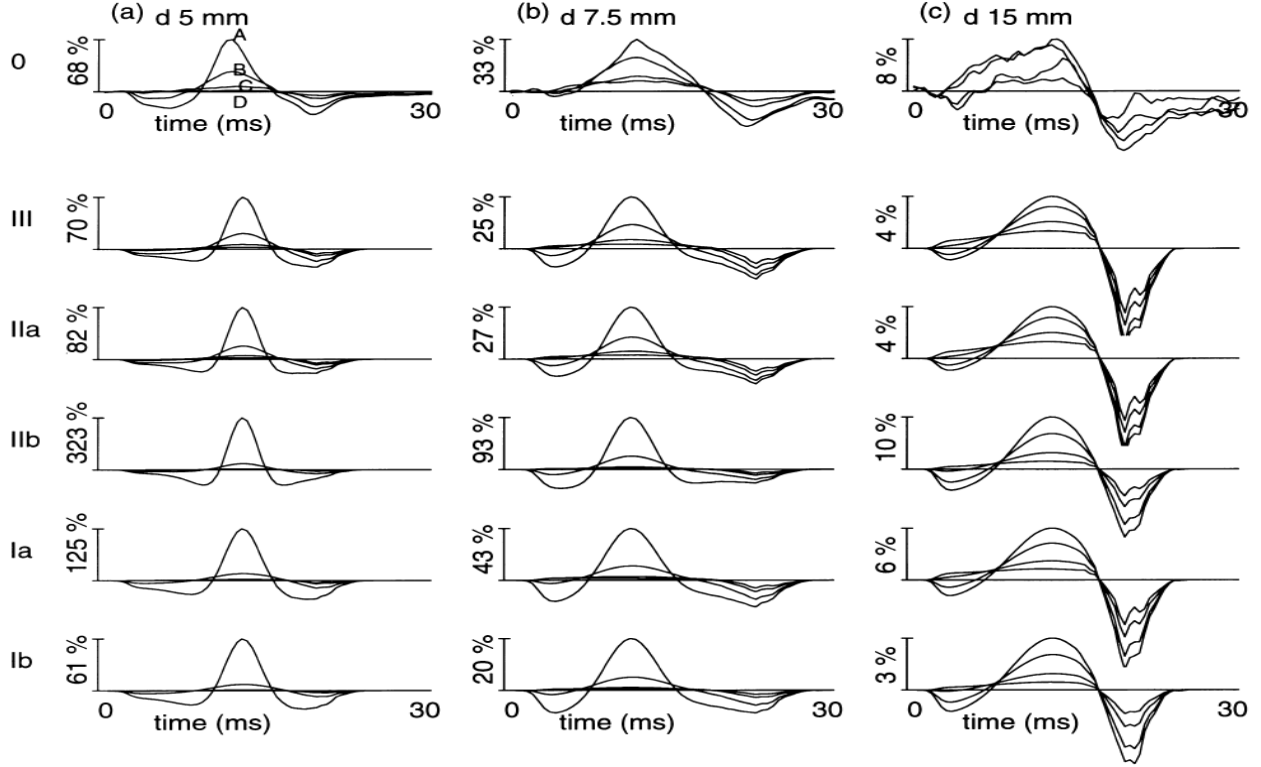
Figure 2.18: Experimental results (row 0) and simulated ones on the other rows when the electrodes are placed perpendicularly to the muscle fiber (A, B, C, D in Fig. 2.16). The indicated % are relative to the 100% of Fig. 2.17 (from: Roeleveld et al. [35] Figure 5).

As for Chauvet et al. [36], they used an analytical function to localize bioelectric sources from EMG surface recordings. They simulate the generation of 16 surface signals collected at 11 mm intervals over the half cross-section of the upper arm (Figure 2.19). A weak isometric contraction is considered and a single fiber action potential (SFAP) is represented by:

$$v(t,r) = V_2(r) - b_i(r)t^2 e^{-t^2/\sigma_i(r)}$$

where t = time, r = electrode to fiber distance, $V_2(r)$= 2nd phase magnitude, $b_i(r)$ and $\sigma_i(r)$ = shape coefficients. MUs firing rate depended on the MUAPs duration and ranged between 7 and 33 Hz. To generate a MUAP train (MUAPT), a firing rate was convolved with a MUAP and the resulting EMG signal collected by each electrode represents the summation of the MUAPTs. Signals of 1 s long were generated.
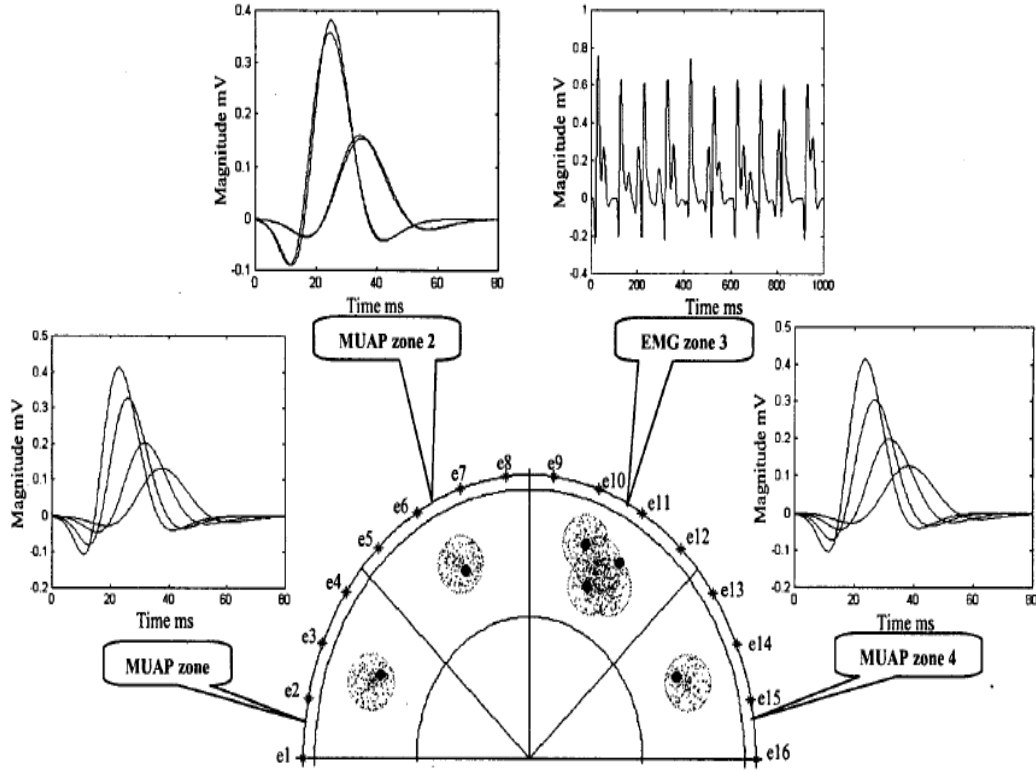
Figure 2.19: Localisation of emission sources in a muscular cross section. Detection system included 16 surface electrodes over the half part of the upper arm cross section. The (●) symbol is the average geometry of the source found by the proposed program from motor unit action potentials in zone 1, 2 and 4 but in zone 4 it is scattering of micro active area detected on inadequate superimposed SEMGs (from: Chauvet et al. [36] Figure1)

To estimate the electrode-source distance and the sources locations within the model (inverse model), the following equation was used:

$$V(d,t) = k(t)/d^{a(t)}$$

where $V(d,t)$= amplitude of MUM, $k(t)$ and $a(t)$ = middle parameters, $d$ = Euclidean distance between the electrode position $(x_e, y_e)$ and the active source $(x_s, y_s)$ in the recording system plane.

For the optimization method, the gradient method was used where a cost function was minimized:

$$c = \sum_{i=1}^{N}(Y_{i,calculated} - Y_{i,observed})^2 = \sum_{i=1}^{N}(a.X_i + b - b_{i,observed})^2$$

where $Y_{i,calculated} = \log(V_{i,calculated})$, $Y_{i,observed} = \log(V_{i,observed})$

and $V_{i,calculated}, V_{i,observed}$ are squares of the calculated and observed amplitude at the ith electrode's position and at time instant t.

The muscular cross-section is divided in 4 zones (Figure 2.19) and only one active region per zone and per instant is allowed. Two maximum amplitudes for two given distances are initially chosen and the algorithm seeks the electrode with the highest potential value to determine the initial position of the source. With a threshold value for very low amplitude potentials and a stop criteria (< 10% between forward and inverse results), the algorithm iterates along the duration of the signal before displaying the results as in Figure 2.19.

In summary, a model with few simple hypotheses was assumed and simulated signals facilitate the testing of the inverse solution. For zones 1, 2, and 4, the average coordinates of the sources detected were always close to the center where the MUAPs had been placed. As for zone 3, were various MUAPs were superimposed, 3 active regions could be observed but with the algorithm used, their precise location is uncertain. While the arm model appears in Figure 2.19 to be made of 3 concentric layers, there is nothing in the text about them and this model could then be considered as made of a one layer cylinder.

For a more realistic volume conductor, Jessinger et al. [37] used cross-section magnetic resonance images (MRI) of the arm from elbow to shoulder. A finite element model (FEM) was used where bone, muscle and fat tissues with their conductivity was built and Poisson's equation used for the purpose of identifying a finite number of sources. Experimentally, an array of 4 mm disc electrodes was placed over the bicep and the triceps of the subjects' left arm. A sample of an EMG signal and its power spectrum are shown in Figure 2.20 A and B. Using a time-frequency distribution for each recorded signal, the frequency of interest was found to be 46 Hz. Assuming a single 46 Hz sinusoidal source, the location of the source was determined with an optimization method. At Figure 2.20 C, the source (small black point) is located within the meshed model. The experimental results and those obtained with the dipole results were compared at Figure 2.20 D.
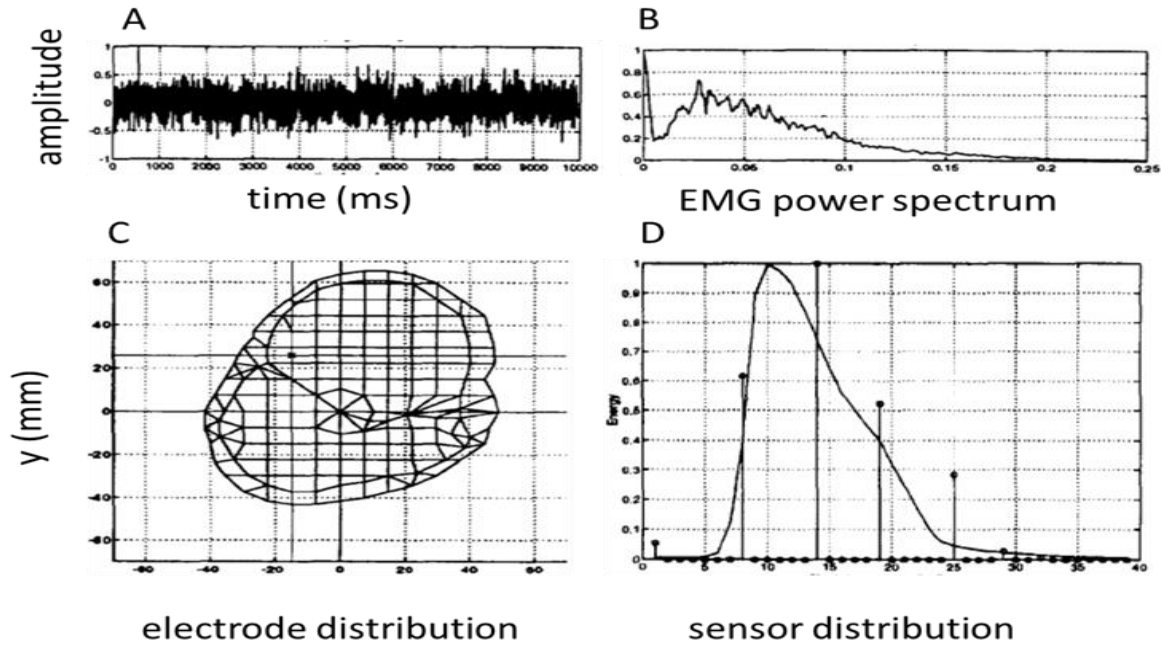
Figure 2.20: **A:** EMG signal; **B:** power spectrum of the signal **C:** Estimated source location (small dot) in the upper arm model created from a MRI image. **D:** Experimental data (vertical lines) compared with simulated results from identified source (from: Jessinger et al. [37] Figure 2).
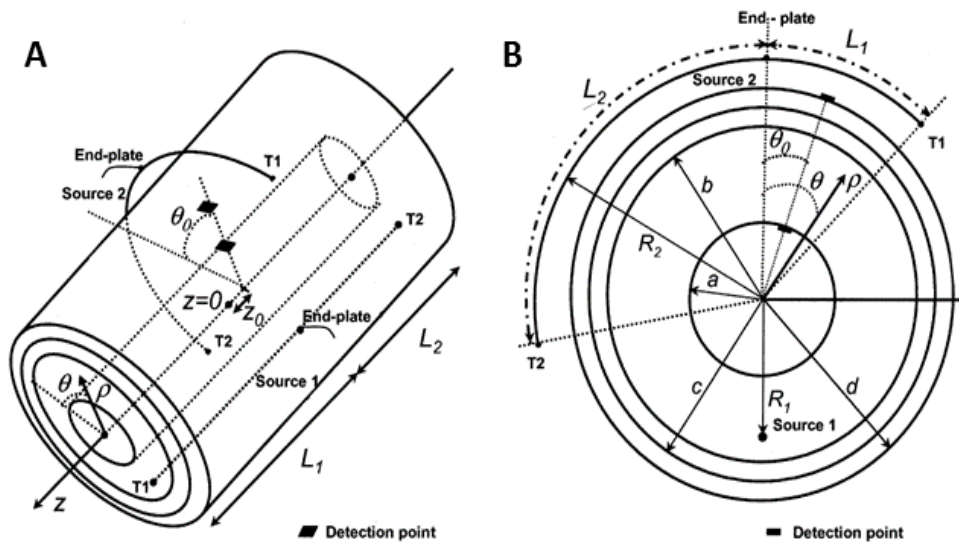


Figure 2.21 **A:** The model of volume conductor. Muscle fiber (source) can be situated in the both z and Θ direction of any layers. The detection points can be placed at the boundary of any two layers. $R_i$ (i:1,2) is the radial distance between the source and the center of the volume conductor, $L_i$ (i:1,2) represents the length between the source and the end-plate. Radial distances of different layers are shown as a, b, c, and d. **B:** Cross section of the model (from: Farina et al [38] Figure1).

A model for surface electromyography (EMG) signal generation in a 4 layers cylindrical volume conductor is proposed by Farina et al. in 2004 [38]. A spatio-temporal function is used to model the generation, spread, and transformation of the axon intracellular action potential (AP) at the end-plate in a muscular (AP) propagating along fibers up to the tendons. The source can be defined either longitudinally (for limb muscles) or radially (for sphincter muscles). Figure 2.21 illustrates geometry of the model in cylindrical coordinates ($\rho,\Theta,z$). The potential distribution over the skin, due to sources in the muscle was obtained with the Poisson equation in the frequency domain where low-pass spatial filters represent the anisotropic muscle tissue and the isotropic fat and skin layers. Results are at the effect that the sub-cutaneous tissue layers increase the detection volume in all directions and reduce its amplitude. To compensate the attenuation and widening of the signal due to the subcutaneous tissue, various recording electrode arrays could be used. The transfer functions of anisotropic muscle tissue and the isotropic layers of fat and skin were proposed.

In 2008, Van den Doel et al. [39] explored the mapping of the activity of individual muscles using surface EMG data from various recording sites which was named computed myography (CMG). The sEMG inverse problem was similar to surface electroencephalogram inverse problem. These sources of potential field are polarization waves know as intracellular action potentials (IAP) initiated at the neuromuscular junction and travelling along the individual muscle fibers. The conduction velocity (~3-5 m/s) is proportional to the radius of the muscle fibers. The motor unit action potential (MUAP) is the signal obtained from a motor unit (MU). The frequency content of surface EMG signals reach up to 500 Hz depending on the electrodes size.

As shown at the left of Figure 2.22, the steps for processing data are:

1) Segmentation of MRI data in order to make a 3D finite element model (FEM).
2) Write 3D volume conduction forward model of muscles to predict the surface voltages.
3) Solve the inverse problem through calculating the most likely current sources that can account for the acquired data.

(a) Systems diagram             (b) 3D geometry
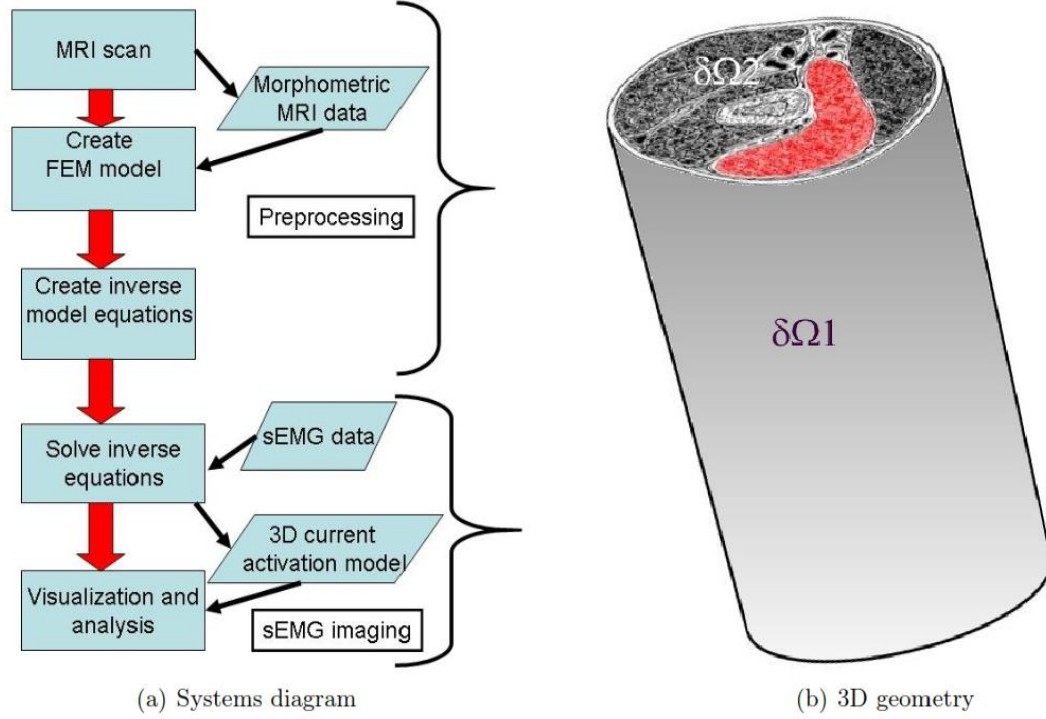
Figure 2.22: **Left:** The CMG system's chart. The thick red arrows represent sequential processing steps and the narrow black arrows represent data created or used. The rectangular boxes indicate processes and the skewed boxes indicate data. **Right:** A 3D domain $\Omega$ (including of muscle, fat and bone) with the physical boundary $\partial\Omega_1$ (gray) and the cut boundary $\partial\Omega_2$. (from: Van den Doel et al. [39] Figure1).

The electrostatic potential $u(x)$ satisfies the generalized Poisson partial differential equation (PDE) on the domain $\Omega$:.

$$\begin{cases} -\nabla(\sigma\nabla)u = I(x), in\ \Omega, \\ \nabla_n u = 0, \qquad on\ \partial\Omega_1, \\ \nabla_n u = -\ \Sigma u, on\ \partial\Omega_1. \end{cases}$$

Where $n$ is the outer-side normal at the boundary and $\sigma(\text{x})$ is the conductivity tensor which is non-isotropic in the muscles. I(x), the transmembrane current density is assumed to be proportional to the second spatial derivative of the muscle fiber intracellular action potential $V(x,t)$.travelling in the muscle fiber direction. At the right of Figure 2.22 (as in the formulas above), there are two types of boundaries: the $\partial\Omega_1$ term is the physical boundary which denotes the skin over the muscle where measurements can be done and the $\partial\Omega_2$ term is cut boundary which represents artificial

boundary of the model and also the $\Sigma$ term is an effective resistance at artificial boundary which represents the flow of currents toward inside and outside of the model.

To have a 3D representation of a section of the upper arm, a cross-section MRI of the upper arm (Figure 2.23 (a)) was segmented manually into subcutaneous fat and skin (lumped model), bone, brachialis, biceps, and triceps. Then, the geometry segmented image was imported in COMSOL and a 20 cm slice was extruded to create a 3D geometry. Different conductivities were assigned to different tissue. The geometry was meshed with tetrahedral elements. Experiments were done to investigate the ability to differentiate between the biceps activation and the one of the brachialis. Since the biceps is positioned closer to the electrodes array than large portions of the brachialis, activity of the biceps contributes more to the signal collected at the electrodes than the brachialis. The reconstructed sources were distributed throughout biceps and brachialis while allocating a large penalty term of 1000 for sources outsides the muscular tissue. They placed 5000 tripole sources in the biceps, in the brachialis or in both of them. The sources were vertically restricted to the middle 10 cm of the 20 cm 3D model in order to be far enough from the artificial boundaries.

In another set of experiments, the effect of bipolar (differential) recording which decrease crosstalk from distant sources was investigated. Experimental sEMG data was acquired from one healthy subject performing isometric flexion and extension with 12 electrode pairs encircling the upper arm (Figure 2.23(c)) at its middle length with the elbow flexed at 90° and the hand supinated. With the generic MRI image of Figure 2.23(a), the simulated data were consistent with the human data.

In a 2002 article, Lowery et al. [41] considered the upper limb as a purely resistive medium in which a source of activity was located. They studied the influence of skin, subcutaneous tissue and bone on the rate of decay of the EMG signals around the surface of a cylindrical model because those factors are important for estimating crosstalk in surface EMG signals. A FEM was used where the mesh of the interior regions was done with 3D tetrahedral elements (Figure 2.24).

(a) Anatomical image    (b) 3D geometry constructed    (c) Mesh and 12 sensors
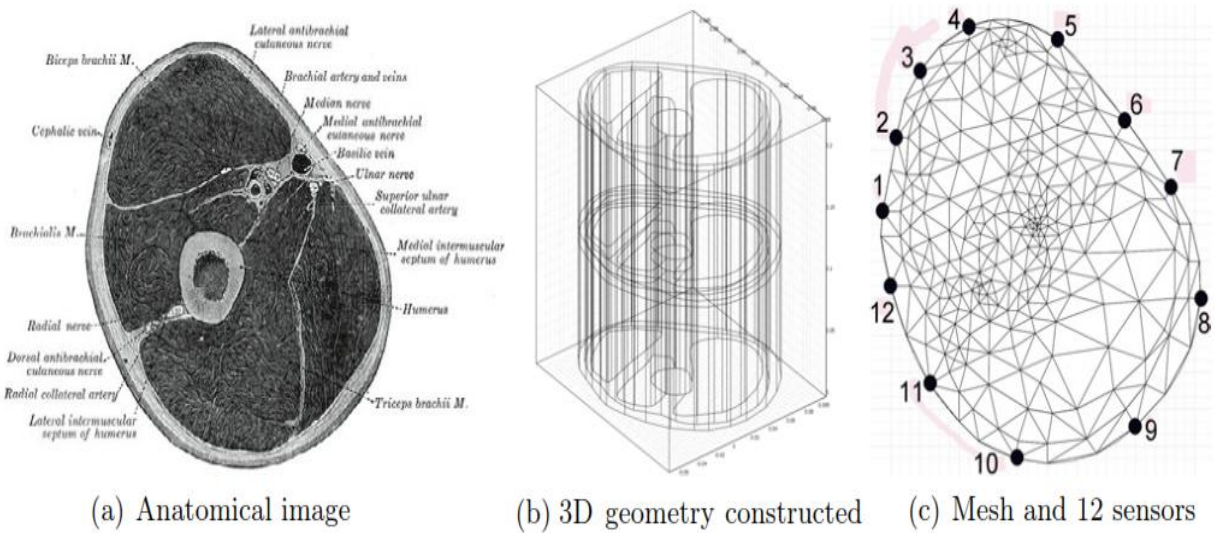
Figure 2.23: **(a)** Cross-section of an upper arm MRI which was segmented into anatomical regions like: brachialis, biceps, triceps, bone, fat and skin. **(b)** The 2D segmented image was then extruded to create a 3D geometry which was imported in COMSOL. Afterwards, the result was meshed via tetrahedral elements. The differential equations were discretized in COMSOL and conveyed to MATLAB to solve the inverse problem, either measured data or synthetic data, at the locations illustrated in the cross-sectional view of the mesh **(c)**, 5000 distinct current tripole sources, with different configurations, were placed in the upper arm muscles and 12 sensors surrounded upper arm model (from: Van den Doel et al. [39] Figure2).
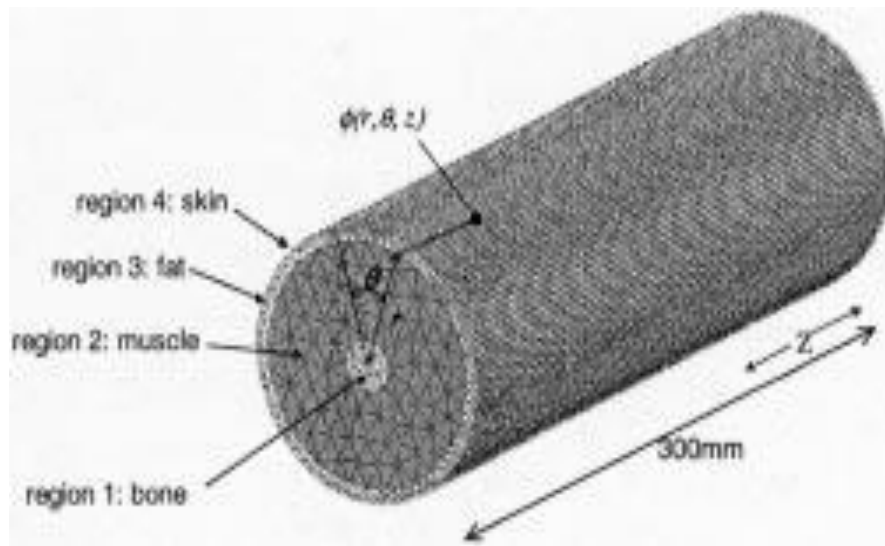


Figure 2.24: Finite-element multilayer model of the upper arm (from: Lowery et al. [41] Figure1).

Under assumption of a piecewise homogeneity throughout the model, Laplace equation was used to determine the potential distribution:

$$\Delta\phi(r,\theta,z) = \frac{\delta^2\phi(r,\theta,z)}{\delta r^2} + \frac{1}{r}\frac{\delta\phi(r,\theta,z)}{\delta r} + \frac{1}{r^2}\frac{\delta^2\phi(r,\theta,z)}{\delta\theta^2} + \frac{\delta^2\phi(r,\theta,z)}{\delta z^2} = 0$$

where $\emptyset(r,\theta,z)$ is the electric potential at each point of the volume conductor of radial r, angular theta, and axial position z. At the boundary of each two media, the continuity of electric current is assumed and the following condition is considered:

$$\sigma_1 E_{1n} = \sigma_2 E_{2n}$$

where $\sigma_1$ and $\sigma_2$ represent the conductivities of the first and second media respectively, $E_{1r}$ and $E_{2r}$ are the electric field of the first and second media respectively. At the interface between skin surface and surrounding media, the conductivity of surrounding media was assumed as zero (air). The volume conductor was assumed to have an infinite length. The transmembrane current-density $I_m(z)$ was applied to the surface of a muscle fiber having a diameter of 100µm located within the conducting muscle tissue. $I_m(z)$ was defined as a continuous function of axial distance z and orientated parallel to the skin surface. $I_m(z)$ was assumed proportional to the second derivative of the transmembrane voltage $V_m(z)$:

$$I_m(z) = \frac{\sigma_i \pi d^2}{4} \cdot \frac{d^2 Vm(z)}{dz^2}$$

where $\sigma_i$ is the intracellular conductivity and $d$ is the fiber diameter and $V_m(z)$ the algebraic formula of Rosenfalk for the transmembrane potential. Conductivity of different tissues (muscle, skin, fat, cortical bone, and cancellous bone) at the median frequency of a typical surface EMG signal (i.e. 100 Hz) was obtained from Gabriel et al. as in the 2014 paper. The potential of the node in the center of each electrode was assumed to be the potential of the electrode.

Five different models of the upper arm (Table 2.3) were considered. In Model II, a 2 mm-thick isotropic skin layer was placed on the outer rim layer while for Model III, skin was replaced by 5 of fat. In Model IV, the skin and fat thicknesses were 2 and 3 mm respectively. For Model V, a cylindrical bone with a radius of 10 mm was added and its position was changed from the center of the model up to near to the outer layer (Figure 2.25) where $b$ represents the distance between

center of the volume conductor and the bone center and $\Theta$ is the angular displacement of the bone relative to the vertical axis. The bone, assumed to be made of homogeneous cortical material or having at its center a less resistive cancellous material within a radius of 7 mm, was moved from the center of the conductor up to 2 mm under the muscle-fat border. The external radius of the volume conductor was 50 mm in each 5 models. To study the influence of subcutaneous fat tissue, its thickness was varied up to 18 mm while the muscle thickness was kept constant. Over the biceps, skinfold thickness ranged between 2 and 29 mm for males and from 2 to 45 mm for females. The model included bipolar electrodes with an interelectrode spacing of 20 mm aligned parallel to the muscle fiber direction.

Table 2.3: Composition of 5 models of Lowery et al. (Table.2 from [45])

|  | Model I | Model II | Model III | Model IV | Model V |
|---|---|---|---|---|---|
| Region 1 | muscle | muscle | muscle | muscle | bone |
| Region 2 | muscle | muscle | muscle | muscle | muscle |
| Region 3 | muscle | muscle | fat | fat | fat |
| Region 4 | muscle | skin | fat | skin | skin |
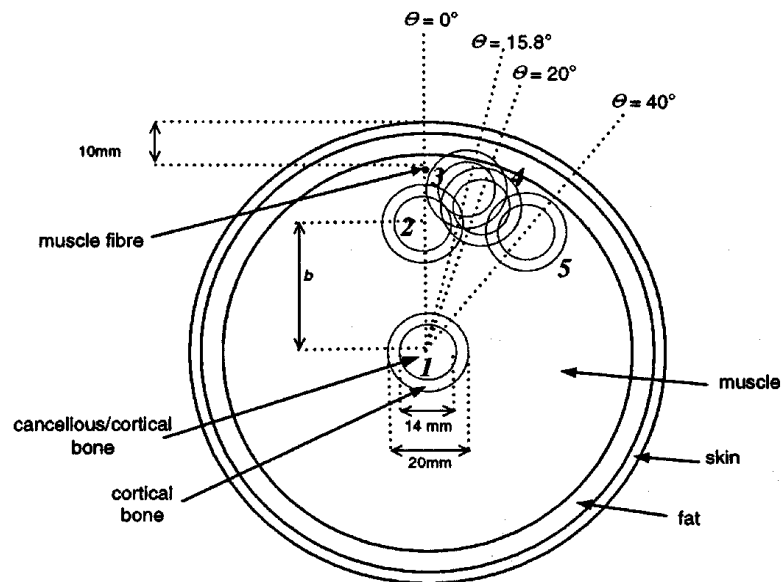


Figure 2.25: Cross section of the model with different bone tissue positions (from Lowery et al. [41] Figure2).
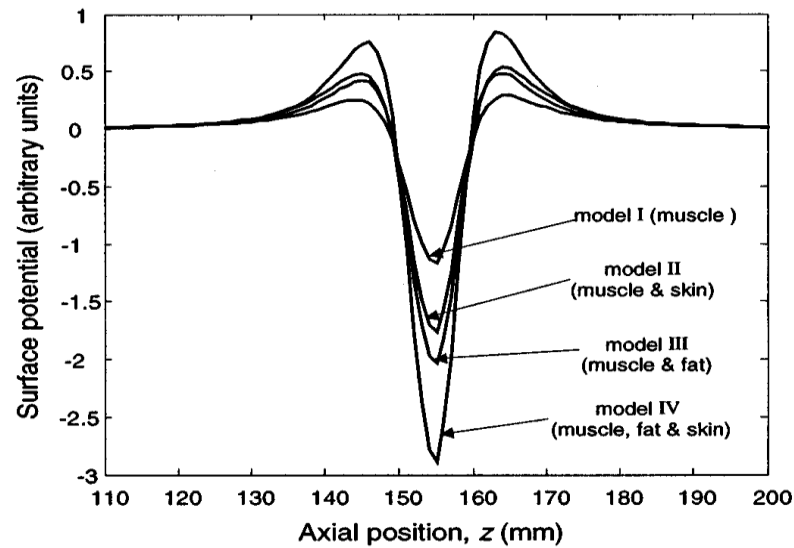
Figure 2.26: Waveform of action potentials detected at the surface directly above a fiber placed at a depth of 7 mm in models I–IV (from Lowery et al. [41] Figure3).

In Figure 2.26, action potential above a source located 7 mm deep in the muscle tissue, is compared for models I–IV. Altering the exterior layer of model I with a less conductive medium, like skin or fat, results in an increasing of the signal amplitude recorded over the surface. The variation of RMS value as the fiber depth is increased is shown in Figure 2.27 for various models. It was deduced that the 90% increase of the action potential RMS value was due to the presence of the fat layer.
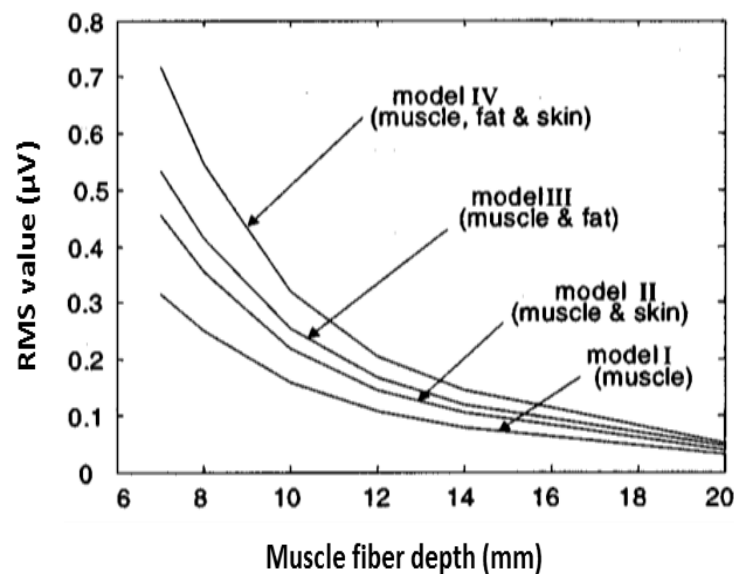


Figure 2.27: RMS value of action potential for 4 models as fiber depth increased from 6 to 20 mm (from Lowery et al. [41] Figure4).

For the homogeneous cortical bone and the bone with an outer layer of cortical bone and a core of cancellous one, the RMS value of the action potential over the surface were quite similar. Effects of bone position for both types of bone are illustrated in Figure 2.28.
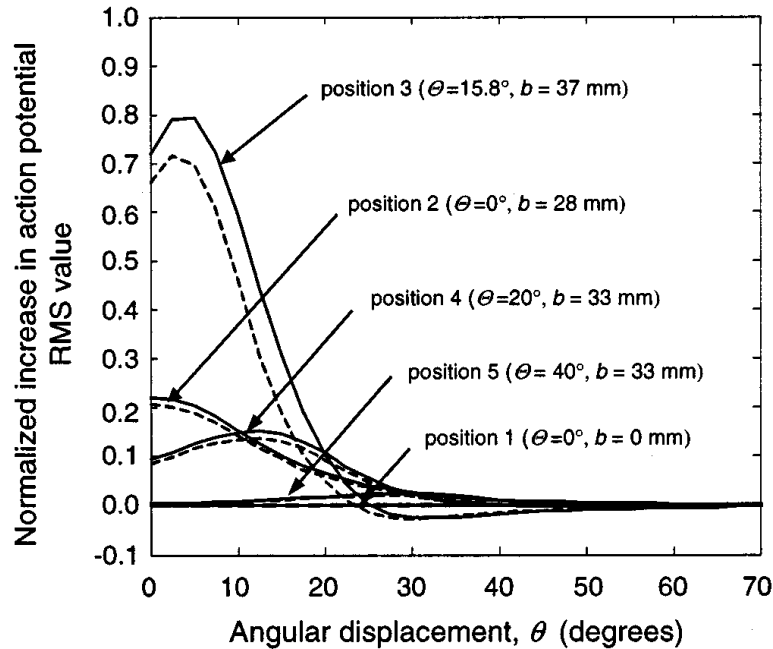


Figure 2.28: Effect of adding bone tissue on surface potentials RMS values. The bone was located at various places within the model. Solid lines indicate effect of cortical bone and dashed lines indicate results of cortical bone with a cancellous tissue core. Using the peak value, the results were normalized in a model without bone tissue and muscle fiber depth was set to 10 mm (from Lowery et al. [41], Figure 9).

An extension of that work appeared in 2004 (Lowery et al.[40]) where magnetic resonance images of the upper arm of a subject (Figure 2.29 (a)) were used to build a FEM model where fat, muscle, cancellous and cortical bone were introduced including the cephalic vein and brachial artery (Figure 2.29 (b)). They explored the effect of limb geometry and composition on surface potentials a FEM model with skin. In the simulations, conductivity and capacitive effects of the biological tissues were considered while inductive effects were assumed to be negligible. For the experiment, 16 pairs of electrodes were placed around the arm (Figure 2.29 (b). An idealized model was produced modeling the upper arm as a cylinder with concentric layers of skin, fat, muscle and bone (Figure 2.29 (c)). The diameter of each layer was the mean diameter of that tissue as measured on the MR image taken between the 2 rows of the recording electrodes. As can be seen in Figure 2.30, two sites of stimulation (A and B electrode pairs separated by 60 mm) were placed along fibers

direction on either side of the recording electrode pairs #4 and #7. A constant current sinusoidal source of 1 mA at 100 Hz was used. Such a current source, too small to stimulate the underlying muscle fibers, was used to verify if a 3D layer model of skin could be equivalent to a layer of 2D elements placed over the fat tissue. Experimental signals were compared to simulated data obtained from the detailed and idealized models.
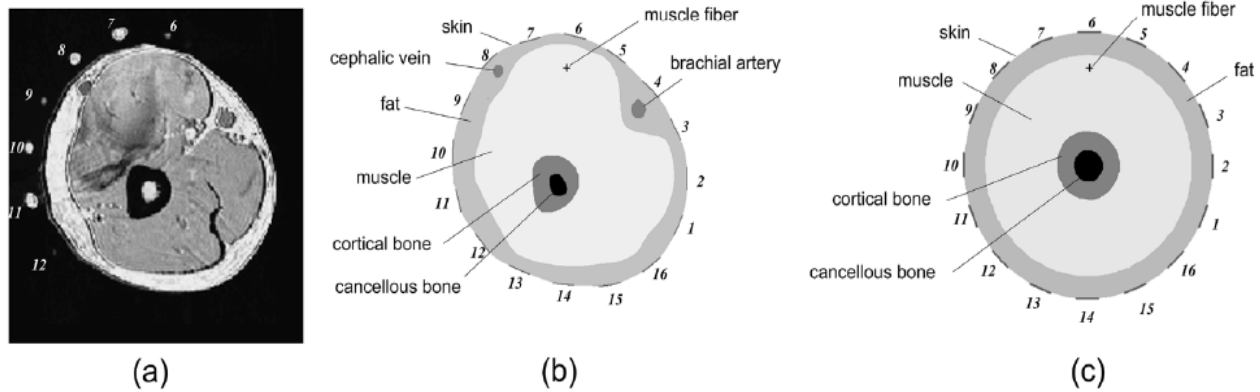


Figure 2.29: **(a):** MRI cross section of subject's right arm mid-way between surface electrode pairs. **(b):** Anatomically based FEM model of (a) around which position of the 16 recording pairs of electrodes appear as a small plate. **(c):** Idealized cylindrical model based on MRI shown in (a) (from: Lowery et al. [40] Figure1).

At the boundary of the model, average value of the electrical field was set at zero and a finite length was assumed with a ground put at the farthest node from the recording electrodes. Conductivity and permittivity for a surface EMG signal was chosen at 100 Hz. Muscle tissue was considered anisotropic both in conductivity and permittivity while bone and fat where isotropic as skin in spite of its laminar structure. Four different sets of values for conductivity and permittivity were tested. In the simulations, a transmembrane action potential travelling at 4m/s in a fiber located 14.5 mm below the skin was used. The current source was derived from the second derivative of an analytical model of the transmembrane potential.
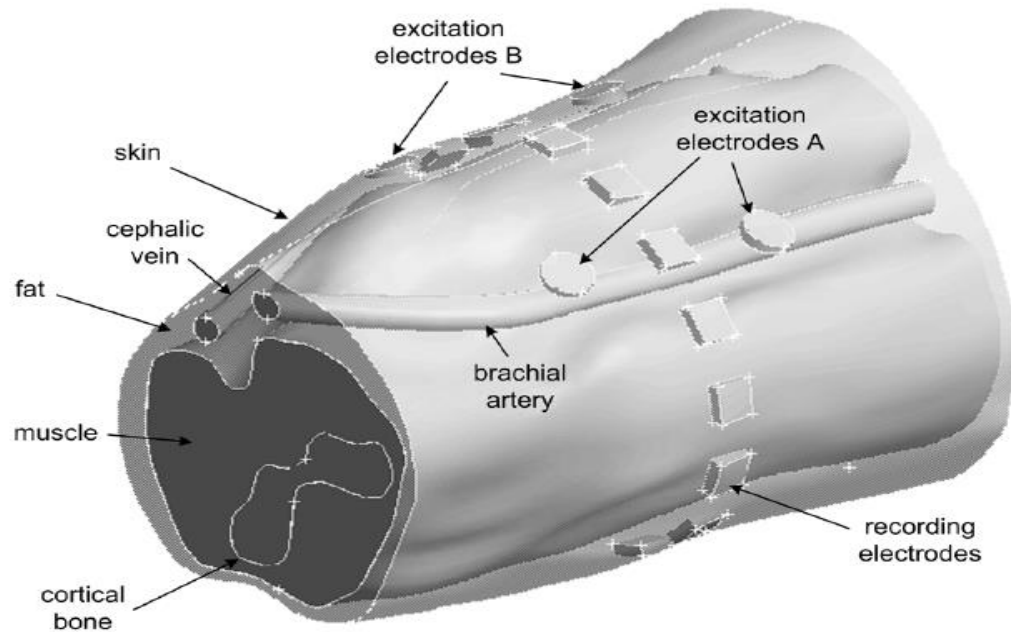
Figure 2.30: Anatomically based volume conductor model showing the tissue geometries around which surface recording electrodes as well as excitation electrode pairs A and B are displayed (from: Lowery et al. [40] Figure2).

Many simulated results are shown in Figure 2.31 for various conditions. The most marked change in surface potentials occurred for the signal recorded above a vessel. This occurred due to the presence of the brachialis artery or the cephalic vein which caused a shunt and decreased surface potential above them. When in the model they replaced blood vessels with fat, an increase in signal amplitude was observed under each electrode. Effects of muscle fibers curvature were studied. When electrodes were close to a source, the recorded action potentials were similar for straight and curved muscle fiber. However for electrodes located far from the source, the action potential for a straight muscle fiber were closer than for a curved muscle fiber when an ideal cylindrical limb model is used. When only qualitative surface EMG signal characteristics are under study, an ideal cylindrical model with appropriate tissue thicknesses provides a very good approximation.
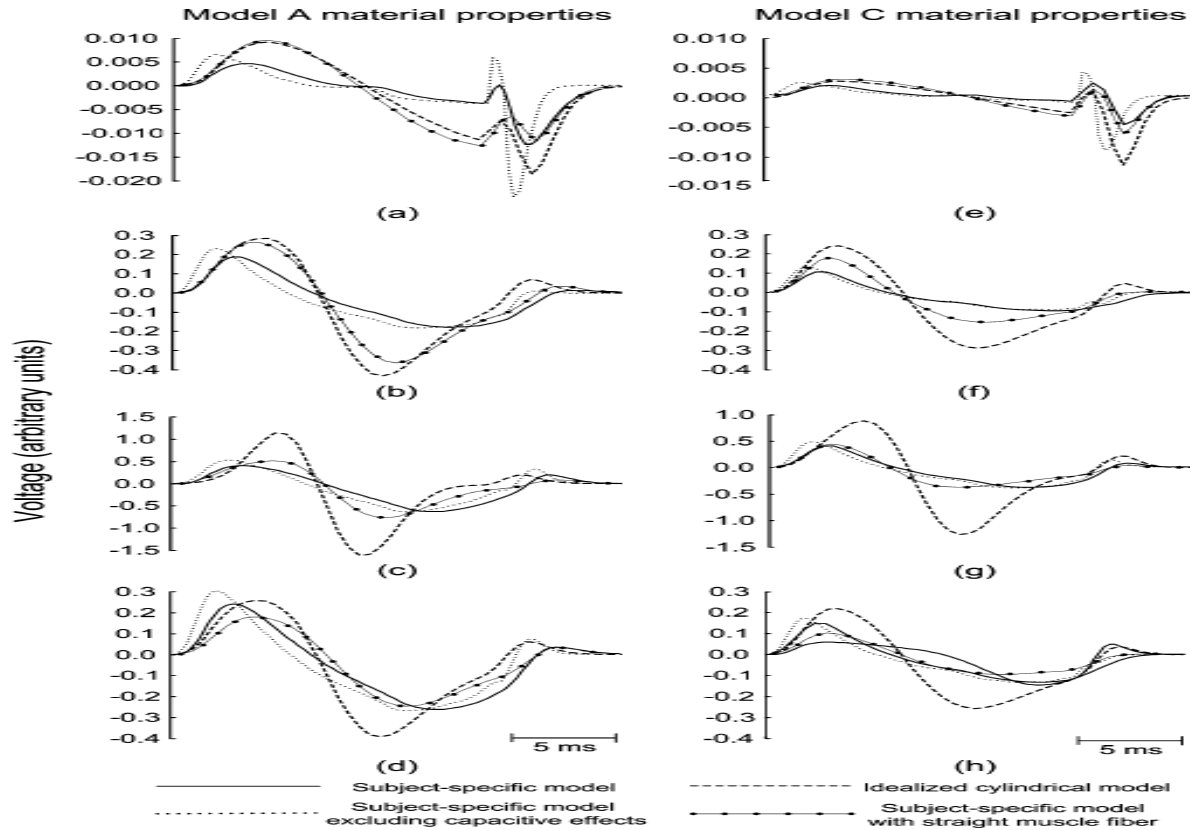
Figure 2.31: Simulation results of surface action potentials for a fiber located 14.5 mm under the skin surface below electrode #6. Action potentials are represented at different electrode locations for the subject anatomical model including resistive and capacitive material properties (solid line), completely resistive material properties (dotted line), a straight muscle fiber (dot-dashed line) and for the corresponding ideal cylindrical model (dashed line). (a) Electrode 2, (b) Electrode 5, (c) Electrode 6, (d) Electrode 7, (e) Electrode 2, (f) Electrode 5, (g) Electrode 6, (h) Electrode 7 (from: Lowery et al. [40] Figure4. Models A and C refers to the characteristics shown in their Table 1).

Having used a realistic arm anatomy they modelled surface EMG in various conditions and when they compared the results with those obtained with an idealized circular model where subcutaneous layers are adequately represented, no great differences was observed in the rate of decay of the surface action potential amplitude.

Out of those articles, the simulations of Lambin & Troquet and those of Saitou et al. attracted our attention because they could be used to check that the COMSOL software was appropriate for our simulations. It is based on the articles of Lowery et al., that modelling the upper arm as a cylinder was found adequate for locating dipoles within the 6 compartments of the biceps.

# CHAPTER 3   METHODS

In this chapter, information of the subjects who participated in experimental tests will be presented and the peak fitting approach to find dipole characteristics are explained.  Our simulations were done with COMSOL Multiphysics. So a brief description of this software and its local network link between COMSOL and MATLAB (livelink MATLAB) will be exposed.

## Experimental EMG signals

We analyzed EMG data that have been previously collected from 10 healthy right handed subjects (Nejat 2012 [43]). Some of their characteristics are presented in Table 3.1.

Table 3.1: Subjects characteristics. BMI: body mass index.

| Subject ID | Gender | Hight (cm) | Weight (kg) | BMI | Age | Arm circumference (cm) | Biceps length (cm) | Biceps width (cm) |
|---|---|---|---|---|---|---|---|---|
| S1 | F | 160 | 57.5 | 22.5 | 33 | 26.5 | 16.5 | 11 |
| S2 | M | 146 | 52 | 24.4 | 32 | 27 | 16.5 | 9 |
| S3 | F | 163 | 63.5 | 24 | 31 | 26.5 | 16 | 9 |
| S4 | F | 169 | 70 | 24.5 | 27 | 30 | 19 | 11 |
| S5 | M | 184 | 68 | 20.1 | 33 | 25 | 19 | 9.5 |
| S6 | M | 170 | 72 | 24.9 | 22 | 30 | 17 | 15 |
| S7 | F | 167 | 60 | 21.5 | 33 | 26.5 | 16 | 9 |
| S8 | M | 175 | 69 | 22.5 | 20 | 31 | 16 | 13.5 |
| S9 | F | 165 | 55 | 20.2 | 29 | 26.5 | 13 | 11 |
| S10 | M | 176 | 75 | 24.2 | 29 | 28 | 16 | 12.5 |
| Average | | 167.5 | 64.2 | 22.88 | 28.9 | 27.7 | 16.5 | 11.05 |

As for the EMG data collection, 5 pairs of surface electrode were placed across the SH and 5 others over the LH of BB of subjects' right upper arm (Figure 3.1A). Lower row of electrodes was 10 mm above the middle of the BB where the neuromuscular junction zone is located. Electrodes were made of gold disks of 6 mm in diameter mounted on an adhesive medical tape with a center-to-center distance of 15 mm horizontally and vertically (Figure 3.1B). Two body and 3 hand positions were experimented as shown in Figure 3.1C. In the seated position, the arm was close to the trunk and elbow flexed at ~$100^0$. To prevent muscular fatigue, contractions at 20% of maximum

voluntary contraction (MVC) level were produced. In the standing up posture, the arm was 90°
abducted and held horizontally in the coronal plane with a 1 kg load attached at the wrist level
which corresponded to ~20% MVC of the seated position. In both body positions, EMG signals
were collected while the subject's hand was either in pronation, neutral position or supination. In
each condition, 3 to 4 isometric and isotonic contractions of 5 s long were produced and a mean
EMG signal obtained. The root mean square (RMS) of each of the 10 mean signal was used to
represent a potential distribution across the BB as shown in Figure 3.2.
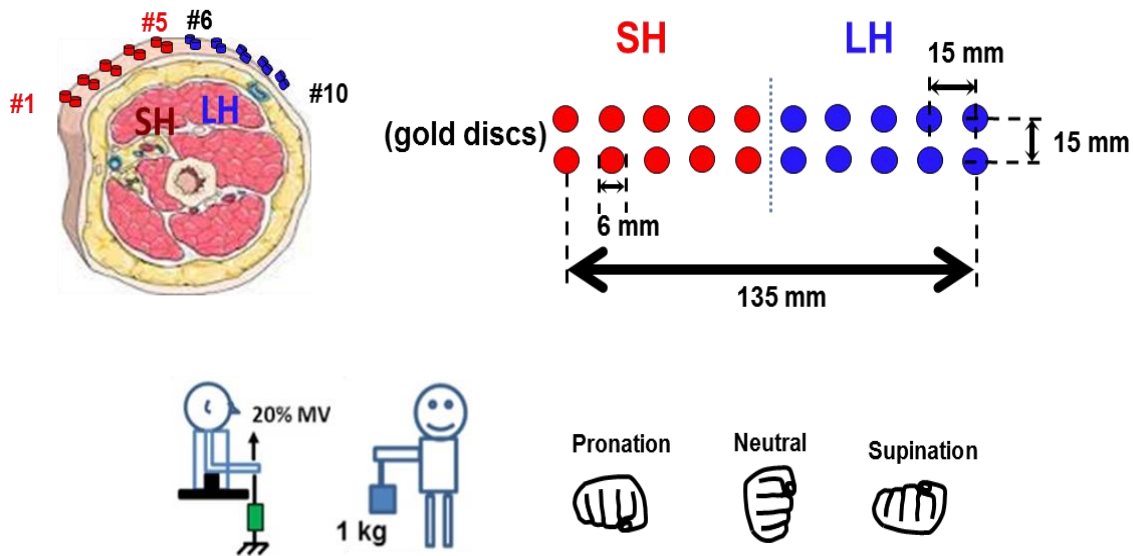


Figure 3.1: Experimental conditions. **A**: Cross section illustration of upper arm showing humerus
bone, muscle tissue, subcutaneous fat and skin layers with the short head (SH) and long head (LH)
of the BB muscle. Five pairs were placed across the SH and 5 others over the LH. **B:** Electrode
array used for data collection. **C:** Seated and standing up positions and hand position experimented.

To get a first estimate of the dipoles position within a cylinder representing the arm, and their
relative intensity a peak fitting method derived from the identification of many MU trains from
intramuscular recordings (Florestal, Mathieu, McGill, 2009 [44]) was used. A finite element model
(FEM) of an homogenous cylinder representing the upper arm was used in simulation with 360
electrodes along its circumference at a given observation line (Figure 3.3A) to detect activity
resulting from dipoles travelling at a constant speed inside the model.
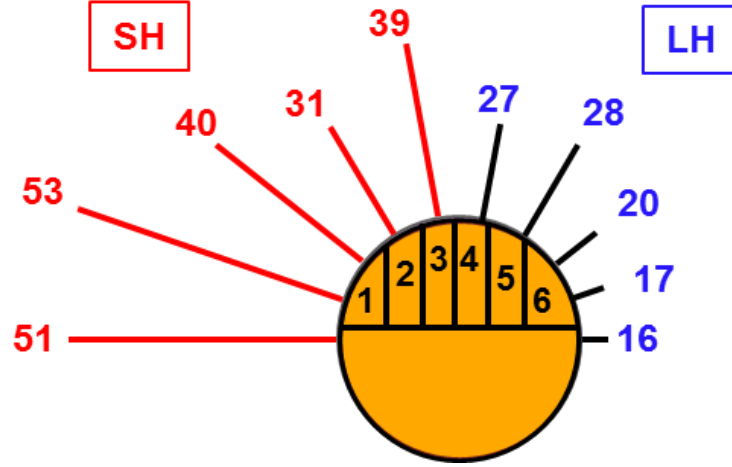
Figure 3.2: One-layer upper arm model with the 6 biceps compartments. Length of the spokes around the SH and the LH are proportional to each RMS values (µV) of the 10 EMG signals[2]. (Subject S2 seated position and hand pronated).

As illustrated in B panel for 2 dipoles, their radial and angular positions within the cylinder was $\rho$ and $\varphi$ respectively while their relative intensity was proportional to the diameter of the red bullets. Potentials around the cylinder were obtained by the Okada's [30] equation:

$$V\left(\rho,\phi,z\right) = \frac{-p_z}{a\,\pi\,\sigma}\sum_{n=0}^{\infty}\frac{n\,\pi}{a}\sin\left(\frac{n\,\pi\,z'}{a}\right)\cos\left(\frac{n\pi z}{a}\right)\times$$

$$\sum_{m=0}^{\infty}\left[K_m\left(\frac{n\pi\rho}{a}\right) - \frac{K_m'\left(\frac{n\pi b}{a}\right)}{I_m'\left(\frac{n\pi b}{a}\right)}I_m\left(\frac{n\pi\rho}{a}\right)\right]I_m\left(\frac{n\pi\rho'}{a}\right)\cos\left(m\left(\phi-\phi'\right)\right)$$

where V($\rho$, $\varphi$, z) is desired potential point from the location P'($\rho'$, $\varphi'$, z') of the current source, $a$ is length of the cylinder, $K_m$ and $I_m$ are modified Bessel functions of order m. Many simulations were performed and it was found, in particular, that as a dipole position got nearer to the cylinder center (panel C), its rectified signal amplitude detected around the cylinder decreased (panel D), and by normalizing their amplitudes the width of each curve got larger as the dipole approached the cylinder center (panel E).

---

[2] How RMS values were obtained from EMG records is presented in Appendix **C**

Having a solution for the forward solution, the following steps were oriented toward the inverse solution, i.e. finding the dipole(s) at their origin of the simulation results. As shown in Figure 3.4A the potentials obtained around the cylinder for the 2 dipoles of Figure 3.3 are linearly plotted from 0° to 360° and from such a curve, changes between a positive and a negative slope are used to detect peaks the position of which gives the angular position ($\varphi$) of each dipole (panel B) while the width of the peaks (panel C), provides their radial position ($\rho$) as taken from the normalized curves (Figure 3.3E). Finally the amplitude of the peaks are normalized to make their sum equal to one (Figure 3.4D).
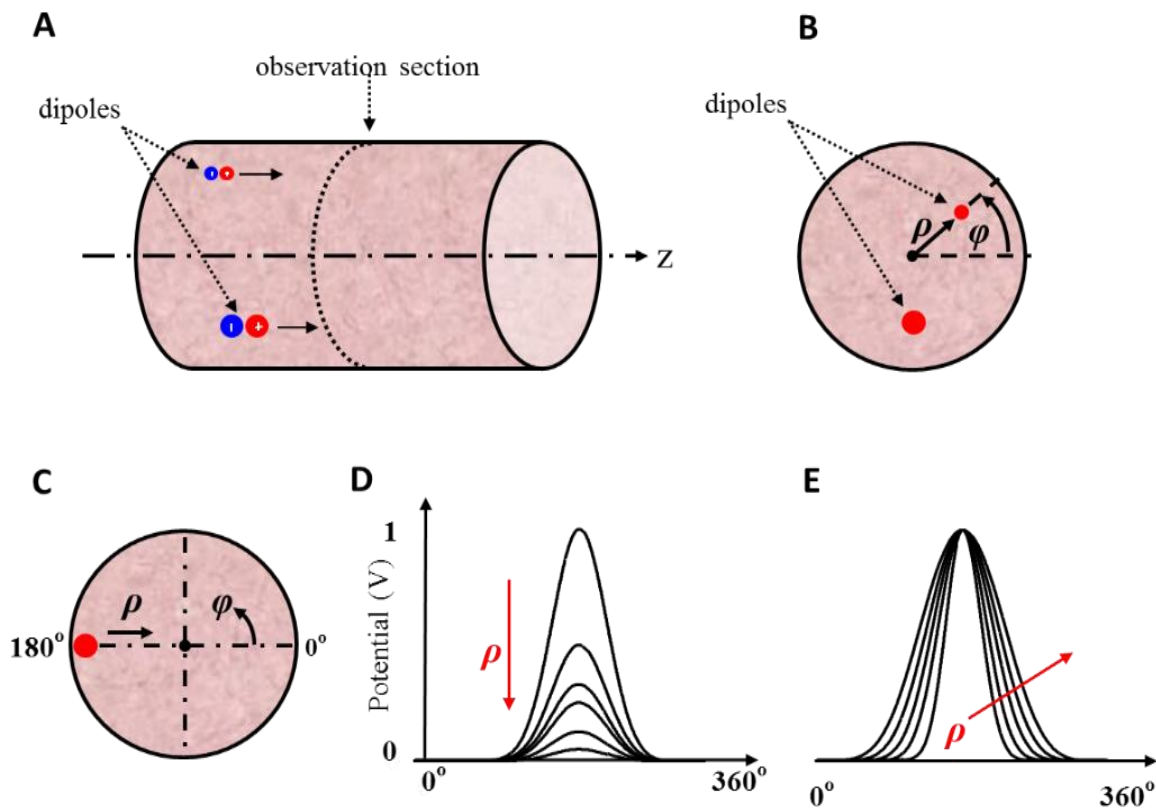


Figure 3.3: **A:** Dipoles moving within an homogeneous cylinder toward an observation section where potentials are measured **B:** Radial and angular position of the dipoles shown as bullets with a size proportional to their relative intensity. **C:** a dipole displacement from the cylinder border toward its center to obtain potentials around the observation section. **D**: potential distribution amplitude of the rectified signals as the dipole gets closer to the cylinder center. **E:** By normalizing the peak amplitudes of the curves, their width is associated to the dipole radial position ($\rho$).
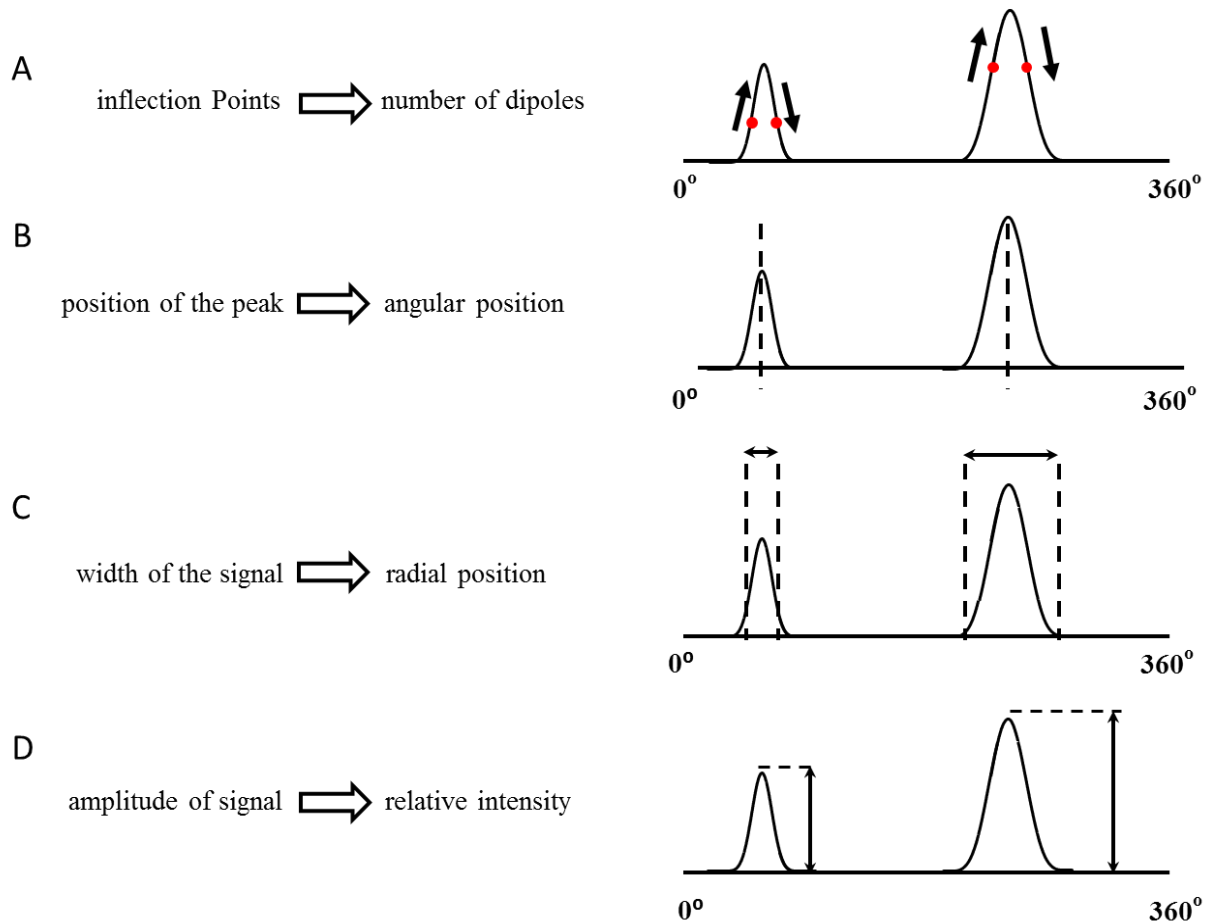
Figure 3.4: Identification of the dipoles' characteristics. **A:** use of positive and negative slopes to detect peaks associated to the number of detected dipoles. **B:** Position of the peaks provides the dipoles angular position ($\varphi$). **C:** Width of the peaks is associated to the radial position ($\rho$) of the dipoles. **D:** Peak amplitude is used to establish the relative intensity of each dipole.

## Simulations

The COMSOL multiphysics software (version 4.4 and 5.1) and its AC/DC library were used for our simulations. First, we checked the results obtained for a homogenous single medium within a cylinder with the peak fitting method and then move to a more elaborate arm model where muscle anisotropy was considered. As often done, the upper arm was modelled as a cylinder. From the measures obtained from one of our subject (S1), the cylinder height was 165 mm and its radius was 42.1 mm. A dipole (red dot) was inserted in the cylinder at $\rho$, $\varphi$, z ($\rho$ = radial position, $\varphi$ = angular position, z= height in the cylinder) and the voltage generated on the border of the cylinder was measured. With an intensity of 1 μA·m for a dipole and each measurement displayed in mm, signals

reaching the electrodes were in the mV range. As shown in Figure 3.5, a 1-layer and a 4-layer upper arm model were tested. Around them, 10 pairs of differential electrodes were used: lower row was at 75 mm from the bottom and the upper one 15 mm above and each vertical pair was separated by 15 mm. From each vertical pair of electrodes a differential signal was calculated. The electrical conductivity (S/m) considered for the biological tissues are those mentioned in Table 2.1(p.17) of the previous chapter.
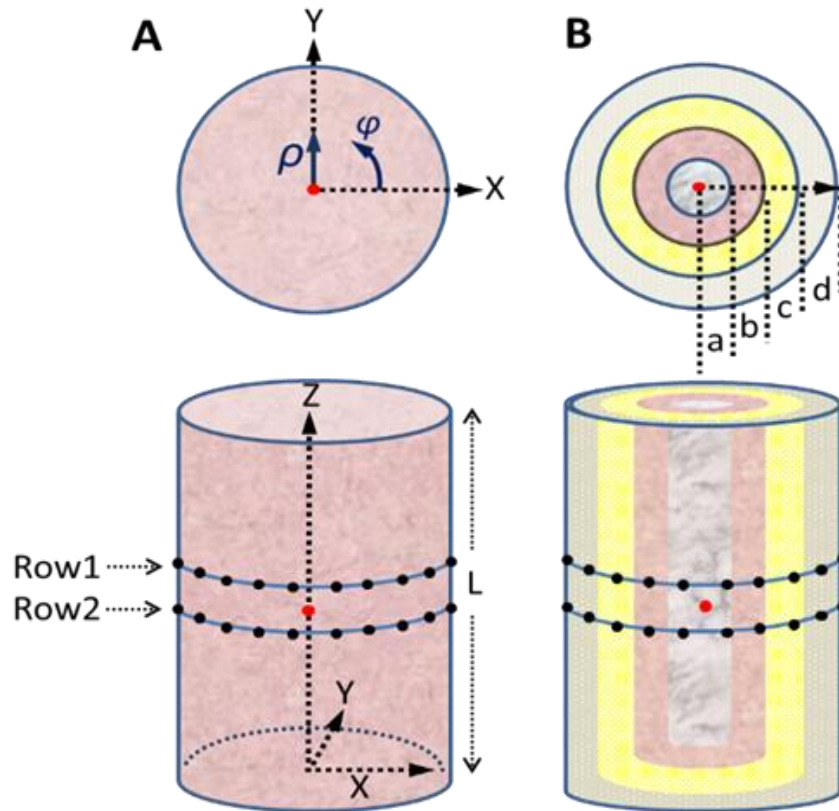


Figure 3.5: **A:** 1-layer model consisting only muscle in a cylinder; **B:** 4-layer model representing the skin, the fat layer, the muscle tissue and the humerus bone. In this figure, an electric dipole (●) is placed at (X=0,Y=0, Z= 82.5 mm) and the 2 rows of 10 electrodes are located at 90 mm (Row 1) and 75 mm (Row 2). The horizontal distance between each electrode pair is 15 mm. Approximately half of the cylinder circumference is covered by the electrodes.

Since the stationary solver of COMSOL was used, the relative permittivity of the biological tissues was ignored. Range in resolution for the 2 smallest pre-set mesh size used for our modeling are shown in Table 3.2.

Table 3.2 : Resolution of the 2 pre-set mesh sizes that were used.

| | Extra fine mesh | Extremly fine mesh |
|---|---|---|
| Maximum element size (mmm) | 8.73 | 4.99 |
| Minimum element size (mmm) | 0.374 | 0.0499 |

The FEM of one of our subjects (S6) consisted of 8360601 tetrahedral elements and 116970 triangular elements. These values varied between subjects due to the number of dipoles, the length of the biceps and its circumference.

## COMSOL windows

Known as FEMLAB before 2005, COMSOL multiphysics is used in many fields of study. With this simulation software finite element models (FEM) can be build, application programing interfaces (APIs) are used and partial differential equations (PDEs) solvers are available. With the LiveLink option, users can share the results with other software such as Matlab, Microsoft Excel, computed-aided design (CAD) or electronic CAD (ECAD) ones. The COMSOL APIs facilitate use of JAVA to drive COMSOL throughout compiled code. With COMSOL, 2D CAD/ECAD file should be transformed into a 3D object to be prepared for performing finite element analysis (FEI). Figure 3.6 illustrates the overal outline of the desktop.

To set up a model, the model wizards or a blank model can be used. In model wizard, dimension of the model, physics and interested module (e.g. AC/DC module) and domain of study (stationary, frequency, time, etc.) are specified. In the blank model, no predefined options are offered.  In the model builder section, the model and its components are defined. The model tree, as shown in Figure 3.6 provides a full access to entire pre/post processing functional operations: defined variables and parameters, designed geometry, materials, physics settings, boundary conditions, type of studies (stationary, frequency, time, etc…), solvers, results, plots, etc. It is also possible to include external equations or materials' properties to the main model.
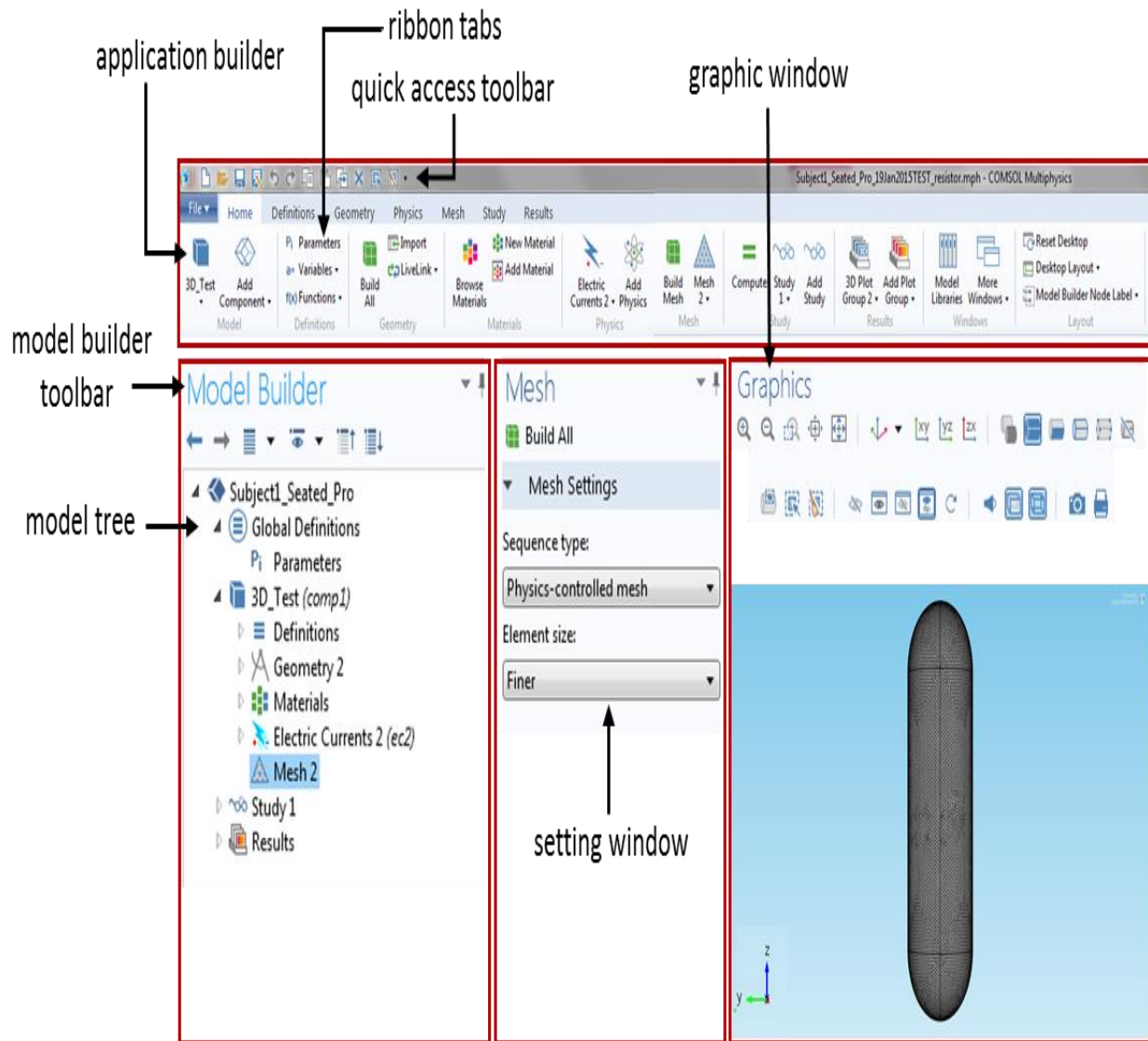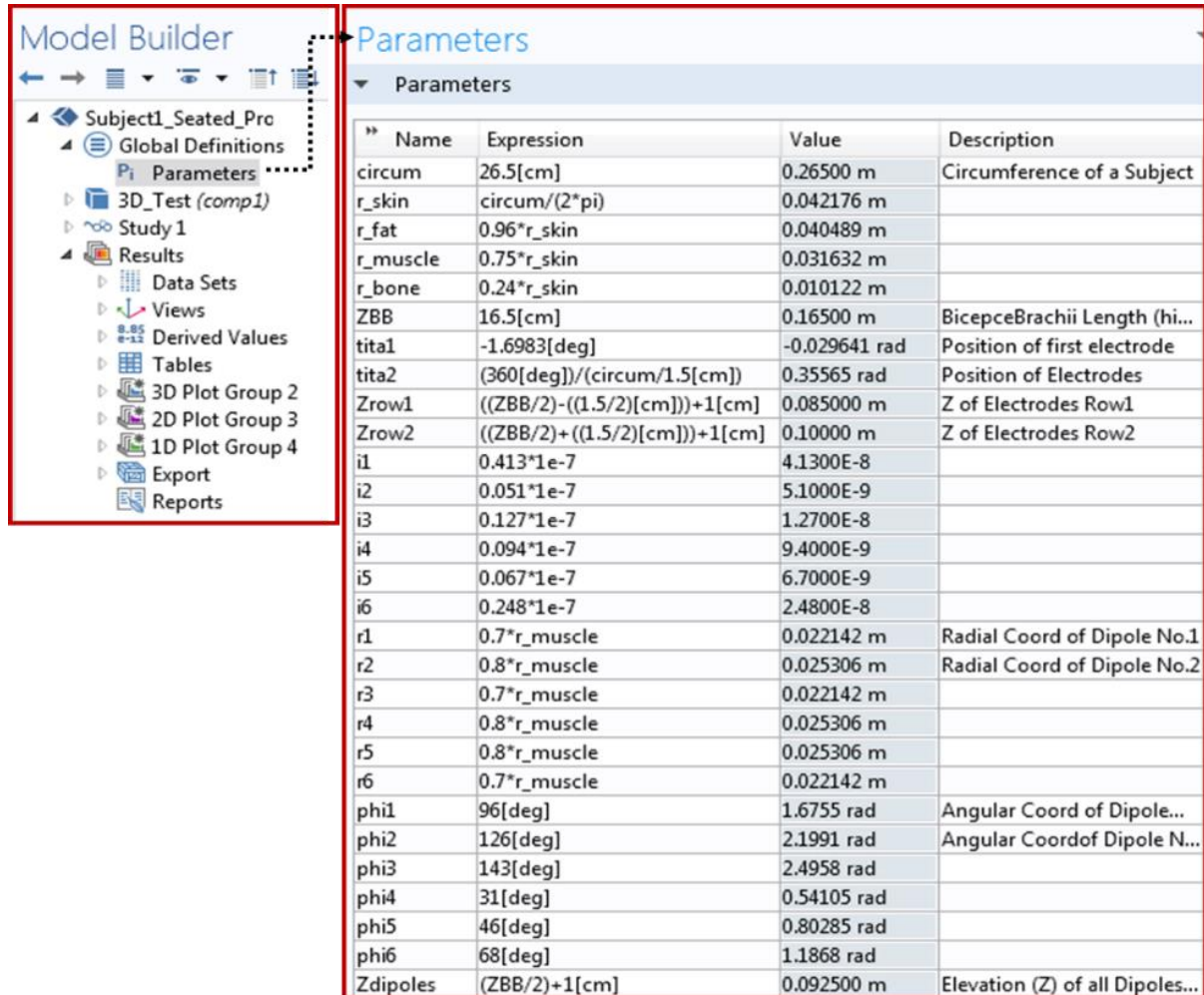
Figure 3.6: COMSOL multiphysics main desktop sections.

In its simplest form, our upper arm model consisted in a single cylinder representing the muscle tissue and in a more elaborate one as 4 concentric cylinders representing the skin, the fat layer, the muscular tissue and the humerus bone. Conductivity of each of those biological tissues at a frequency of 100 Hz were added to material properties. In our simulations, activity of many MUAPs in a given location where represented by a current dipole. After the model setup, the first

step is as shown in Figure 3.7 to define parameters like subject's circumference, length of the BB, electrodes and dipoles positions, etc.



| Name | Expression | Value | Description |
|---|---|---|---|
| circum | 26.5[cm] | 0.26500 m | Circumference of a Subject |
| r_skin | circum/(2*pi) | 0.042176 m | |
| r_fat | 0.96*r_skin | 0.040489 m | |
| r_muscle | 0.75*r_skin | 0.031632 m | |
| r_bone | 0.24*r_skin | 0.010122 m | |
| ZBB | 16.5[cm] | 0.16500 m | BicepceBrachii Length (hi... |
| tita1 | -1.6983[deg] | -0.029641 rad | Position of first electrode |
| tita2 | (360[deg])/(circum/1.5[cm]) | 0.35565 rad | Position of Electrodes |
| Zrow1 | ((ZBB/2)-((1.5/2)[cm]))+1[cm] | 0.085000 m | Z of Electrodes Row1 |
| Zrow2 | ((ZBB/2)+((1.5/2)[cm]))+1[cm] | 0.10000 m | Z of Electrodes Row2 |
| i1 | 0.413*1e-7 | 4.1300E-8 | |
| i2 | 0.051*1e-7 | 5.1000E-9 | |
| i3 | 0.127*1e-7 | 1.2700E-8 | |
| i4 | 0.094*1e-7 | 9.4000E-9 | |
| i5 | 0.067*1e-7 | 6.7000E-9 | |
| i6 | 0.248*1e-7 | 2.4800E-8 | |
| r1 | 0.7*r_muscle | 0.022142 m | Radial Coord of Dipole No.1 |
| r2 | 0.8*r_muscle | 0.025306 m | Radial Coord of Dipole No.2 |
| r3 | 0.7*r_muscle | 0.022142 m | |
| r4 | 0.8*r_muscle | 0.025306 m | |
| r5 | 0.8*r_muscle | 0.025306 m | |
| r6 | 0.7*r_muscle | 0.022142 m | |
| phi1 | 96[deg] | 1.6755 rad | Angular Coord of Dipole... |
| phi2 | 126[deg] | 2.1991 rad | Angular Coordof Dipole N... |
| phi3 | 143[deg] | 2.4958 rad | |
| phi4 | 31[deg] | 0.54105 rad | |
| phi5 | 46[deg] | 0.80285 rad | |
| phi6 | 68[deg] | 1.1868 rad | |
| Zdipoles | (ZBB/2)+1[cm] | 0.092500 m | Elevation (Z) of all Dipoles... |

Figure 3.7: Desktop view for the parameters used to design our upper arm model.

In the geometry section (Figure 3.8), predefined tools can be used to build the desired model. In the material section (not illustrated), a library of numerous mediums with their characteristics is offered and it is also possible to include others materials of interest.

Using the AC/DC module, a dipole is only defined as a point without any distance between its poles. Electric current was chosen to define our current dipoles intensity. Potentials detected at each electrode position on the skin layer are obtained with a solver (stationary, frequency, time,

etc.) and the results can be presented as Tables or as 2D/3D figures. Brief, intermediate, complete or custom reports can be produced.
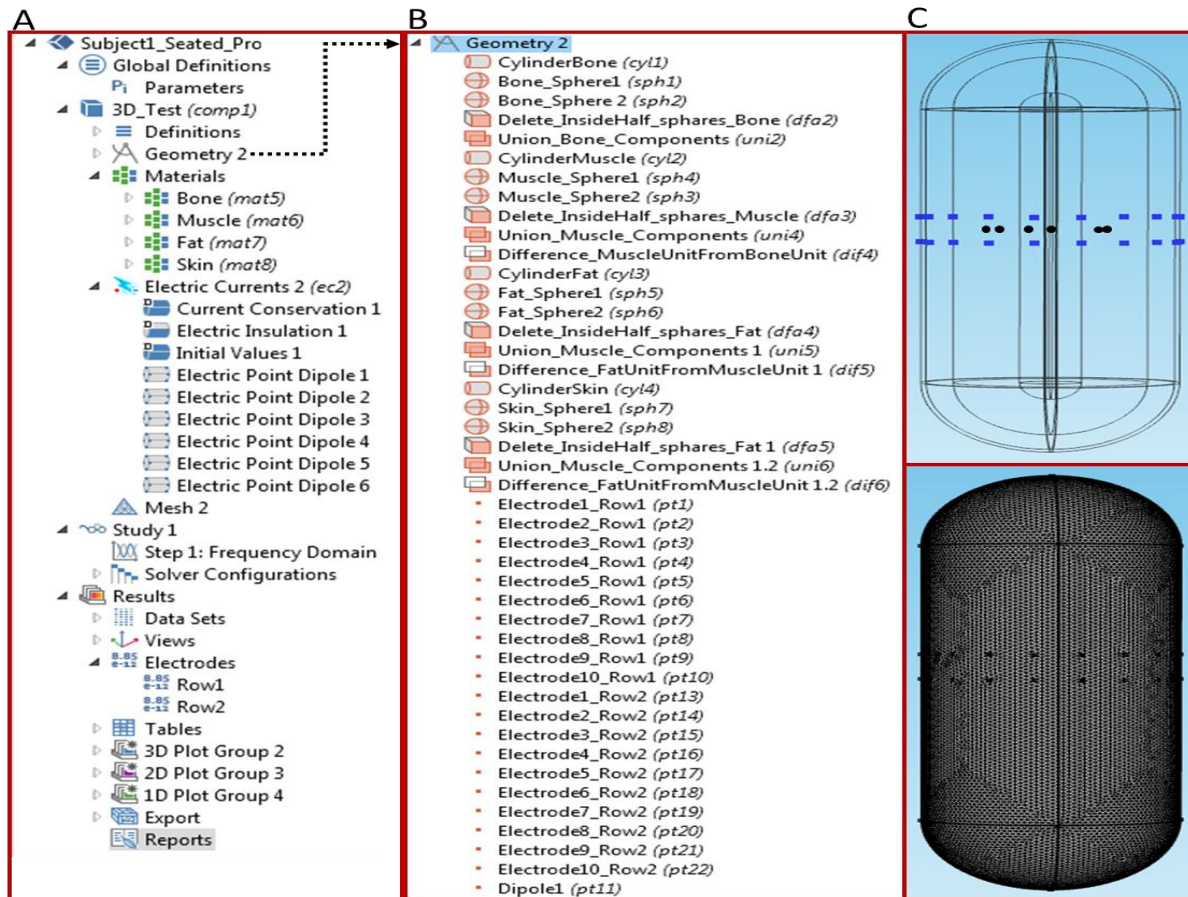


Figure 3.8: **A:** Desktop view of different sections concerning our model. **B:** Geometry information for the 4-layer model. **C:** In the top panel, the 10 electrodes pairs over the skin layer are illustrated with the two rows of electrodes and between them the 6 black dots represent as many dipoles inserted in the muscular tissue. Each dipole in the model represents a bundle of many muscle fibers' dipoles. In the bottom panel, an image of the mesh model of our upper arm model with electrodes locations. At the model extremities, hemispheres were added to get smoother signals at those areas.

## COMSOL and MATLAB

With COMSOL programing, each section (e.g. variables, geometry, materials, mesh resolutions, etc.) have to be manually entered and the simulation results have to be transferred to MATLAB for display. Due to human errors, accuracy of the results is not guaranteed and errors debugging is

time-consuming. However, COMSOL programming through Matlab scripts is achievable by using the Livelink for Matlab[3] server link the interface of which is shown in Figure 3.9. This expand modeling ability by providing an interface where all COMSOL sections can be monitored and simulation results observed directly. Additional information on this topic is easy to get by consulting the COMSOL webpage.
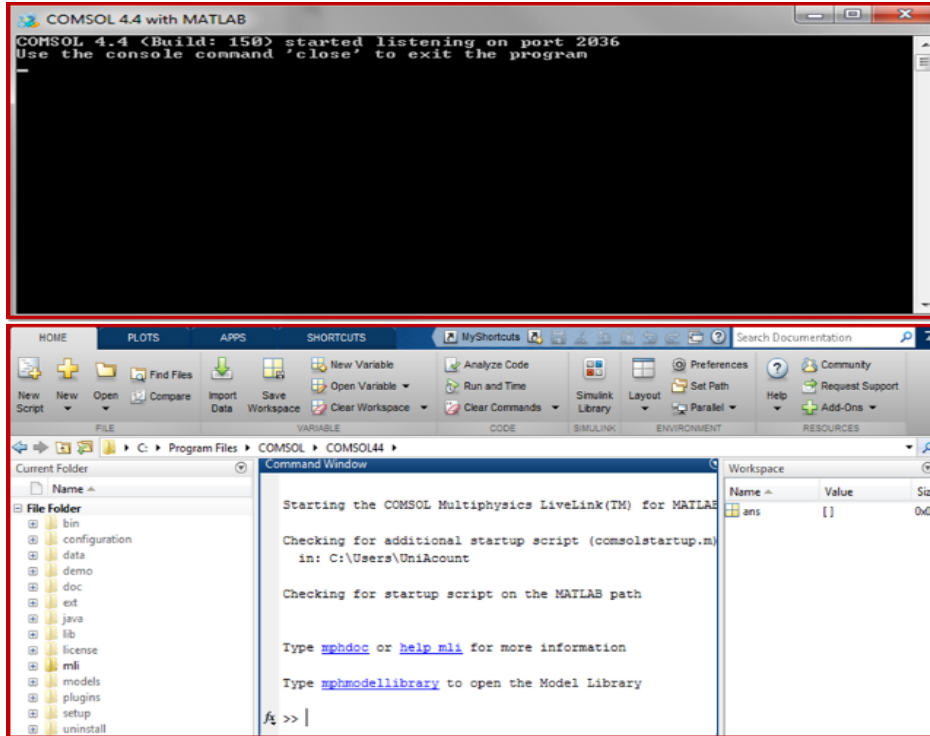


Figure 3.9: Upper panel: LiveLink for Matlab black panel connecting COMSOL to Matlab. Lower panel: Matlab is accessed with LiveLink and communicate with this link.

## Scaling factor

To graphically display a signal a scaling factor is needed. In our case, a RMS value $x$ was associated to a length $y$ on a graph by using:

$$y = m_N + \{(x - m_d) * (M_n - m_N)/(M_d - m_d)\}$$

where $m_n$ and $M_n$ are the minimum and maximum length to be used on the graph and $M_d$ and $m_d$ are the maximum and minimum value of the RMS values. We used 1.2 and 3.2 as $m_n$ and $M_n$. In Table 3.3 for example, 10 RMS values are presented in the second row and their respective mapped

---

[3] Appendix **E** represents MATLAB codes for one of the subjects (S1).

length in the third row. The same $m_n$ and $M_n$ were used for the simulated results obtained with COMSOL since simulation results obtained with a dipole of few nA.m are in the µV range as for our experimental results.

Table 3.3: The ten experimental RMS values of a subject (S2) are assigned to a length varying from 1.2 for the smallest signal to 3.2 cm for the largest one (bolded green values). Those mapping factors are also applied to the COMSOL simulation results.

| Electrode # | 1 | 2 | 3 | 4 | 5 | 6 | 7 | 8 | 9 | 10 |
|---|---|---|---|---|---|---|---|---|---|---|
| RMS (µV) | 51 | 53 | 40 | 31 | 39 | 27 | 28 | 20 | 17 | 16 |
| Mapped length | 3.092 | 3.2 | 2.498 | 2.011 | 2.443 | 1.795 | 1.849 | 1.416 | 1.254 | 1.2 |
| COMSOL (µV) | 75.87 | 78.14 | 54.31 | 42.41 | 41.44 | 36.42 | 24.93 | 17.06 | 13.09 | 11.11 |
| Mapped value | 3.132 | 3.2 | 2.489 | 2.133 | 2.104 | 1.955 | 1.612 | 1.377 | 1.258 | 1.2 |

As it can be observed in Figure 3.10, experimental and simulation results were different for some of the recording sites. To quantify those differences, and eventually minimize them by assigning a different position for the dipoles, the following error function was used:

$$Error(\%) = \left( \frac{1}{10} \sqrt{\frac{\sum_{i=1}^{10}[\text{experimental}_i - \text{simulation}_i]^2}{\sum_{i=1}^{10}(\text{experimental}_i)^2}} \right) \times 100$$

where $experimental_i$ is the experimental RMS value of each signal and $simulatioon_i$ the result of the simulation.
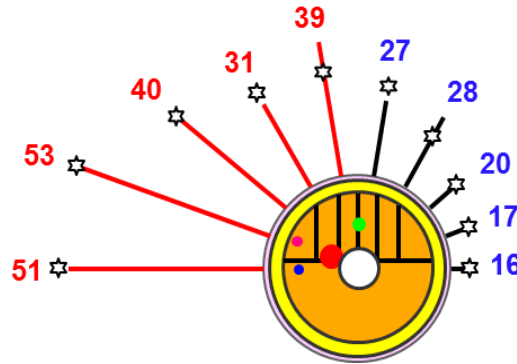


Figure 3.10: The 4-layer upper arm model around which the length of each spoke corresponds to the mapped length of the upper panel of Table 3.3. As for the stars, they correspond to the mapped values of the bottom panel of the same table obtained with a COMSOL simulation where 4 dipoles (colored dots) were considered (same subject's data as in Fig.3.2).

# CHAPTER 4   RESULTS

This chapter starts with results of two most accurate mesh resolutions in COMSOL. Verification results of FEM will be compared with two articles. In main section of this chapter, distribution of dipoles for all 10 subjects in different situations e.g. seated and standing up and with various hand postures will be presented.

## Mesh size

To choose between the 2 smallest pre-set COMSOL meshes, four variants of the 4-layer model were analyzed (Figure 4.1) in addition to the 1-layer model. In column A of that figure, each layer is given the same radius ratio (25%) relative to the radius of the outside cylinder (R). A somewhat more realistic repartition of the biological tissues in the upper arm is shown in column B where skin thickness was much reduced in favor of the fat and muscular tissues. In column C, the reduction of the fat layer is compensated by an increase of the muscular tissue and this variant is quite similar to the 1-layer model where only muscular tissue is present. The model shown in column D is the one we used for our simulations.

Differences between the 2 mesh sizes are generally small for each of the 10 simulated signals (Table 4.1) which is more easily observed in Figure 4.2. The extremely fine mesh resolution was used in all our simulations because, differences between each recording site was smaller than with the other mesh sizes and the simulation time was only 16 s longer (26 vs 10) . Even with the extremely fine mesh, and electrode sites placed on the same horizontal plane, there are still some signal differences (red curves) between each site within a model and between the models. Those small errors can be associated to the generation of the FEM which does not necessarily produce the same uniform mesh sizes everywhere as well as between the different models.
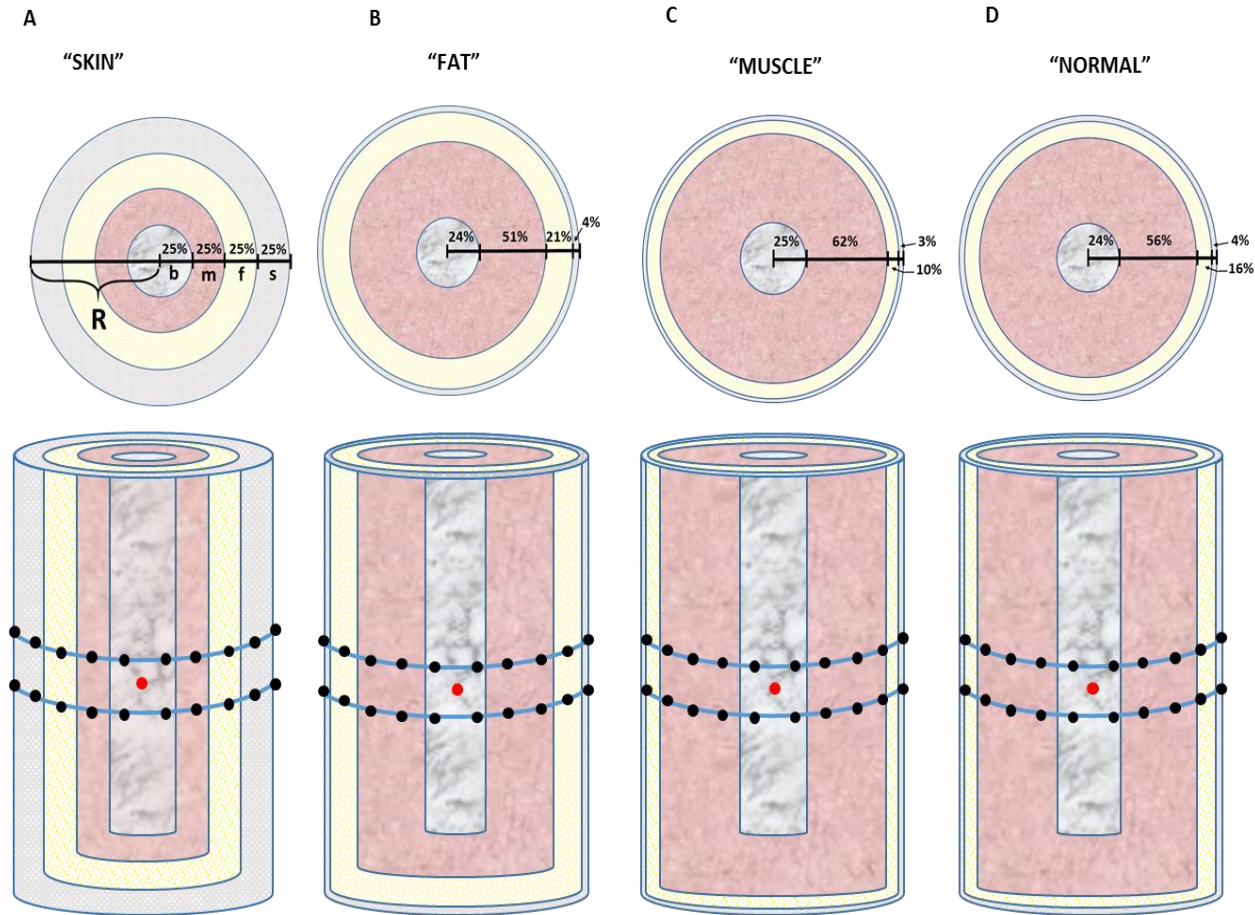
Figure 4.1: Variants of the 4-layer model used to model the upper arm. From outside to the inside, layers are   representing: the skin (s), the fat (f), the muscular tissue (m) and the humerus bone (b). **A:** each layer share the same radius (R) ratio i.e. 25%. f: fat, s: skin. **B:** skin thickness is reduced while fat and muscle volume are increased. **C:** situation where muscular volume is larger than the fat volume. **D:** model used in all simulations with our 10 subjects.

When average of those signals are displayed in Figure 4.3, it can be realized that with the 1-layer model, signal is smaller than for the 4-layer models due to the muscle higher conductivity relative to the other biological tissues, which results in smaller potentials reaching the electrodes. As muscle volume diminish, potentials at the electrode sites increases.

Table 4.1: The 10 differential simulated signals (µV) obtained when using extra Fine or Extremely Fine mesh for the 1-layer model and the 3 distributions of tissues examined with the 4-layer model. Average and standard deviation (±SD) are shown at the right.

| | | Electrode | 1 | 2 | 3 | 4 | 5 | 6 | 7 | 8 | 9 | 10 | Average | ±SD |
|---|---|---|---|---|---|---|---|---|---|---|---|---|---|---|
| 1-Layer | | Extra Fine | 205.31 | 205.39 | 205.35 | 205.17 | 204.95 | 204.83 | 204.85 | 204.93 | 205.15 | 205.35 | 205.13 | 0.22 |
| | | Extremely fine | 205.33 | 205.30 | 205.30 | 205.33 | 205.39 | 205.43 | 205.42 | 205.40 | 205.36 | 205.33 | 205.36 | 0.05 |
| 4-Layer | Type 1 "SKIN" | Extra Fine | 1033.74 | 1034.59 | 1035.61 | 1036.33 | 1036.22 | 1035.04 | 1033.88 | 1033.33 | 1032.97 | 1034.23 | 1034.59 | 1.18 |
| | | Extremely fine | 1036.48 | 1036.69 | 1036.86 | 1036.93 | 1036.95 | 1036.79 | 1036.48 | 1036.29 | 1036.29 | 1036.42 | 1036.62 | 0.26 |
| | Type 2 "FAT" | Extra Fine | 577.40 | 576.99 | 577.04 | 577.44 | 578.00 | 578.48 | 578.79 | 578.84 | 578.57 | 577.85 | 577.94 | 0.70 |
| | | Extremely fine | 577.09 | 577.03 | 576.92 | 576.81 | 576.79 | 576.87 | 577.01 | 577.17 | 577.25 | 577.24 | 577.02 | 0.17 |
| | Type 3 "MUSCLE" | Extra Fine | 336.97 | 336.66 | 336.70 | 337.00 | 337.37 | 337.69 | 337.91 | 337.95 | 337.73 | 337.27 | 337.33 | 0.48 |
| | | Extremely fine | 336.81 | 336.77 | 336.70 | 336.64 | 336.62 | 336.68 | 336.78 | 336.87 | 336.92 | 336.90 | 336.77 | 0.11 |
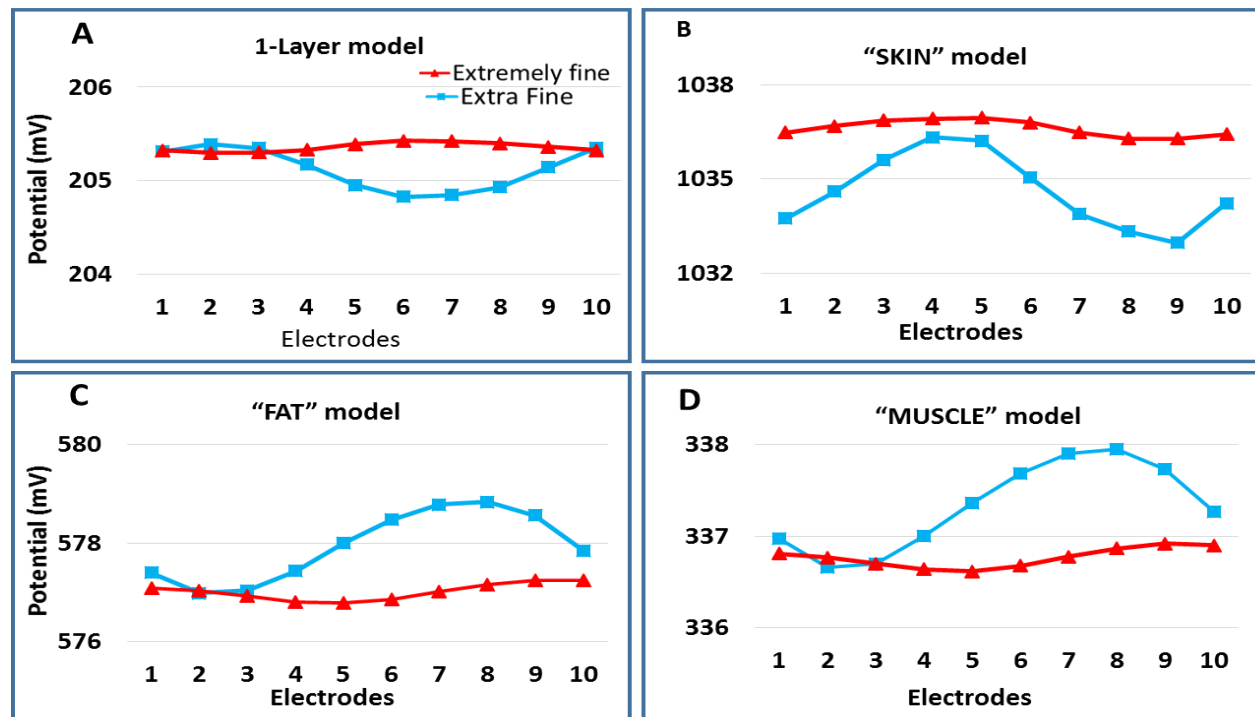


Figure 4.2: Extra and extremely fine mesh resolutions results at each electrode site for the 1-layer model (panel A) and for the three 4-layer models (panels B, C, D).
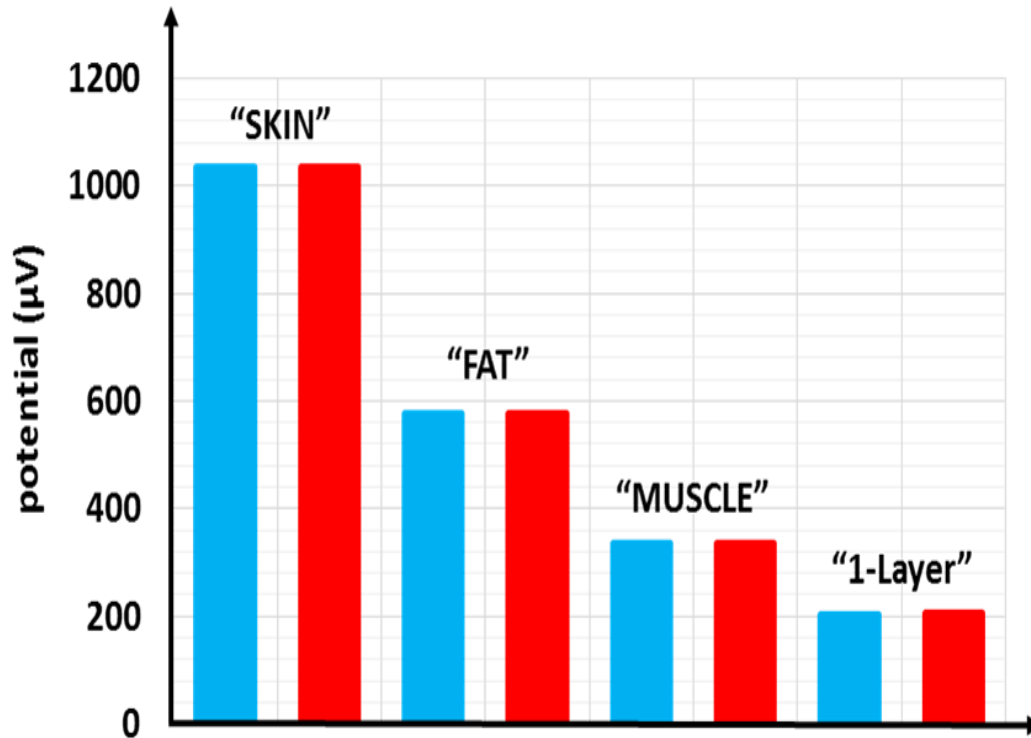
Figure 4.3: Mean results of the 10 electrode sites (from Table 4.1) obtained with extra fine (blue) and extremely fine mesh (red) resolutions in different 4-layer upper arm models and in the 1-layer one.

## Model validation

Before using our simulation model on our experimental results, we made 2 tests. One consisted in reproducing the results of Lambin and Troquet (1983) who modelled the human heart as an eccentric current dipole within an isotropic medium of a finite homogenous cylinder representing human's trunk. Orientation of the dipole was either 1) along the length of cylinder (Z_oriented), 2) perpendicular to the length of the cylinder and along the radius of the cylinder ($\rho$_oriented), 3) perpendicular to the both Z and $\rho$ directions and toward the angular axis ($\varphi$_oriented). The dipole position and dimension of trunk were the same as Okada (1956) but since Okada's analytical approach did not explain the potentials at the border of the cylinder, at sharp edges and it had some convergence problem, Lambin and Troquet (L&T) extended his work. We used the same parameters as their trunk cylindrical model which are: height: L=74.9 cm, radius: R=17.8 cm, radius position of the dipole: $\rho$'=4.93 cm and position of the dipole from the bottom of the cylinder:

z'=43.9 cm. Potentials on the model periphery were expressed in the arbitrary unit $\frac{P_z}{(\gamma L^2)}$ where $\gamma$ is the conductivity of the medium contained in the cylinder. Here are the comparisons for an eccentric z-oriented dipole as shown in Figure 4.4A. The L&T analytical results (their Figs 2 and 3) around the surface of the cylinder from its bottom to the top are shown in Figure 4.4B while our COMSOL simulations appear in C. When B and C are superposed, they fitted perfectly well as shown in D. For the same situation as in Figure 4.4A, equipotential lines obtained with the analytical model were similar to ours simulated results as displayed in Figure 4.5.
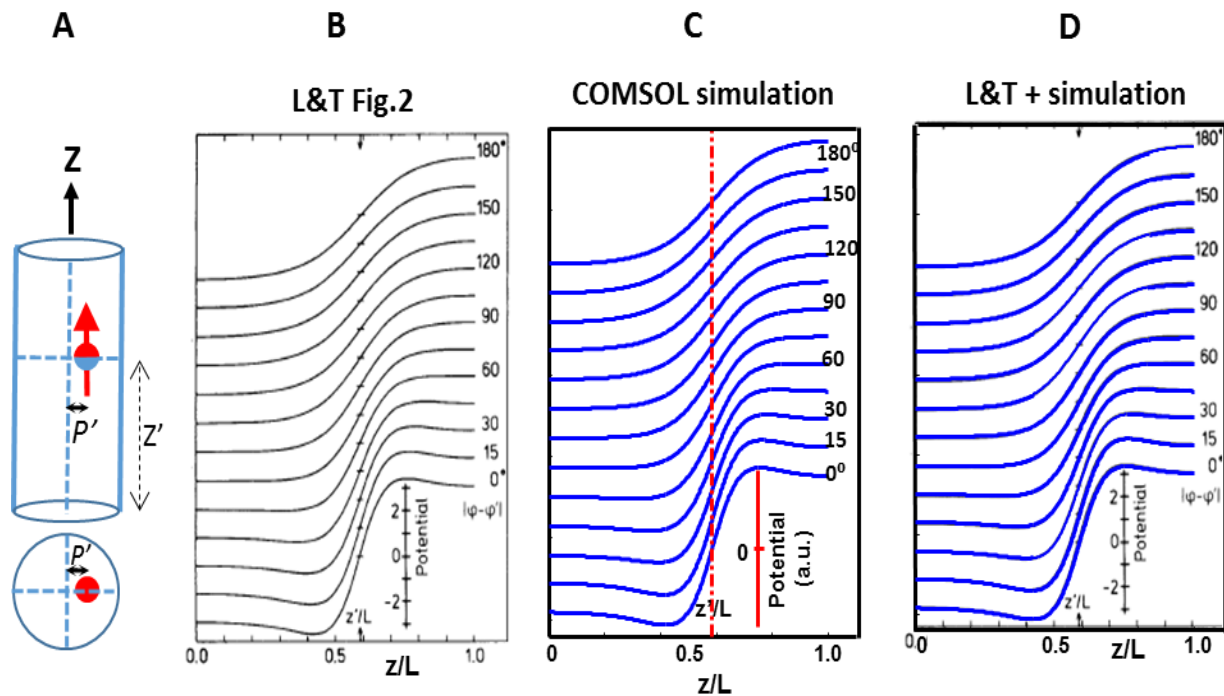


Figure 4.4: **A:** Human trunk modelled as a cylinder of radius (R) of 17.8 cm and a length (L) of 74.9 cm within which an eccentric z-oriented dipole is positioned ($\rho'$/R =0.277 and z'/L= 0.586). **B:** L&T analytical results obtained around half (0° to 180°) of the cylinder at various z'/L levels of the dipole. **C:** our COMSOL simulation results obtained in the same conditions. **D:** Superposition of our simulated results with the L&T analytical results.
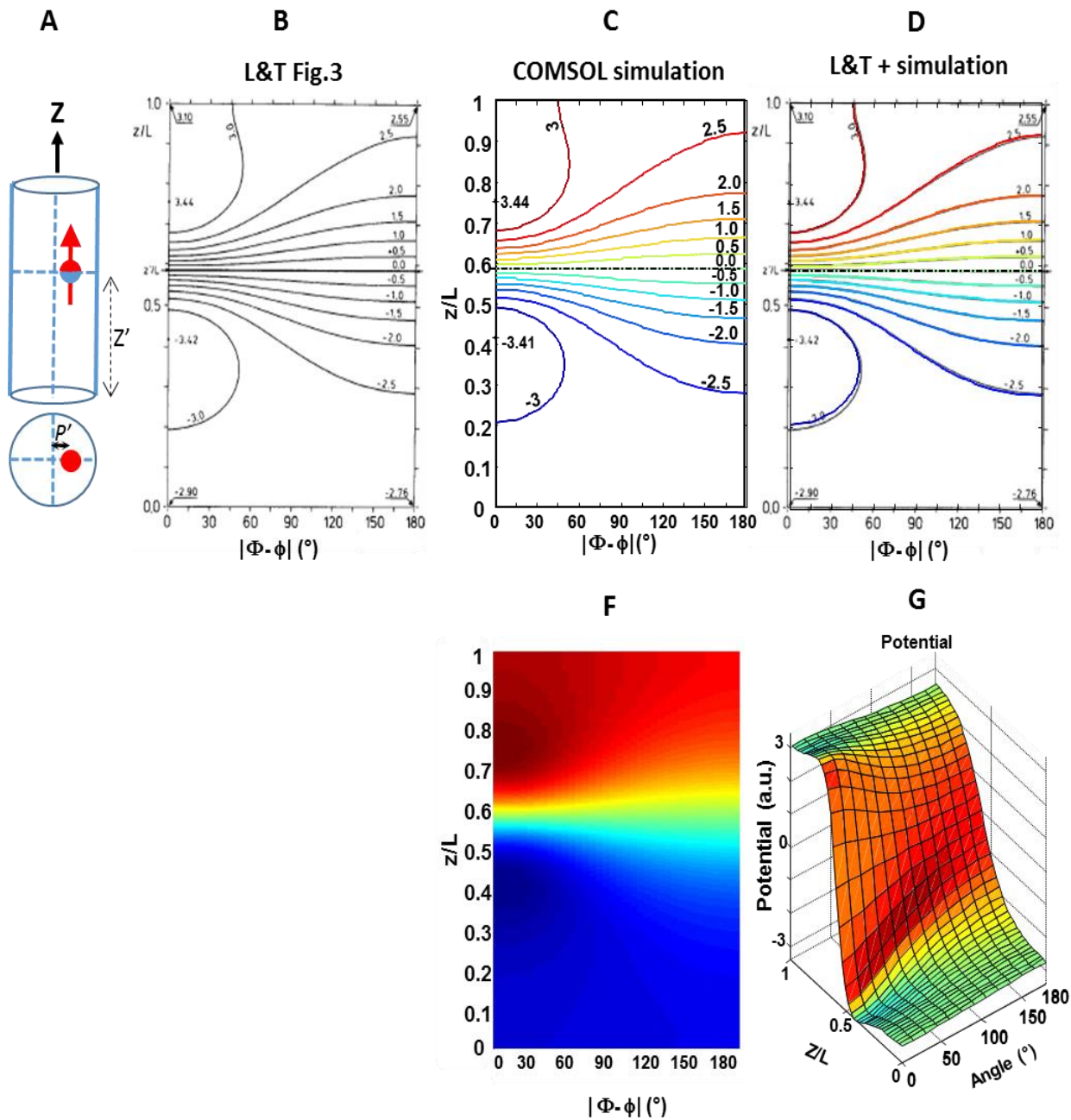
Figure 4.5: **A:** Same situation as in **A** of the previous figure. **B:** L&T analytical equipotentials obtained around half of the cylinder at various z'/L levels of the dipole. **C:** Our simulation results obtained in the same conditions. **D:** Superposition of simulation and analytical results. **E:** 2D view of C. **F:** 3D representation of the simulated results where potential amplitude is expressed in arbitrary units (a.u.).

Comparison between the L&T results and ours simulations for a $\rho$- and a $\varphi$-oriented dipole (their Figs 6 and 5) are shown in Figure 4.6 and Figure 4.7 respectively. As it can be observed, in both situations, our simulations results are quite close to their equipotentials.
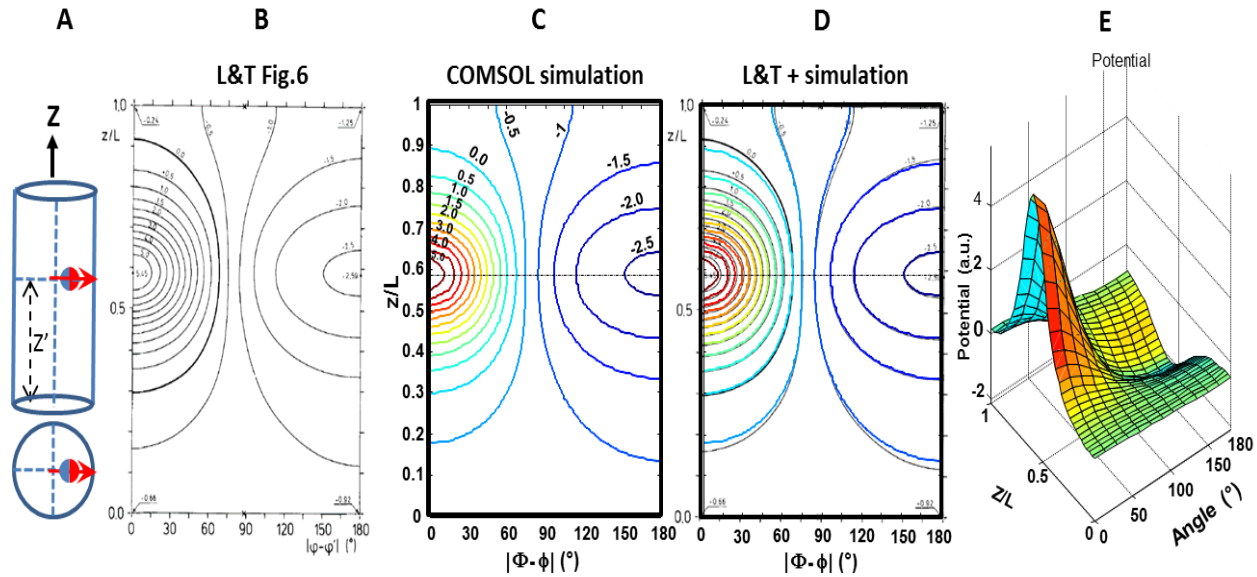


Figure 4.6: **A:** Trunk model as in Fig.4.4.A. Except that the dipole is ρ-oriented. **B:** L&T analytical results obtained around half (0° to 180°) of the cylinder at various z'/L levels of the dipole. **C:** Simulation results obtained in the same conditions. **D:** Superposition of B and C. E: 3D representation of the simulated results where potential is expressed in arbitrary units (a.u.).
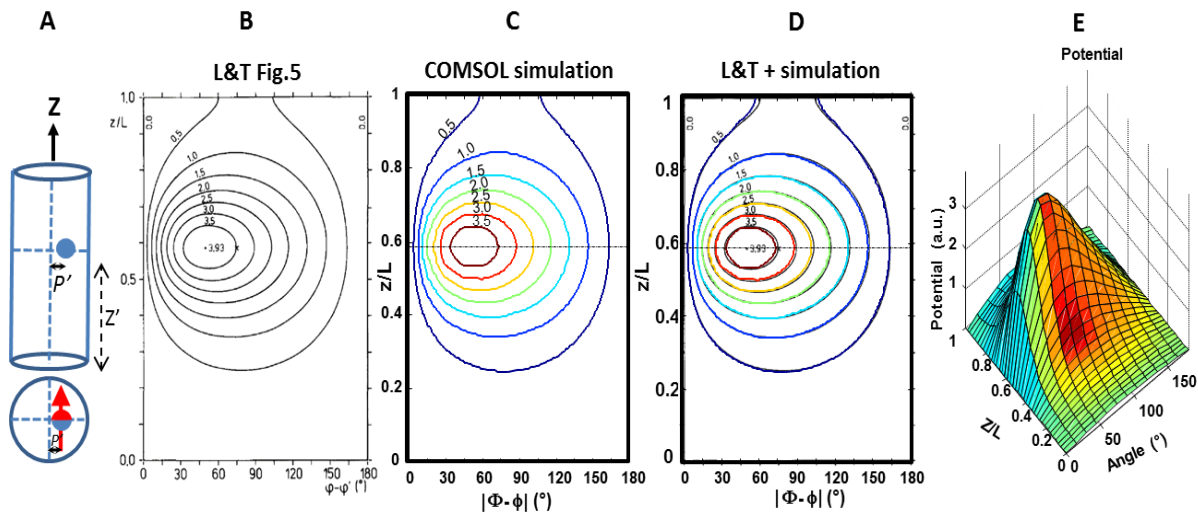


Figure 4.7: **A:** Same situation as in Fig 4.4.A. except that the dipole is φ-oriented **B:** L&T analytical results obtained around half (0° to 180°) of the cylinder at various z'/L levels of the dipole. **C:** Simulation results obtained in the same conditions. **D:** Superposition of B and C. **E:** 3D representation of the simulated results. Where potential amplitude is expressed in arbitrary units (a.u.).

For our second validation test, we choose the Saitou et al. [34] article where the image method was used to identify the depth and intensity of dipoles that could be associated to experimental potentials recorded across the bicep of 3 subjects with an array of 16 pairs of electrodes (see p.21) of Chapter 2). In our simulations to reproduce their Figs 5 and 7 results, we used a 1-layer cylinder model (diameter: 6.2 cm, height: 16 cm) filled with isotropic muscular tissue within which their dipoles were inserted. As in their experimental protocol, 16 pairs of electrodes separated by a vertical distance of 5 mm and with a horizontal center-to-center distance of 2.5 mm were placed around the cylinder.

At the top left of our Figure 4.8, a 3D surface plot of their Fig.5 simulated signals is shown. It consists of 16 differential signals of 12 s long while their contour plot is presented in the bottom panel where the location of the 5 dipoles at the origin of those results have been added. In our simulations, the 5 dipoles have to travel a distance along our model corresponding to the 12 ms of Figure 4.8A. Considering that the conduction velocity of an action potential in a muscular fiber is 4 m/s, the distance travelled in a 12 ms time span is 48 mm. In Figure 4.9 which is a partial enlargement of Figure 4.8B, the position of each dipole along the time axis ($D_{p1}$, $D_{p2}$, $D_{p3}$, $D_{p4}$, $D_{p5}$) was determined and the delays between them converted to distances: i.e. 0.52 mm between $D_{p1}$ and $D_{p2}$, 0.68 mm between $D_{p2}$ and $D_{p3}$ and 0.40 mm between $D_{p3}$ and $D_{p4}$ as well as for $D_{p4}$ and $D_{p5}$. Our simulation results (Figure 4.8B and D) were obtained with those dipoles characteristics and the temporal delays between them.

The results of their Fig.7 are shown in our Figure 4.10 where the surface plot A is slightly more complex than in their Fig. 5. Here, such a result was associated to 6 spread dipoles as can be seen on its contour plot in C. As can be seen in B and D, our simulation results are lacking similarity with their results.

We were unable to satisfactorily duplicate the Saitou et al. results partly because no amplitude scale was ever provided for their surface plot and no potential values was associated to their equipotential contours: various intensities of the dipoles were experimented but no fruitful combination was found.
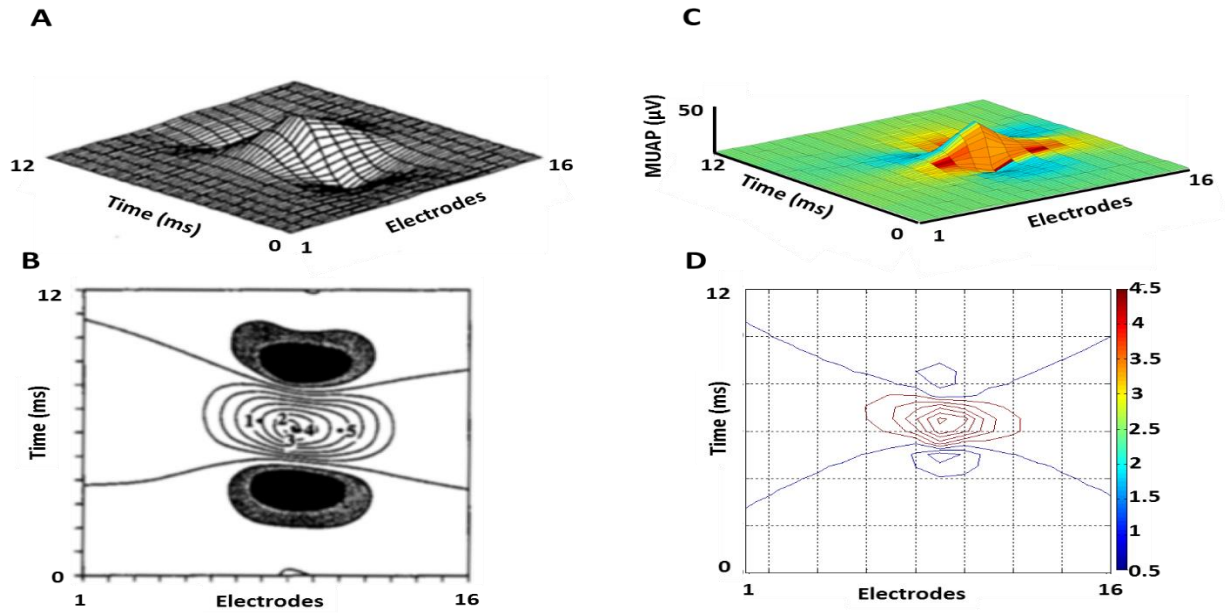
Figure 4.8: On the left, simulated results of Fig. 5 of Saitou et al. which duplicate an experimental result and on the right our simulation results. Surface potential distribution are shown in A and C while their corresponding contour plots are displayed in B and D. Position of the 5 dipoles at the origin of those results are shown in B. Dipole depth position and intensity are: dipole 1: 3.8 mm and 0.9 nAm; dipole 2: 4.0 mm and 3.3 nAm; dipole 3: 2.4 mm and 2.5 nAm; dipole 4: 1.7 mm and 0.7 nAm; dipole 5: 3.0 mm and 0. 4 nAm.
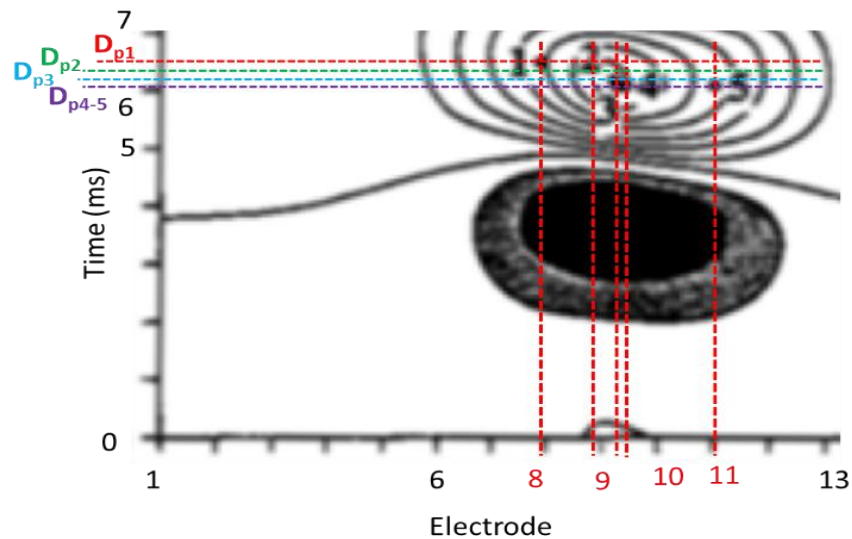


Figure 4.9: Estimation of dipoles positions in time-channel (electrode) based on an enlarge portion of Saitou et al. Fig.5.

Dipoles were moved around without producing clearly detectable improvement in the results. In addition, some of their dipole depths were so small as to put them in the skin and fat layers which is impossible. Considering that Saitou et al. model produced non-realistic dipole locations and amplitude scale lacking in their results display, duplication of their simulations is near impossible to achieve.
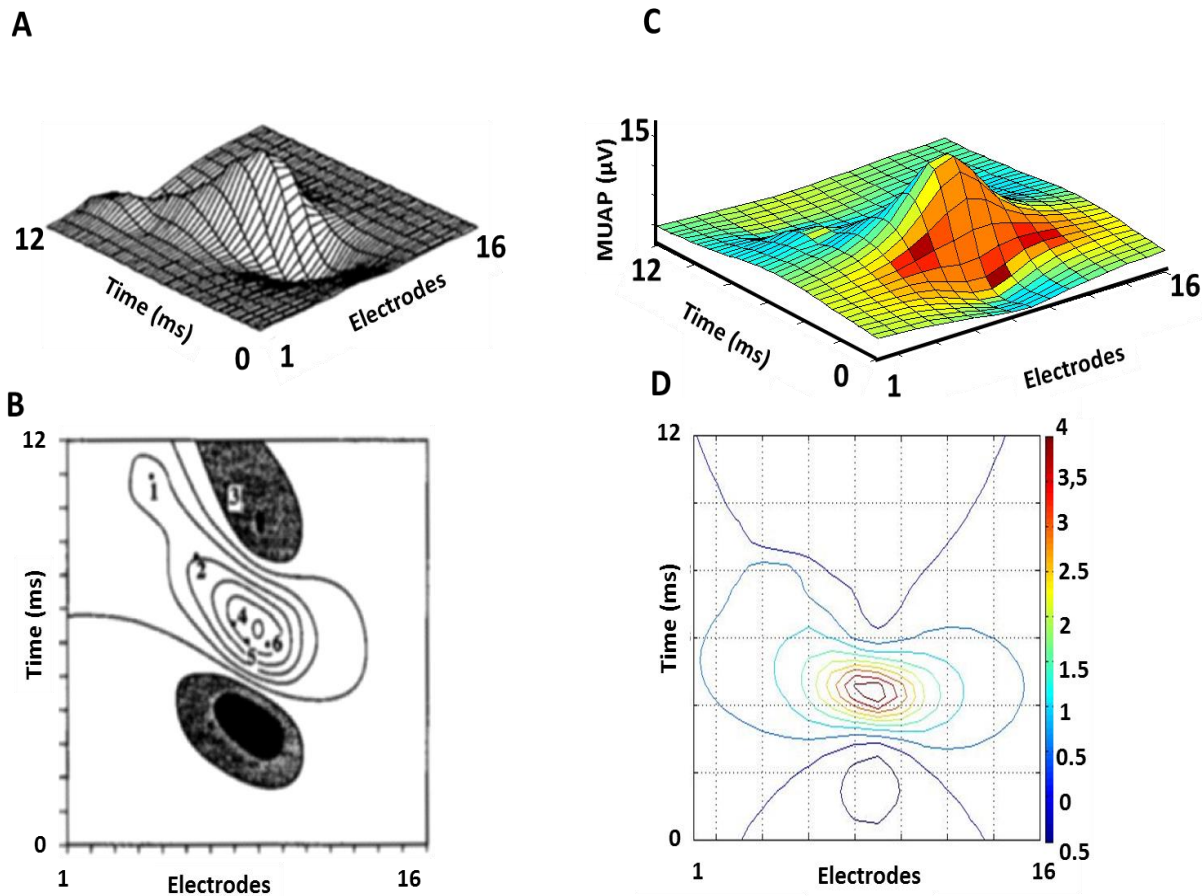


Figure 4.10: Same display as in the Figure 4.8. Dipole depth position and intensity are: dipole 1: 2.2 mm, 0.1 nAm; dipole 2: 5.7 mm, 0.8 nAm; dipole 3: 6.2 mm, 0.6 nAm; dipole 4: 3.7 mm, 0.6 nAm; dipole 5: 6.6 mm, 2.6 nAm; dipole 6: 3.7 mm, 0.8 nAm. **A:** Saitou 3D view of the simulated results. **B:** Saitou top view with location of the six dipoles (1-6) **C** and D: Our simulation results (A and B from Saitou et al. Fig.7).

So, considering the very satisfactory duplication of the results of L&T, a good confidence can be put in our COMSOL models ability to provide valuable information on the best dipole locations that were at the origin of the experimental EMG signals that have been recorded across the biceps of 10 normal subjects.

## Dipoles results with the 1-layer model.

In our 1-layer upper arm model, only isotropic muscular tissue is present. The dipoles identified with the peak fitting method in the seating position were initially positioned in the column A at the left of Figure 4.11and those identified in the standing-up position in the column A at the right. Since the simulation results (magenta bullets) were different from some of the 10 experimental signals (red and black spokes), positions of the dipoles were manually changed, and by successive essays, more satisfying results (smaller error values) were obtained as can be seen in columns B.
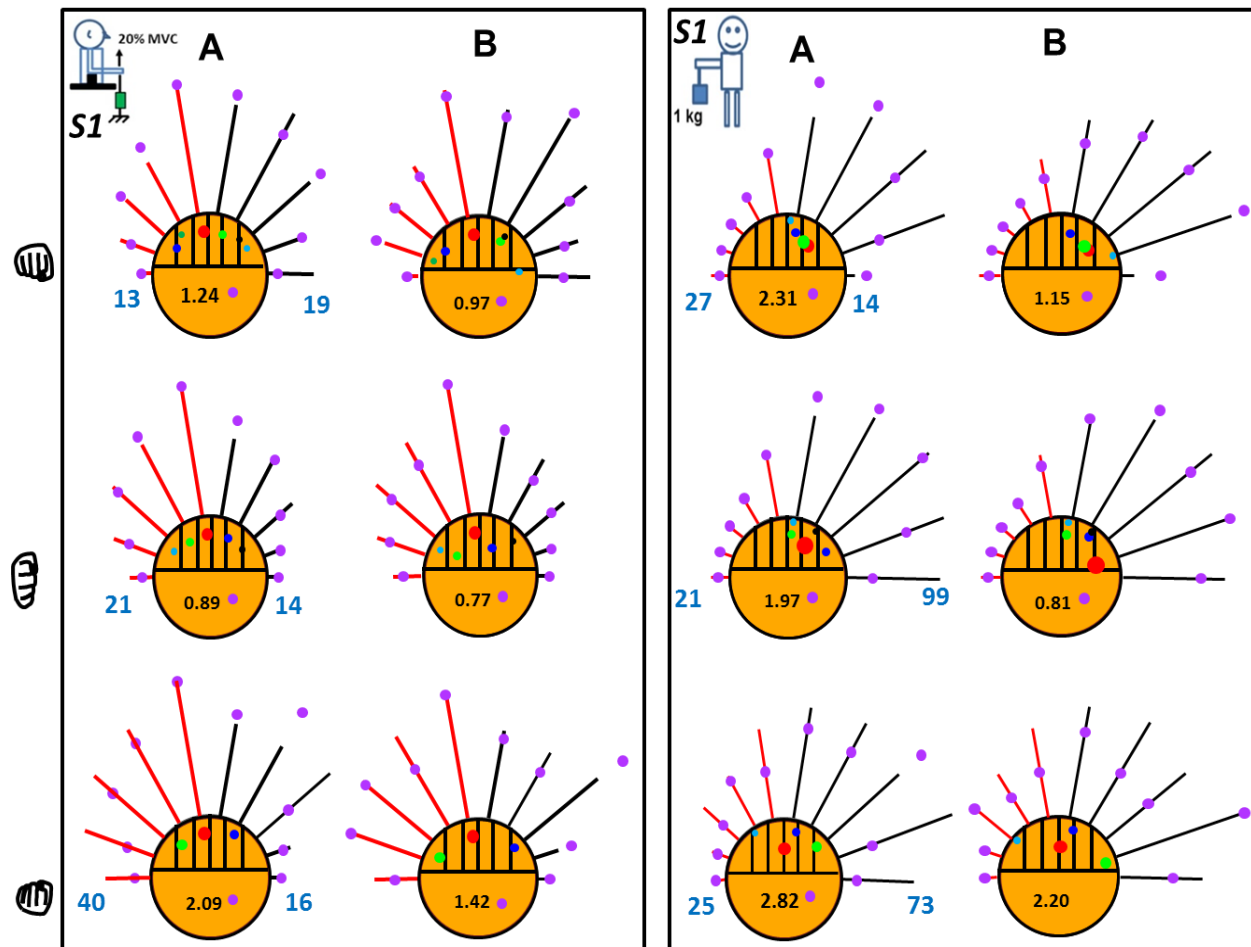


Figure 4.11: Experimental data (spokes length proportional to the RMS value (µV) with superposed simulation results for S1 in the seated and standing up positions while the hand was pronated, in neutral position or supinated. Columns A: initial estimation of dipoles' characteristics as obtained with the peak fitting method. Columns B: the dipole positions were changed manually to get a better match with the RMS values of the experimental data (spokes length proportional to the RMS value (µV)). Improvements is detected by the smaller number appearing within each circle in B columns as compared to A columns. Those numbers are measurements of the differences between experimental data and simulation results (equation p.47).

## Dipoles results with 4-layer models

For a more realistic model, the upper arm was considered as being made of 4 concentric layers representing the skin, the fat layer, the muscular tissue and the humerus bone as shown in Figure 4.1. All our following results were obtained with the 4-layer model where the thickness of each layer is as shown in Figure 4.1D. While all layers were initially considered isotropic, an anisotropy factor of 5 was later introduced for the muscular tissue.

As can be seen in Figure 4.12A, some of the dipoles obtained with the B column of previous figure (Figure 4.11) were located in fat and skin tissues. So those dipoles where moved in the muscular tissue and position of the other dipoles were also modified to get a better match with the experimental results (column B). In column C, the position of the dipoles is the same as in column A but the muscular tissue is now anisotropic; the error is larger than in A but was reduced appreciably by moving the dipoles as shown in column D. Results of another subject are shown in Figure 4.13 before and after manual optimization of the dipole positions for isotropic and anisotropic muscular tissue. Results similar to those of S1 and S6 were obtained for the 8 other subjects.
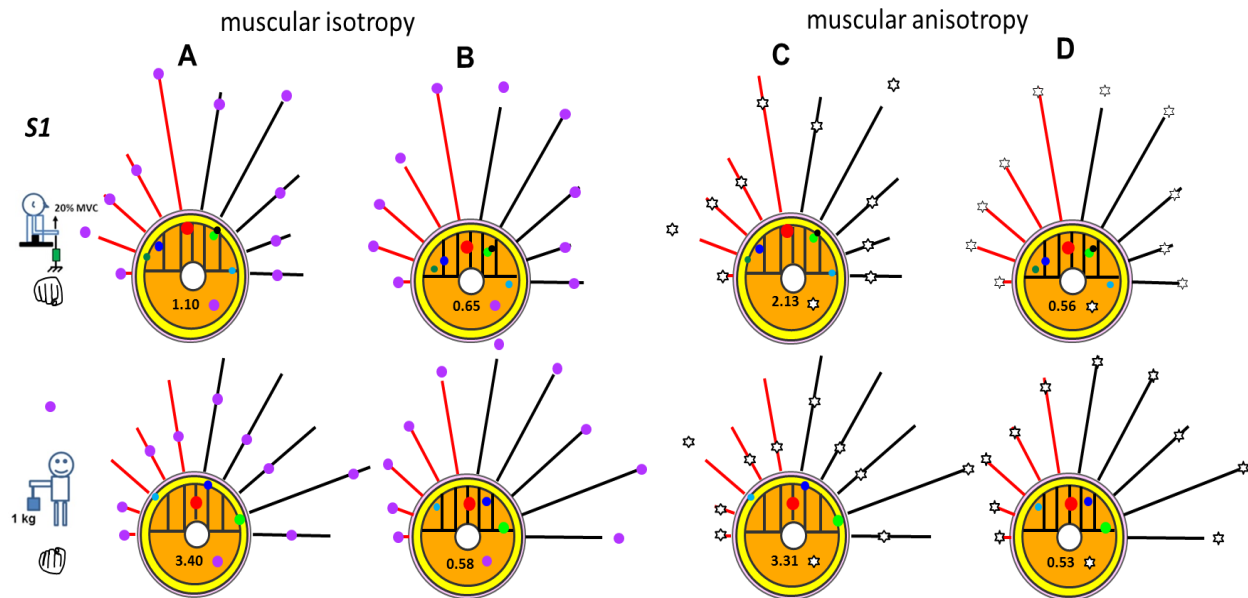


Figure 4.12: Column A: The dipole positions for the 1-layer model showed in Fig. 4.11.B were used in a 4-layer model were muscle tissue was isotropic. Column B: Dipole positions of column A were moved to get a better match between experimental data and simulation results. Column C: Same dipole positions as in A but muscle tissue is anisotropic. Column D: Same dipole positions as in B but for anisotropic muscle tissue condition.
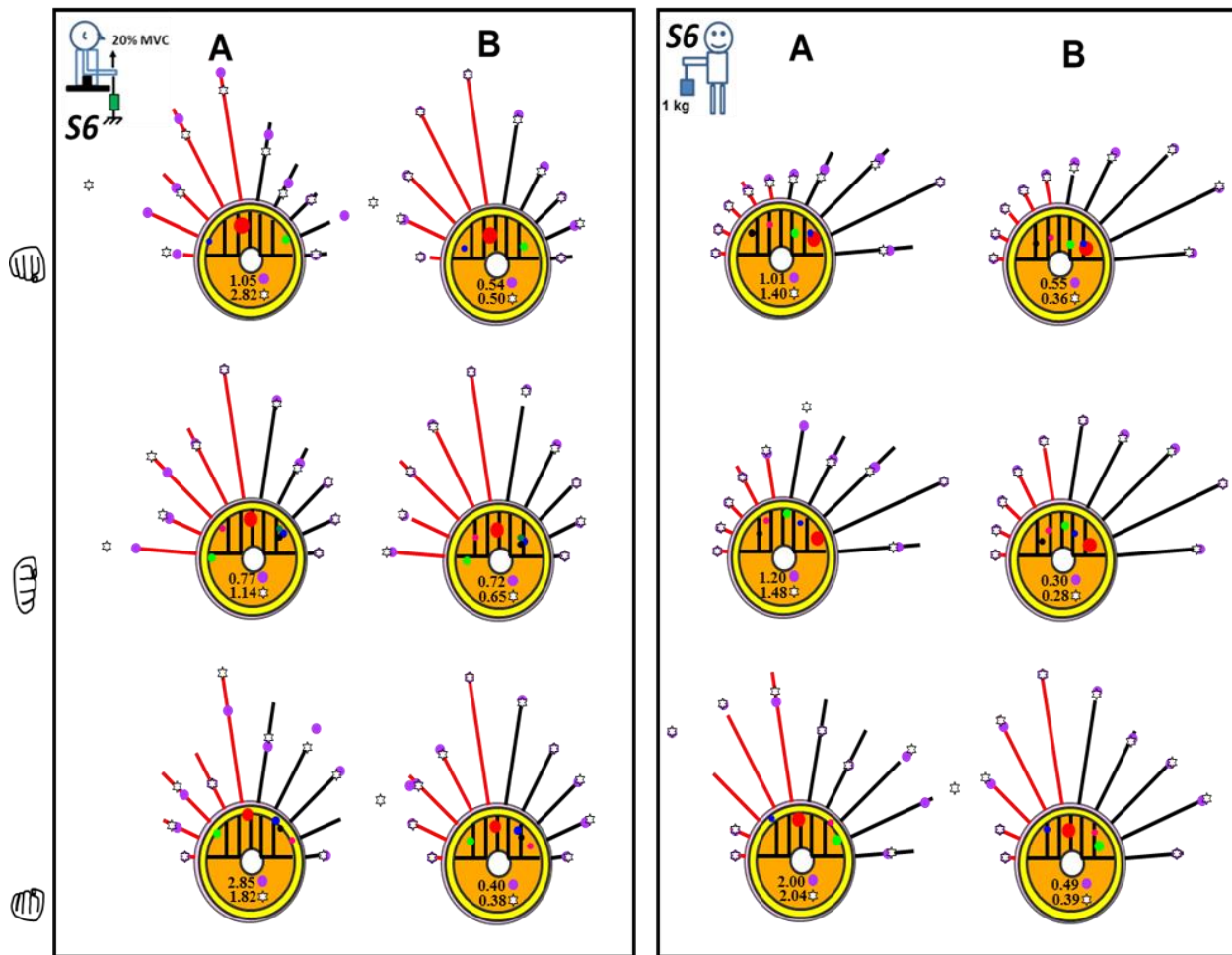
Figure 4.13: Results of S6 without (magenta bullets) and with muscular anisotropy condition (stars). Columns A: results obtained with modified dipole positions obtained from the 1-layer model. Columns B: a better match is obtained following changes in the dipoles position.

To select the most appropriate arm model for duplicating the experimental data, errors measuring differences between experimental and simulation results were used. In the two panels of Table 4.2, the results obtained by each subject indicate that the error is appreciably reduced when the 1-layer is replaced by the 4-layer isotropic model while further error reduction is only minimal when muscular anisotropy is introduced. This is graphically presented in Figure 4.14 where the error obtained with the 3 models are shown for each subject while mean values of the group are presented in Figure 4.15.

Table 4.2: For each subject, errors % between experimental and simulated results in different hand postures in the seated position (panel A) and in the standing up position (panel B) for 3 different upper arm model. Mean and standard error (±SE) for each model is also shown.

**A**

| 20% MVC | Pronation | | | Neutral | | | Supination | | |
|---|---|---|---|---|---|---|---|---|---|
| | 1-layer | 4-layer | | 1-layer | 4-layer | | 1-layer | 4-layer | |
| | Isotropy | Isotropy | Anisotropy | Isotropy | Isotropy | Anisotropy | Isotropy | Isotropy | Anisotropy |
| S1 | 1.24 | 0.65 | 0.56 | 0.89 | 0.72 | 0.68 | 2.09 | 0.69 | 0.68 |
| S2 | 2.68 | 0.89 | 0.68 | 2.79 | 1.1 | 0.93 | 2.79 | 0.89 | 0.63 |
| S3 | 1.30 | 0.54 | 0.42 | 1.50 | 0.83 | 0.69 | 1.72 | 0.53 | 0.52 |
| S4 | 2.94 | 1.04 | 0.80 | 2.5 | 0.7 | 0.43 | 2.06 | 0.6 | 0.53 |
| S5 | 2.09 | 0.52 | 0.49 | 2.03 | 0.51 | 0.49 | 1.82 | 0.68 | 0.43 |
| S6 | 1.32 | 0.54 | 0.50 | 2.02 | 0.72 | 0.65 | 1.41 | 0.40 | 0.38 |
| S7 | 2.82 | 0.73 | 0.41 | 1.38 | 0.55 | 0.49 | 1.23 | 0.71 | 0.61 |
| S8 | 1.94 | 0.47 | 0.45 | 1.42 | 0.72 | 0.41 | 2.44 | 0.85 | 0.65 |
| S9 | 1.39 | 0.58 | 0.33 | 1.33 | 0.51 | 0.49 | 1.24 | 0.36 | 0.31 |
| S10 | 2.43 | 1.04 | 0.82 | 1.70 | 1.09 | 0.58 | 1.43 | 0.87 | 0.80 |
| | | | | | | | | | |
| mean | 2.02 | 0.70 | 0.55 | 1.76 | 0.75 | 0.58 | 1.82 | 0.66 | 0.55 |
| ± SE | 0.68 | 0.22 | 0.17 | 0.58 | 0.21 | 0.16 | 0.52 | 0.19 | 0.15 |

**B**

| 1 kg | Pronation | | | Neutral | | | Supination | | |
|---|---|---|---|---|---|---|---|---|---|
| | 1-layer | 4-layer | | 1-layer | 4-layer | | 1-layer | 4-layer | |
| | Isotropy | Isotropy | Anisotropy | Isotropy | Isotropy | Anisotropy | Isotropy | Isotropy | Anisotropy |
| S1 | 2.31 | 1.17 | 1.02 | 1.97 | 0.57 | 0.49 | 2.82 | 0.58 | 0.53 |
| S2 | 1.73 | 0.63 | 0.61 | 1.23 | 0.58 | 0.46 | 1.46 | 0.78 | 0.78 |
| S3 | 1.84 | 0.36 | 0.32 | 1.57 | 0.57 | 0.45 | 1.65 | 0.77 | 0.67 |
| S4 | 2.37 | 0.48 | 0.46 | 3.4 | 0.48 | 0.43 | 2.54 | 0.72 | 0.7 |
| S5 | 3.11 | 0.52 | 0.51 | 2.9 | 0.37 | 0.32 | 3.39 | 0.45 | 0.37 |
| S6 | 2.42 | 0.55 | 0.36 | 2.37 | 0.30 | 0.28 | 1.88 | 0.49 | 0.39 |
| S7 | 2 | 0.65 | 0.57 | 1.98 | 0.71 | 0.53 | 2.25 | 0.71 | 0.7 |
| S8 | 3.26 | 0.50 | 0.28 | 2.96 | 0.76 | 0.55 | 1.64 | 0.40 | 0.38 |
| S9 | 1.55 | 0.42 | 0.25 | 2.20 | 0.56 | 0.44 | 1.46 | 0.66 | 0.40 |
| S10 | 2.87 | 0.44 | 0.16 | 2.80 | 1.35 | 0.62 | 2.65 | 0.92 | 0.32 |
| | | | | | | | | | |
| mean | 2.35 | 0.57 | 0.45 | 2.34 | 0.63 | 0.46 | 2.17 | 0.65 | 0.52 |
| ± SE | 0.59 | 0.23 | 0.25 | 0.68 | 0.29 | 0.10 | 0.66 | 0.17 | 0.17 |
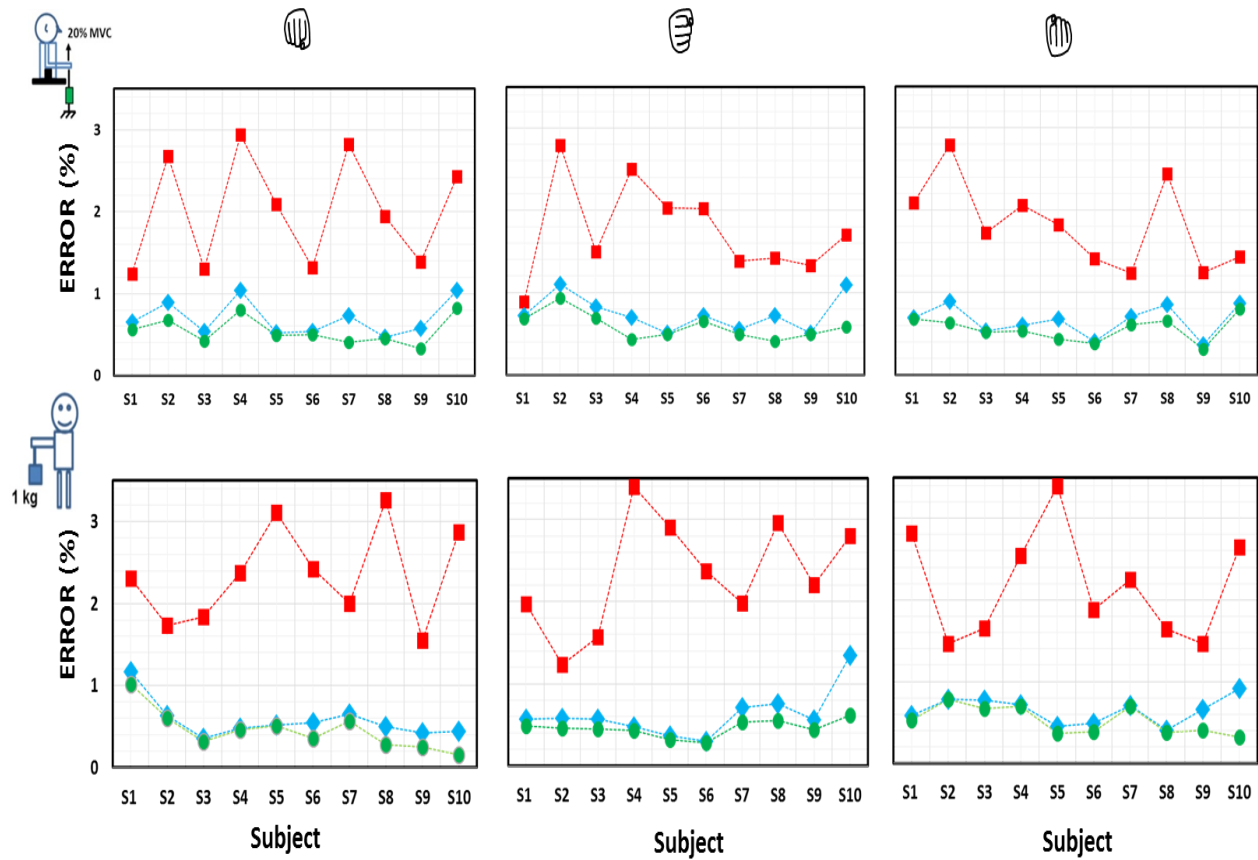
Figure 4.14: Graphical representation of the errors of each subject shown in Table 4.2 with the 3 arm models used: red: 1-layer model, blue: 4-layer isotropic muscle tissue, green: 4-layer anisotropic muscle layer.
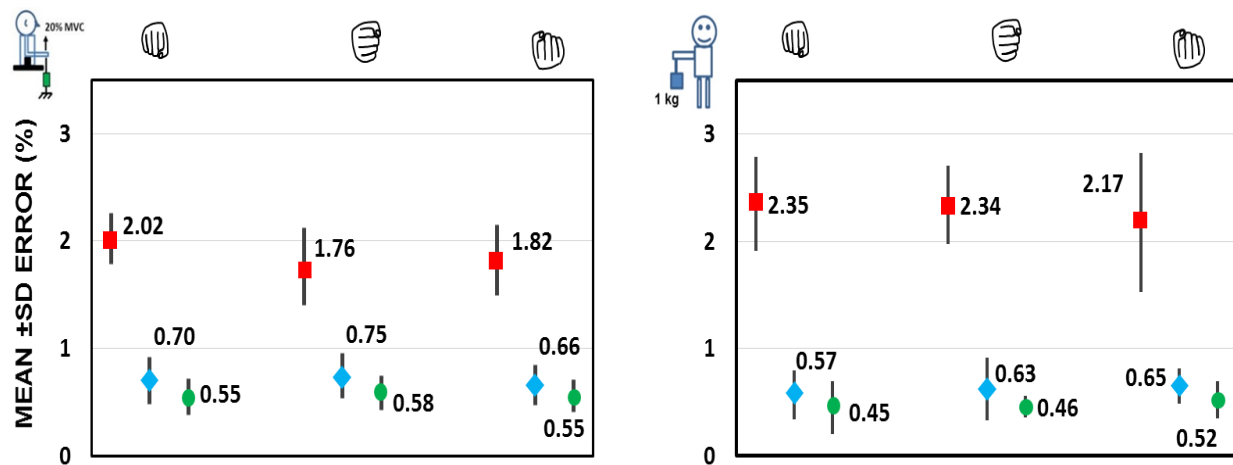


Figure 4.15: Mean (±SE) obtained for the 10 subjects with three upper arm models red: 1-layer blue: 4-layer and isotropic muscle, green: 4-layer and anisotropic muscle tissue.

## Dipoles repartition with 4-layer models

As the 4-layer anisotropic model provided the best estimate of the dipoles position, the location of the dipoles within each head of the biceps was analyzed. Based on our simplified representation of the biceps (Figure 3.2, p.43) and as shown in Table 4.3, a roughly equivalent number of dipoles (69 and 57) were found in each head when the subjects were seated while a great difference (42 vs 77) was observed in the standing-up position due to a greater presence of the dipoles in the LH. In those results, hand position does not appear as important.

Table 4.3: For the 10 subjects, total number of dipoles found within each head and outside of the biceps obtained with the 4-layer anisotropic model upper arm model.

| 20% MVC | SHORT HEAD | LONG HEAD | OUTSIDE OF THE BB | TOTAL |
|---|---|---|---|---|
| Pronation | 24 | 17 | 5 | 46 |
| Neutral | 22 | 22 | 4 | 48 |
| Supination | 23 | 18 | 4 | 45 |
| TOTAL | 69 | 57 | 13 | 139 |

| 1 kg | SHORT HEAD | LONG HEAD | OUTSIDE OF THE BB | TOTAL |
|---|---|---|---|---|
| Pronation | 12 | 26 | 3 | 41 |
| Neutral | 17 | 27 | 3 | 47 |
| Supination | 13 | 24 | 3 | 40 |
| TOTAL | 42 | 77 | 9 | 128 |

In the seated and standing up position, 22 dipoles were found outside of the assumed boundary of the BB and their relative intensity was usually small except in one occasion as shown in Figure 4.16. For the dipole with a relative intensity above 0.60, it seems that an important portion of the EMG signal recorded by few pairs of electrodes above the biceps would have been come from a neighbor muscle such as the brachialis. For the other 21 situations, the position of the dipoles outside the biceps can be associated to a less important crosstalk originating from the brachialis and coracobrachialis muscles.
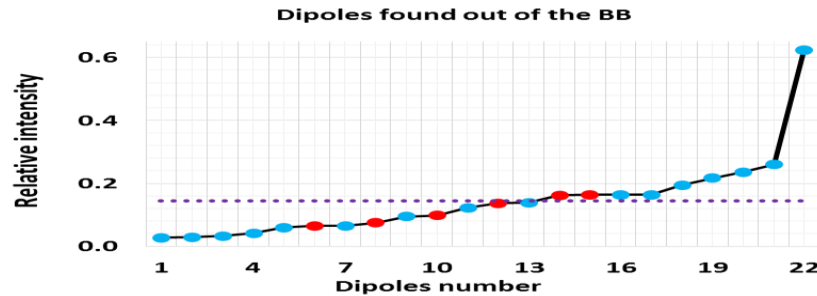
Figure 4.16: Relative intensity of the dipoles located outside the biceps model. Red dots represent dipoles located below the SH (near the 1st compartment) and blue ones under the LH (near the 6th compartment. The dashed line represents the average of all 22 dipoles.

As for the relative intensity of the dipoles, attention was given to values of the 2 most important dipoles which are displayed in Figure 4.17. Among 60 situations (10 subjects x 2 body positions x 3 hand postures), the relative intensities of the most important dipole ranged between 0.37 and 0.89 while the second most important ranged between 0.06 and 0.42.
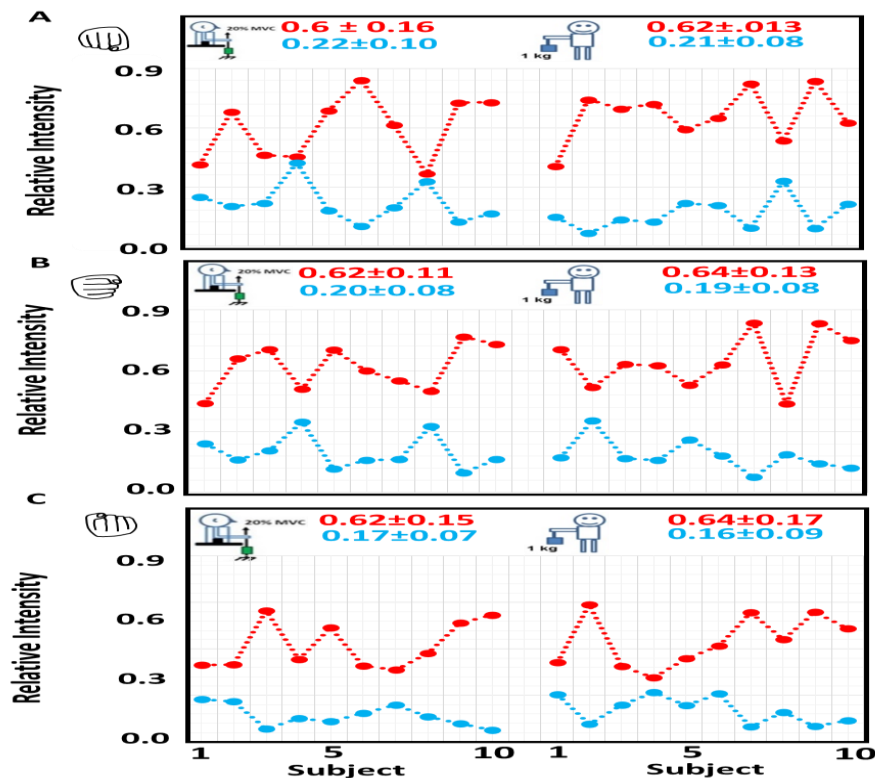


Figure 4.17: Relative intensity of the most important dipoles (red) and the second most important ones (blue). **A:** Pronation **B:** Neutral **C:** Supination. Mean (±SE) values for those dipoles are shown at the top of each panel.

Position of those 2 most important dipoles within the assumed compartments of the biceps are shown in Figure 4.18. In the seated position with the hand pronated, the largest dipole was most of the time located in compartments #2 to #4 but never in #1. With the hand in neutral position, the largest dipole was never located in compartments #5 and #6 while in supination the most important dipole was never located in compartments #1, #5, #6. In the standing up position, for pronation and neutral position, the largest dipoles were never located in compartments #1 to #3 and for supination, it never was in #1, #2 and #6. As for the second most important dipoles, in the seated position they never appeared in #1, #3 or #4 depending in the hand posture. In the standing up position with the hand pronated they were all located in the #5 and #6 compartments. In neutral position, they were absent in #3 and #5 compartments and most often present in the #6. In supination, dipoles were most frequently located in compartments #3 and #6. While the most important dipole was found only once outside that biceps, this happened 10 times for the second most important dipole and 11 times for the other dipoles with a smaller relative intensity.
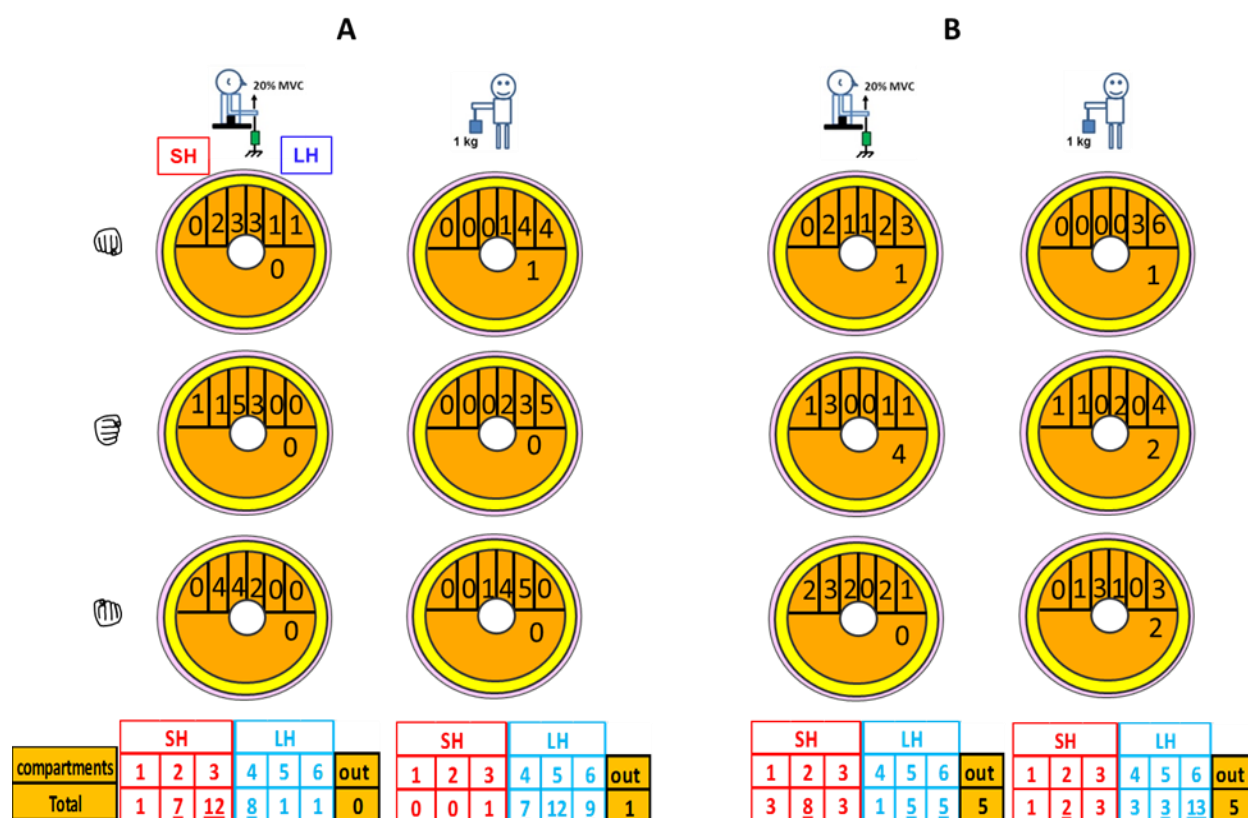


Figure 4.18: For the 10 subjects, number of occasions where the dipole with the highest relative intensity (A panel) and the second most important one (B panel) were found in a given compartment of the biceps.

Subject by subject information on the dipole distribution within the biceps compartments is shown in Table 4.4. For the dipoles located within the biceps compartments, it can be observed in the seated position that more dipoles are located in the SH (compartments #1, #2, #3) than in the LH compartments #4 and #5 but not for the #6. As for the standing up position, there are 2 times more dipoles in the LH than in the SH. As for the dipoles located outside of the modelled biceps, in the seated position they are found near compartment #1 and #6 while in the standing up position, they are most frequent in compartment #6. While such dipoles were absent from S4, S6 and S8 data, they were found 9 times for S10.So far, we cannot explain why it occurred so often for S10 but are investigating why.

A detailed illustration of the dipoles distribution of the 10 subjects within the assumed compartments of the BB is presented in Figure 4.19. Dipoles were found to be present in each assumed compartments but not uniformly. In the seated position and hand pronated for instance, 9 dipoles were found in the 3$^{rd}$ and the 6$^{th}$ compartment while with the hand in neutral position, 11 dipoles were positioned within the 2$^{nd}$ and 6$^{th}$ compartments and in supination, 9 dipoles were found in the 3$^{rd}$ compartment. In the standing up position, a greater number of dipoles were located in the 5$^{th}$ or the 6$^{th}$ compartment depending on the hand position. As mentioned previously, some dipoles were located outside the biceps.

Table 4.4: For the 4-layer anisotropic model, comparison of distribution of dipoles within compartments of the biceps in seated and standing up positions for the 3 hand postures. Each black "**x**" represents a dipole within a given compartment and a red "**x**" a dipole found outside the biceps but near the compartment where it is displayed. Absence of "x" indicates that no dipole was located in that compartment. At the bottom of the table Σx corresponds the total number of dipoles in each compartments and Σx to the number of dipoles found outside the biceps but near a given compartment.

| | | Seated | | | | | | Standing Up | | | | | |
|---|---|---|---|---|---|---|---|---|---|---|---|---|---|
| | | Compartments | | | | | | Compartments | | | | | |
| | | 1 | 2 | 3 | 4 | 5 | 6 | 1 | 2 | 3 | 4 | 5 | 6 |
| **Pro** | S1 | x | x | x | | xx | **x** | | | | x | xx | x |
| | S2 | x**x** | x | | x | | | | | | x | x | x |
| | S3 | x | x | xx | | x | x | | x | x | | x | xx |
| | S4 | x | x | x | | | xx | x | | x | | x | x |
| | S5 | x | x | x | | | x | x | x | | | | **xx** |
| | S6 | x | | x | | | x | | x | x | | x | xx |
| | S7 | | x | | x | | x**x** | x | | x | | x | x |
| | S8 | | x | x | | x | x**x** | | x | | x | | xx |
| | S9 | | x | xx | | | x | | | xx | x | | x**x** |
| | S10 | x**x** | | | x | x | **x** | | | | x | | x**x** |
| **Neu** | S1 | x | x | x | x | | x | | | | xx | xx | x |
| | S2 | x**x** | x | | | x | | | | | x | x | x |
| | S3 | x | x | | | x | x | xx | x | x | | x | **x** |
| | S4 | x | | x | | x | x | x | | x | | x | xx |
| | S5 | | xx | x | x | | xx | x | x | | x | | x**x** |
| | S6 | **x** | x | x | | xx | x | | xx | | x | x | x |
| | S7 | x | x | | x | | x**x** | x | | x | | x | x |
| | S8 | | xx | | x | x | x | | x | | x | xx | x |
| | S9 | | xx | x | | | x | | x | x | x | | x |
| | S10 | x**x** | | | x | | xx | | | x | | xx | **x** |
| **Sup** | S1 | x | | x | | x | | x | | | x | x | x |
| | S2 | x**x** | x | x | x | | | | x | | x | | |
| | S3 | | x | x | x | x | | | x | x | | x | xx |
| | S4 | x | x | x | | x | x | | xx | x | | | xx |
| | S5 | | x | x | x | | x | | x | | | xx | |
| | S6 | x | | x | | xx | x | | x | x | | | xx |
| | S7 | x | x | | x | | x**x** | x | | | x | x | |
| | S8 | x | x | | | x | x | x | x | | x | x | xx |
| | S9 | | x | xx | | x | | | | x | x | x | x**x** |
| | S10 | x | **x** | x | x | | xx | | | | x | x | **x** |
| Σx | | 20 | 26 | 23 | 13 | 18 | 26 | 11 | 15 | 16 | 19 | 25 | 32 | 
| Σx | | 6 | 1 | 0 | 0 | 0 | 6 | 0 | 0 | 0 | 0 | 1 | 8 |

Total: 245
Σx total: 22
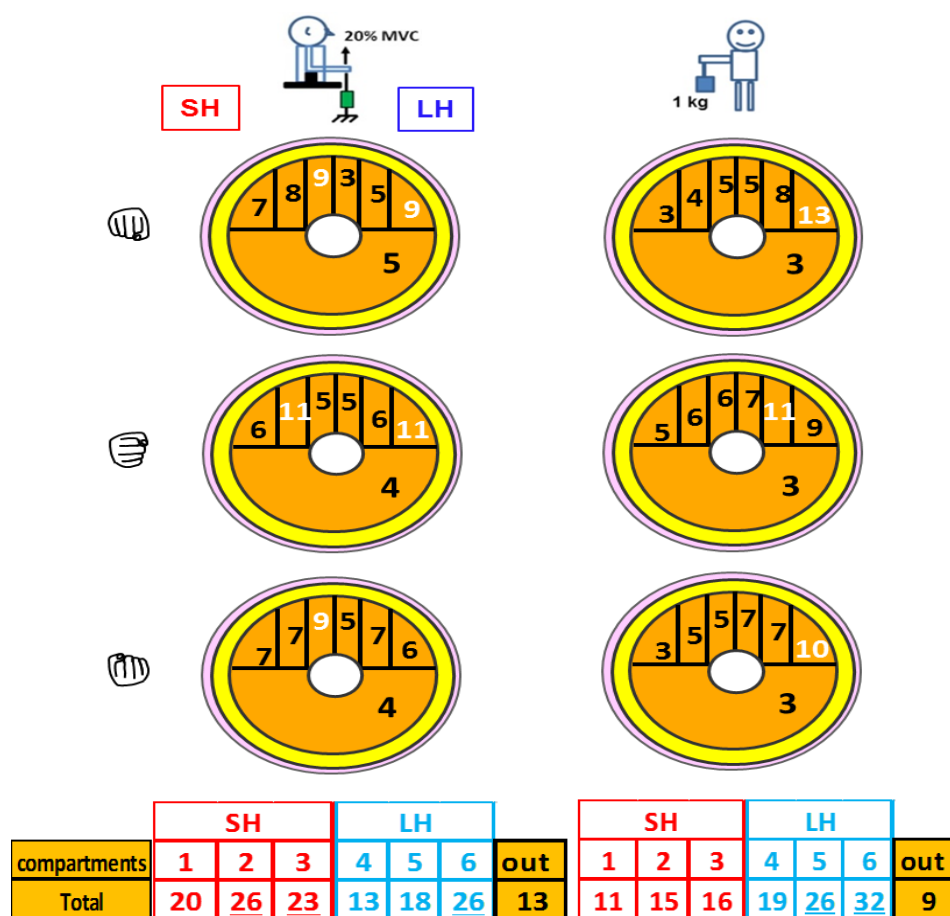
Figure 4.19: For all subjects, distribution of dipoles in each assumed compartments of the biceps. Figures below the biceps outline correspond to dipoles found outside its compartments. The total number of dipoles within each compartment for each hand position and outside the biceps is presented at the bottom.

# CHAPTER 5   DISCUSSION

From 60 ensembles of 10 EMG signals that had been recorded over the biceps brachii of healthy subjects, a peak fitting method was used to get an initial estimation of the dipoles that could have been at their origin. Using the COMSOL multiphysics simulation software with the characteristics of those dipoles as inputs, and modeling the upper arm as a cylinder, the results of the simulations were compared to the experimental data and an error function was used to have a measure of the difference between experimental and simulation results. Two different models of the upper arm were experimented: a simple 1-layer model with the cylinder filled with an homogeneous muscular tissue and a 4-layer model to represent the skin, the fat layer, the muscle tissue and the humerus bone. Various thicknesses of the fat layer and of the muscular tissue were experimented and muscle anisotropy was considered.

To assert our ability to master the use of the COMSOL software, we initially tried to duplicate the analytical results of Lambin and Troquet [33].With an extremely fine mesh resolution, when our results were superposed to theirs, the match was perfect. To strengthen our confidence we also tried to duplicate the Saitou et al [34] results where the image method was used to analyze 16 surface EMG signals recorded across the biceps for the purpose of associating them with dipoles inside the muscle. They found up to 6 dipoles characterized by their depth below the electrodes and by their intensities in nA.m. From their 3D graphics displaying amplitude of each of the 16 the EMG signals along a time axis, an estimate of the temporal delay between the dipoles was obtained using a conduction velocity within muscle fibers of 4 m/s. With the available depths, intensities and delays, we did not succeeded to duplicate their results. This is because some crucial information was lacking in the article. For example in their 3D figures an amplitude scale is lacking and in their contour figures, no color bar was provided. In addition some of the dipole depths below the skin were too small to be valid. So, validity of our use of the COMSOL software is not the element which prevented the duplication of the results of those authors.

We started our simulations with the 1-layer model due to its simplicity to implement and then moved to the 4-layer model which is closer to the anatomical reality but is still far from the duplicating a real cross-section of the arm. In some articles, magnetic resonance images (MRI) of the arm were taken and duplicated in finite element models [37], [39]-[40] but for the purpose of

simply locating bundles of many active muscles fibers within the biceps, we considered that such a detailed model was not required. So for our goals, the 4-layer model as used by Lowery et al. [40, 41], Roelveld et al. [35], Chauvet et al. [36] and Farina et al. [38] was considered as our most appropriate choice. Among the four variants of the 4-layer models considered (Figure 4.1, p.54), the D model was chosen as more representative of our 10 subjects.

The initial dipole characteristics where obtained by a peak method which is simple and produces results rapidly but have some weaknesses. For one, the arm is modelled as a single cylinder filled with a homogeneous and isotropic medium which is somewhat different from our 4-layer anisotropic model. Also, the radial position of the dipoles is estimated from curves obtained with the Okada equation when a dipole is moving radially from the border of the cylinder toward its center. This is considered equivalent to a dipole moving along the length of the muscle fibers but this have yet to be demonstrated. On the other hand, the angular position of the dipoles could be considered reliable since derived from the peaks on an interpolated curve of the 10 RMS experimental values. The same applies to the relative dipole intensities determined from the relative amplitude of the detected peaks.

In our COMSOL model, dipoles are placed in the middle of two rows of the 10 electrodes and that position was always fixed in our simulations. For a more realistic simulation, the current dipoles would be moving at a constant velocity from one end to the other one of the cylinder. Being in a linear system, the addition of each dipole potential associated to such a displacement is expected to give the same results as when all dipoles are moving simultaneously. As shown in Figure 5.1 the superposition of the results (B panel) do not match perfectly the curve in panel A. This is due to the different mesh distribution between the two situations.

In few recorded EMG signals, abnormally large RMS values were observed from 1 or 2 recording sites. That generally occurred with the extension of the elbow angle from 90° to 180° following moving from the seating to the standing up position. Elongation of the biceps appears to have been accompanied by a stretching of the skin which altered the quality of the electrode/skin contact making it more prone to noise contamination.
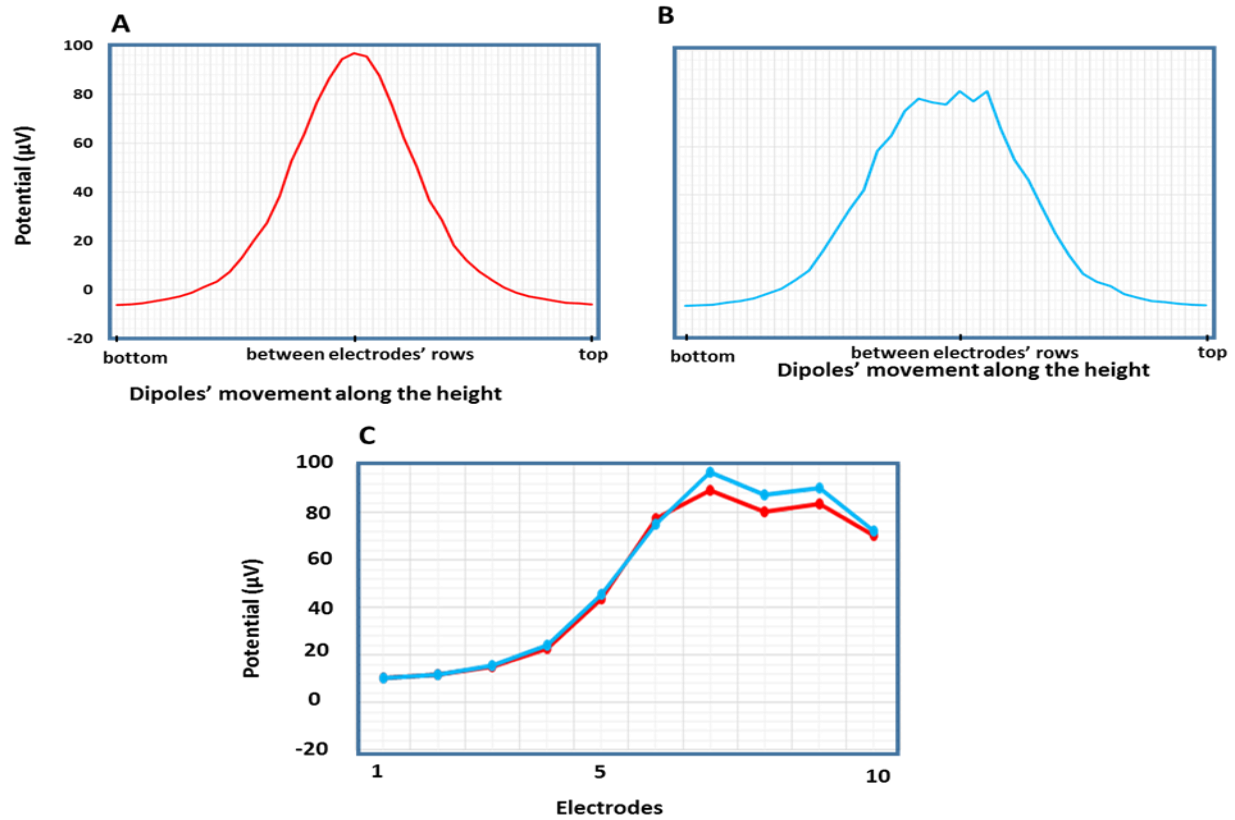
Figure 5.1: Change in potential generated by 5 dipoles moving from the bottom to the top of the 4-layer cylindrical anisotropic model (data from S1 standing up with the hand in neutral posture). **A:** Simultaneous displacement of the 5 dipoles recorded with electrode No.7. **B:** The 5 dipoles were moved individually and their individual potentials summed recorded with dipole No.7. **C:** Potential obtained at each recording electrodes pair as in panel A when all dipoles were simultaneously moved from bottom to the top (blue curve) and when all dipoles were fixed and positioned between the two rows of electrodes (red curve).

In our simulations, the dipole angular and radial positions were manually modified for the purpose of reducing the error between experimental and simulated results. This goal was achieved but it was time consuming, intra-and inter-operator dependant and the final results may not be the best ones. So the use of optimizing methods such as genetic algorithm have to be considered.

With the MKS units system used in COMSOL, simulation results were expressed in µV as were the 10 experimental RMS values. However, since only relative intensity of the dipoles was obtained with the peak method, in COMSOL, an arbitrary value of 100 nA.m was proportionally shared between the dipoles based on their relative intensity. So for both experimental results and

simulation date, a scaling factor was thus required. We used an interval ranging from 1.2 to 3.2 because it allowed to illustrate the results of the 3 hand postures side by side which facilitated comparisons between them.

When we started the project, due to a lack of information on the contours and location of the compartments within the biceps, we simply divided the semicircular representation of the biceps in 6 compartments of equal surface each separated by a vertical line as used in our figures. In search of that information, we came across the American visual human project (VHP) where cross- section high definition images were available. In Figure 5.2 is shown three images of the right arm of the male subject, each separated by 10 mm. On those images, part of the contour of the long head (blue) and of the short head (red) were easily tracked (solid lines) while other segments, in spite of the high resolution of the images, where guessed as the more plausible path (dotted lines). Within the muscle, 5 or 6 compartments could be identified on those images obtained close to the mid part of the muscle. While the images were not obtained in the position similar to our experiences, the shape of the biceps is a bit more similar to a section of an ellipse than of a circle. As for the compartments repartition within the muscle, this is definitively not similar to their assumed location in our model. Since those images are only representative of a single subject, a more significant number of subjects is required for a robust estimation of the compartments location within the biceps. For this purpose, a project is being planned to use the right and left biceps of 7 cadavers that will be imaged in their total length in small animals 7T MRI apparatus. In the obtained images, the presence of compartments will be tracked all along the muscle.

In our model, electrodes were dimensionless and simply represented the center of real electrodes. To get the real dimensions of electrodes, it would be necessary to consider them as flat cylinders and this could be possible, in COMSOL by using the geometry module. The dipoles are also defined as a simple point. In order to get a distance between the positive and negative pole, it would be necessary to define mono negative and positive poles with desired distance. However, the effect of this small gap between the poles of a dipole would not affect the final results.
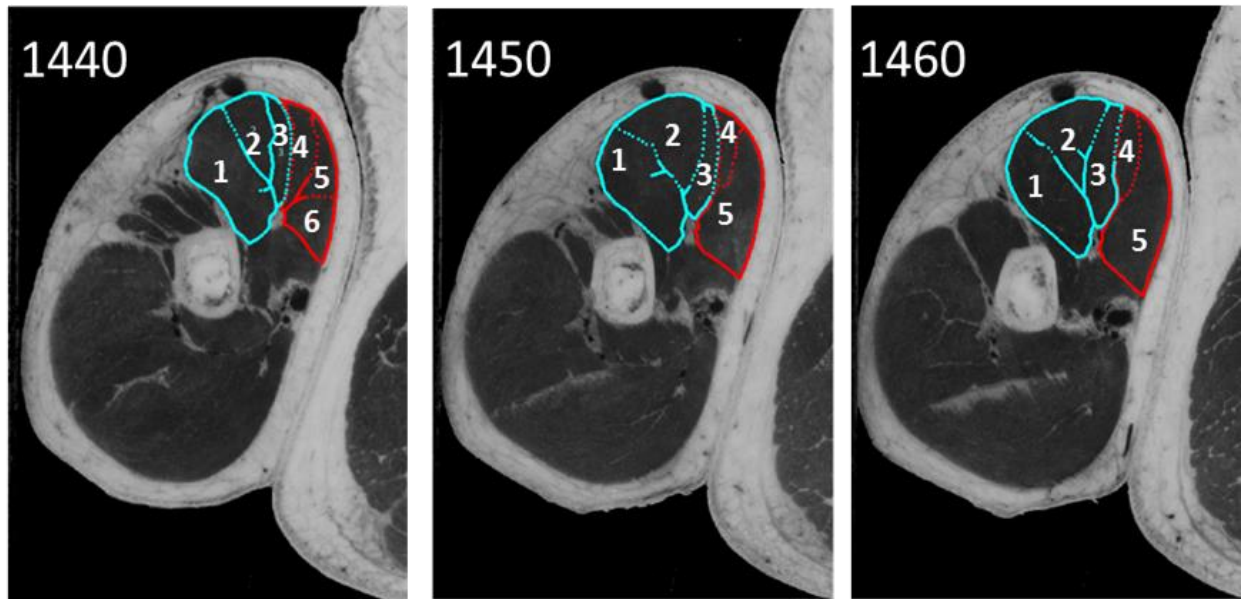
Figure 5.2: From the American Visual Human Project (VHP), high resolution photographs taken at 10 mm intervals near the middle of the upper arm right arm of the male subject. In color, outline of the long (blue) and short (red) heads of the biceps within which up to 6 divisions, associated to the muscles' compartments, are outlined.

# CHAPTER 6  CONCLUSION

Starting with a simple representation of the two head of the biceps and a naïve repartition of its 6 compartments, most of the dipoles that have been identified are located within those compartments. In the seated position, compartments of the SH were most often occupied than those of the LH and the inverse happened when in the standing up position. For those 2 positions, modifying the hand position does not seem to significantly change the dipole positions within each head. In those conditions (seating and standing up with 3 hand positions) it does not seem possible to activate only one compartment at the time. Amongst our tested upper arm models, the 4-layer anisotropic model provides the simulation results which best fitted the experimental data. Around 2% of the dipoles were located outside the biceps. They could be attributed to crosstalk activity but having most of the time a small relative intensity, their contribution to the signal recorded at the skin surface was minimal.
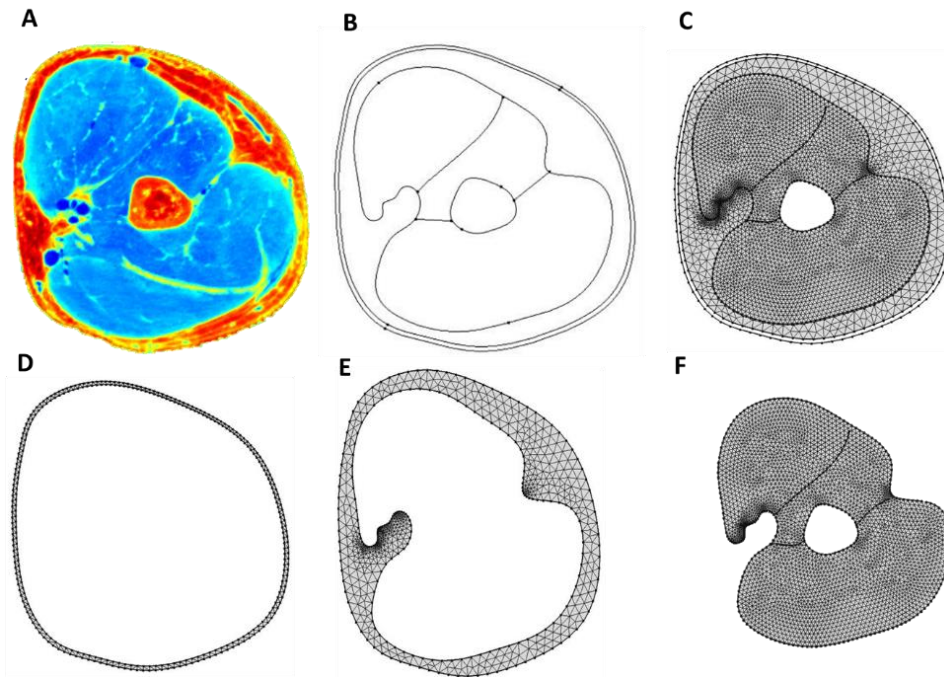


Figure 6.1: Our COMSOL mesh model of the upper arm based on a magnetic resonance image copied from the web. **A:** Colored cross section image of the right upper arm **B:** With a segmentation of the contours, a 2D model is obtained. **C:** Mesh model of the skin and fat layers plus the biceps (top) the brachialis (middle) and triceps (bottom) muscles and the humerus bone in the center. **D:** Skin layer alone. **E:** Fat layer. **F:** Biceps, brachialis and triceps only.

While the 4-layer model was more realistic than the 1-layer one, an even more realistic model could be considered. For this purpose, magnetic resonance images are the best candidates. This is illustrated in Figure 6.1 where accurate thickness of the skin and fat layers can be obtained all around the arm and where more realistic contours of the muscles would indicate more easily where the detected dipoles are really located within the muscular tissues.

Our results were obtained by manually improving the dipole's location which is a tedious task that can be alleviated by using optimization algorithms which could possibly lead to better results. For each of the 10 subjects, ultrasound images were collected over the biceps at the level where the electrodes had been previously placed to record the EMG signals. By analysing those images with recent elastography techniques, it would be possible to locate zones of mechanical tension within the biceps which are expected to have a good correspondence with the electrical dipole locations.
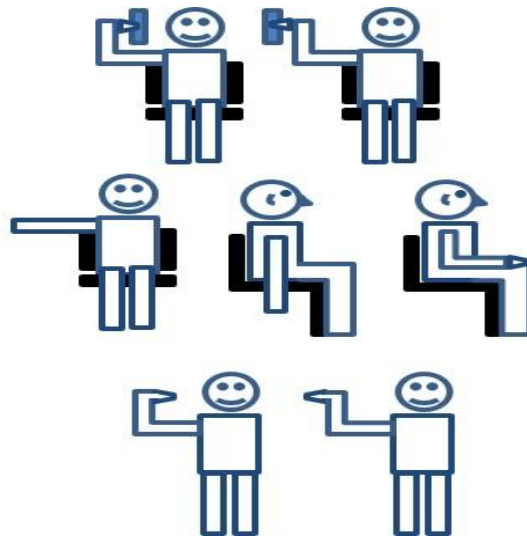


Figure 6.2. Seven other experimented body positions for which data is available for the 3 hand positions experimented.

So far, experimental results were only obtained from healthy subjects in some seating and standing up positions because they appeared as the most interesting to analyze first. But there are also 7 other positions (Figure 6.2) which were explored by 3 to 9 subjects which are worth to study but have not yet been analyzed. Finally, besides normal subjects, data from amputee persons should also be collected to identify how they could manage to activate their biceps.

# BIBLIOGRAPHY

[1]     E. N. Marieb, J. Mallatt, and P. Brady, *Human Anatomy*, 5 ed. San Francisco, CA: Pearson Benjamin Cummings, 2008.

[2]     *Radius and Ulna*. Available: http://www.kidport.com/reflib/science/humanbody/ skeletalsystem/radiusulna.htm

[3]     D. A. Neumann, "Kinesiology of the musculoskeletal system: foundations for rehabilitation. St Louis, MO: Mosby," ed: Elsevier, 2010.

[4]     L. Lippert, "R. Library," *Clinical Kinesiology and Anatomy, FA Davis, Philadelphia,* 2006.

[5]     D. Shier, R. Lewis, and J. Butler, "Hole's Human Anatomy and Physiology. 10th," ed: New York, USA: McGraw-Hill, 2004.

[6]     A. J. Vander, J. H. Sherman, and D. S. Luciano, *Human physiology : the mechanisms of body function*. Boston, Mass.: McGraw-Hill, 2001.

[7]     E. Quinn. (2015). *Concentric Muscle Contraction*. Available: http://sportsmedicine.about.com/od/glossary/g/Concentric_def.htm

[8]     N. Mazzaro. Monopolar electromyographic (EMG ) needles [Online].

[9]     M. Z. Jamal. (2012). *Signal Acquisition Using Surface EMG and Circuit Design Considerations for Robotic Prosthesis, Computational Intelligence in Electromyography Analysis*. Available: http://www.intechopen.com/books/computational-intelligence-in-electromyography-analysis-a-perspective-on-current-applications-and-future-challenges/signal-acquisition-using-surface-emg-and-circuit-design-considerations-for-robotic-prosthesis

[10]    L. A. Cohen, "Localization of Stretch Reflex," *Neurophysiology,* vol. 16, pp. 272-285, 1953-05-01 1953.

[11]    O. Weeks and A. English, "Compartmentalization of the cat lateral gastrocnemius motor nucleus," *Journal of Comparative Neurology,* vol. 235, pp. 255-267, 1985.

[12]    C. Chanaud, C. Pratt, and G. Loeb, "Functionally complex muscles of the cat hindlimb," *Experimental brain research,* vol. 85, pp. 257-270, 1991.

[13]    C. Widmer, D. Carrasco, and A. English, "Differential activation of neuromuscular compartments in the rabbit masseter muscle during different oral behaviors," *Experimental brain research,* vol. 150, pp. 297-307, 2003.

[14]    A. M. Lucas-Osma and J. E. Collazos-Castro, "Compartmentalization in the triceps brachii motoneuron nucleus and its relation to muscle architecture," *Journal of Comparative Neurology,* vol. 516, pp. 226-239, 2009.

[15]    J. M. Wakeling, "The recruitment of different compartments within a muscle depends on the mechanics of the movement," *Biology Letters,* vol. 5, pp. 30-34, 2009.

[16]    E. B. Paré, J. Stern, and J. Schwartz, "Functional differentiation within the tensor fasciae latae. A telemetered electromyographic analysis of its locomotor roles," *The Journal of Bone & Joint Surgery,* vol. 63, pp. 1457-1471, 1981.

[17]  J. F. Paton, "A working heart-brainstem preparation of the mouse," *Journal of neuroscience methods,* vol. 65, pp. 63-68, 1996.

[18]  A. Holtermann, K. Roeleveld, P. J. Mork, C. Grönlund, J. S. Karlsson, L. L. Andersen*, et al.*, "Selective activation of neuromuscular compartments within the human trapezius muscle," *Journal of Electromyography and Kinesiology,* vol. 19, pp. 896-902, 2009.

[19]  J. Wickham and J. Brown, "Muscles within muscles: the neuromotor control of intra-muscular segments," *European journal of applied physiology and occupational physiology,* vol. 78, pp. 219-225, 1998.

[20]  J. Brown, J. Wickham, D. McAndrew, and X.-F. Huang, "Muscles within muscles: coordination of 19 muscle segments within three shoulder muscles during isometric motor tasks," *Journal of Electromyography and Kinesiology,* vol. 17, pp. 57-73, 2007.

[21]  J. B. Wickham and J. Brown, "The function of neuromuscular compartments in human shoulder muscles," *Journal of neurophysiology,* vol. 107, pp. 336-345, 2012.

[22]  R. Segal, S. Wolf, M. DeCamp, M. Chopp, and A. English, "Anatomical partitioning of three multiarticular human muscles," *Cells Tissues Organs,* vol. 142, pp. 261-266, 1991.

[23]  J.-H. Lee, H.-W. Kim, S. Im, X. An, M.-S. Lee, U.-Y. Lee*, et al.*, "Localization of motor entry points and terminal intramuscular nerve endings of the musculocutaneous nerve to biceps and brachialis muscles," *Surgical and radiologic anatomy,* vol. 32, pp. 213-220, 2010.

[24]  R. L. Segal, "Neuromuscular compartments in the human biceps brachii muscle," *Neuroscience letters,* vol. 140, pp. 98-102, 1992.

[25]  *Dielectric Properties*. Available: http://www.itis.ethz.ch/virtual-population/tissue-properties/database/dielectric-properties/

[26]  D. Andreuccetti, R. Fossi, and C. Petrucci. (1997). *An Internet resource for the calculation of the dielectric properties of body tissues in the frequency range 10 Hz - 100 GHz. ( Based on data published by C.Gabriel et al. in 1996.)*. Available: http://niremf.ifac.cnr.it/tissprop/

[27]  C. Gabriel, S. Gabriel, and E. Corthout, "The dielectric properties of biological tissues: I. Literature survey," *Physics in medicine and biology,* vol. 41, p. 2231, 1996.

[28]  *Myoelectric Prosthetics*. Available: http://www.myoelectricprosthetics.com/

[29]  R. F. Weir and J. W. Sensinger, "Design of artificial arms and hands for prosthetic applications," ed: McGraw Hill, New York, 2003, pp. 32.1-32.61.

[30]  R. H. Okada, "Potentials produced by an eccentric current dipole in a finite-length circular conducting cylinder," *Medical Electronics, IRE Transactions on,* pp. 14-19, 1956.

[31]  E. Frank, "The zero-potential contour on a homogeneous conducting cylinder," *Medical Electronics, Transactions of the IRE Professional Group on,* pp. 27-40, 1953.

[32]  H. C. Burger, *Heart and vector: physical basis of electrocardiography*: NV Philips' Gloeilampenfabrieken, 1968.

[33]  P. Lambin and J. Troquet, "Complete calculation of the electric potential produced by a pair of current source and sink energizing a circular finite-length cylinder," *Journal of Applied Physics,* vol. 54, pp. 4174-4184, 1983.

[34]    K. Saitou, T. Masuda, and M. Okada, "Depth and intensity of equivalent current dipoles estimated through an inverse analysis of surface electromyograms using the image method," *Medical & biological engineering & computing,* vol. 37, pp. 720-726, 1999.

[35]    K. Roeleveld, J. Blok, D. Stegeman, and A. Van Oosterom, "Volume conduction models for surface EMG; confrontation with measurements," *Journal of Electromyography and Kinesiology,* vol. 7, pp. 221-232, 1997.

[36]    E. Chauvet, O. Fokapu, and D. Gamet, "Inverse problem in the surface EMG: A feasibility study," in *Engineering in Medicine and Biology Society, 2001. Proceedings of the 23rd Annual International Conference of the IEEE*, 2001, pp. 1048-1050.

[37]    R. A. Jesinger and V. L. Stonick, "Processing signals from surface electrode arrays for noninvasive 3D mapping of muscle activity," in *Digital Signal Processing Workshop, 1994., 1994 Sixth IEEE*, 1994, pp. 57-60.

[38]    D. Farina, L. Mesin, S. Martina, and R. Merletti, "A surface EMG generation model with multilayer cylindrical description of the volume conductor," *Biomedical Engineering, IEEE Transactions on,* vol. 51, pp. 415-426, 2004.

[39]    K. Van Den Doel, U. M. Ascher, and D. K. Pai, "Computed myography: three-dimensional reconstruction of motor functions from surface EMG data," *Inverse Problems,* vol. 24, p. 065010, 2008.

[40]    M. M. Lowery, N. S. Stoykov, J. Dewald, and T. Kuiken, "Volume conduction in an anatomically based surface EMG model," *Biomedical Engineering, IEEE Transactions on,* vol. 51, pp. 2138-2147, 2004.

[41]    M. M. Lowery, N. S. Stoykov, A. Taflove, and T. Kuiken, "A multiple-layer finite-element model of the surface EMG signal," *Biomedical Engineering, IEEE Transactions on,* vol. 49, pp. 446-454, 2002.

[42]    S. Gabriel, R. Lau, and C. Gabriel, "The dielectric properties of biological tissues: III. Parametric models for the dielectric spectrum of tissues," *Physics in medicine and biology,* vol. 41, p. 2271, 1996.

[43]    N. Nejat, "Study on the activation of the biceps brachii compartments in normal subjects," Master of research, Biomedical Engineering, University of Montreal, Canada, 2012.

[44]    J. R. Florestal, P. A. Mathieu, and K. C. McGill, "Automatic decomposition of multichannel intramuscular EMG signals," *Journal of Electromyography and Kinesiology,* vol. 19, pp. 1-9, 2// 2009.

[45]    B. J. Roth, "The electrical conductivity of tissues,"  vol. 1, 2 ed: Boca Raton, FL: CRC Press, 2000, pp. 10.1-10.12.

# APPENDIX A: CONDUCTIVITY AND PERMITTIVITY OF BIOLOGICAL TISSUES[4].

In the study of electrical activity in the body and its manifestation at the body surface, electrodes are frequently used to measure voltages resulting from ionic currents associated either to the activity of the brain, the heart, or muscles. To associate those surface potentials to their internal sources, the potential distribution (V) within the volume conductor, which is the different tissues interposed between the sources and the surface, has to be known. Considering that the variations of the surface potential are often below 1 kHz), the quasi-static Maxwell equations can be used since the capacitive as well as the inductive effects can be neglected. Then, the divergence of the current density J ($A/m^2$) is equal to the applied or endogenous electrical current S ($A/m^3$):

$$\nabla . \mathbf{J} = \mathbf{S}$$

Between the current source and the surface, S=0 in the volume conductor and the divergence of the current density is prevented. The conservation of current law then applies as well as the volume conductor property which makes the current density linearly related to the electric field **E** (V/m) by Ohm's law:

$$\mathbf{J} = g\,\mathbf{E}$$

where g is the electrical conductivity (S/m) and **E** is related to the potential gradient $\nabla$:

$$\mathbf{E} = -\nabla \boldsymbol{\Phi}$$

Conductivity of a biological tissue is difficult to obtain since it is a macroscopic parameter while an experimental measure represents an average property obtained over many of the tissue constituents. Also, as with muscular fibers, conductivity can be anisotropic depending if the measure is done along or perpendicularly to the main direction of the fibers.

To examine the dielectric properties of tissues, a very simple volume conductor is initially considered. In a saline solution for example, conductivity (~1 S/m) depends on the motion of its free ions when an electric field is applied. As for permittivity ($\varepsilon$), it is associated to the

---

[4] Information and figures in this Appendix is based on a book chapter written by Roth [45]

dimensionless dielectric constant k by $\varepsilon=k\varepsilon_0$ where $\varepsilon_0 = 8.854\times10^{-12}$ is the permittivity of free space. Dielectric properties are associated to a bound charge which when displaced by an electric field becomes a dipole. A dielectric behavior is also present when an electric field aligns molecular dipoles as the dipole moments of water molecules.

While the movement of free charges produces conductivity, stationary dipoles produce permittivity. In a steady state condition, distinction between conductivity and permittivity is easy but at higher frequencies those concepts merge and a complex conductivity $\acute{g}$ is considered:

$$\acute{g} = g + i\omega\varepsilon$$

where the real part g corresponds to the charges' exchanges which is in phase with the electric field while the imaginary part corresponds to the out-of-phase motion where $\omega$ (rad/s) is the angular frequency considered. In many bioelectric phenomena, g is much larger than the imaginary part and the tissue can considered as only conductive which applies to us since we are dealing only with signals of low-frequency content (i.e. < 1 kHz).

The simplest model to describe the electrical conductivity of a biological tissue is simply a suspension many identical spherical cells in a saline solution (Figure A.1a) placed within a tube having a length L and a cross section A. With a DC voltage V applied at the ends of the cylinder, an electric current I flows through the suspension creating a V/L electric field and the effective conductivity of the model is IL/VA. The thin membrane of each cells separating the extracellular volume from the intracellular one has as, per unit area, a Gm (S/m2) conductivity and a Cm (F/m2) capacitance. To specify how tightly the cells are packed together, a dimensionless volume fraction (f) is used: f= ~0 for a dilute solution and f= ~1 for a very concentrated solution where non-spherical cells are used to fill all the space.

In most cases, cells conductivity Gm is small enough that the membrane can be considered as an insulator for a DC voltage. Acting as insulated spheres, the cells presence decreases the conductivity of the saline solution proportionally to the density of their packing. With an alternative field, the cell membrane capacitance (~0.01 (F/m2) has a frequency effect on its conductivity.
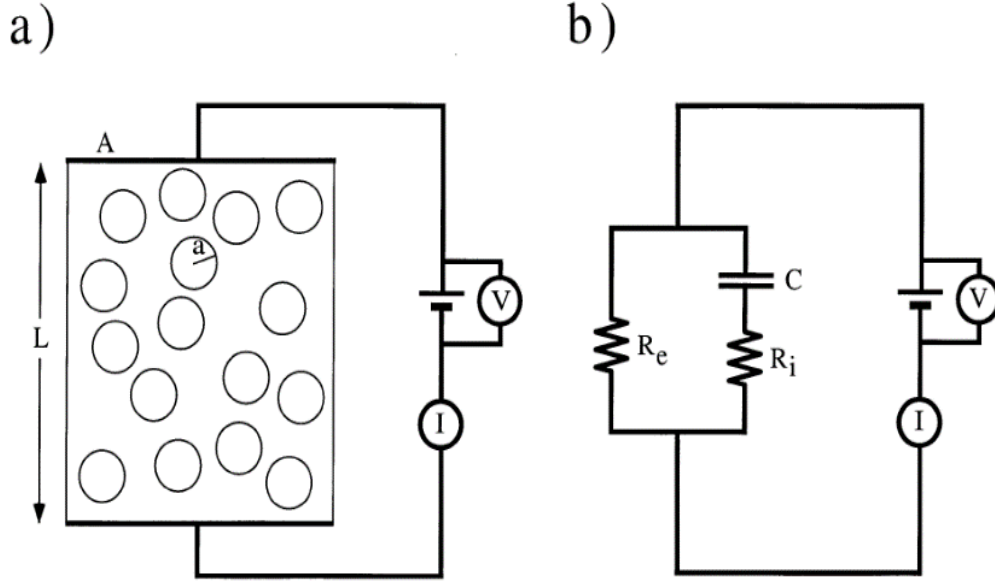
Figure A.1: Suspension of the spherical cells with conductivity IL/VA. b) Electric circuit corresponding to the effective conductivity of the saline solution

The suspension of cells can then be modeled as in Figure A.1b where Re is the effective resistance to current flowing entirely in the interstitial space, $R_i$ the resistance to current passing entirely in the intracellular space and C the effective capacitance. The membrane capacitance is generally small enough that it has minor effect on the cells suspension behavior at any frequency.

While at low frequencies, the entire current flow is restricted to the interstitial space, at high frequencies, current is crossing the membrane and conductivity becomes:

$$g = \frac{2(1-f)\sigma_e + (1+2f)\sigma_i}{(2+f)\sigma_e + (1-f)\sigma_i} \sigma_e.$$

At intermediate frequencies, the effective conductivity has real and imaginary parts due to the membrane capacitance and the above equation is still valid if $\sigma_i$ is substituted by $\sigma_i^*$ where:

$$\sigma_i^* = \frac{\sigma_i Y_m a}{\sigma_i + Y_m a}, \qquad \text{with} \qquad Y_m = G_m + i\omega c_m,$$

The magnitude of effective conductivity respect to frequency for a typical tissue is shown Figure A.2.

Some of the most interesting electrically active tissues, like nerve or skeletal muscle are more appropriately assimilated to a suspension of fibers instead to a suspension of spherical structures. This introduces anisotropy: related to the fibers direction, we have a value for the longitudinal conductivity ($g_L$) and another one for the transverse conductivity ($g_T$). While there is a conductivity value for each of the 3 spatial dimensions, it is assumed that both perpendicular dimensions to the fibers direction have the same conductivity and conductivity is not more a scalar quantity.
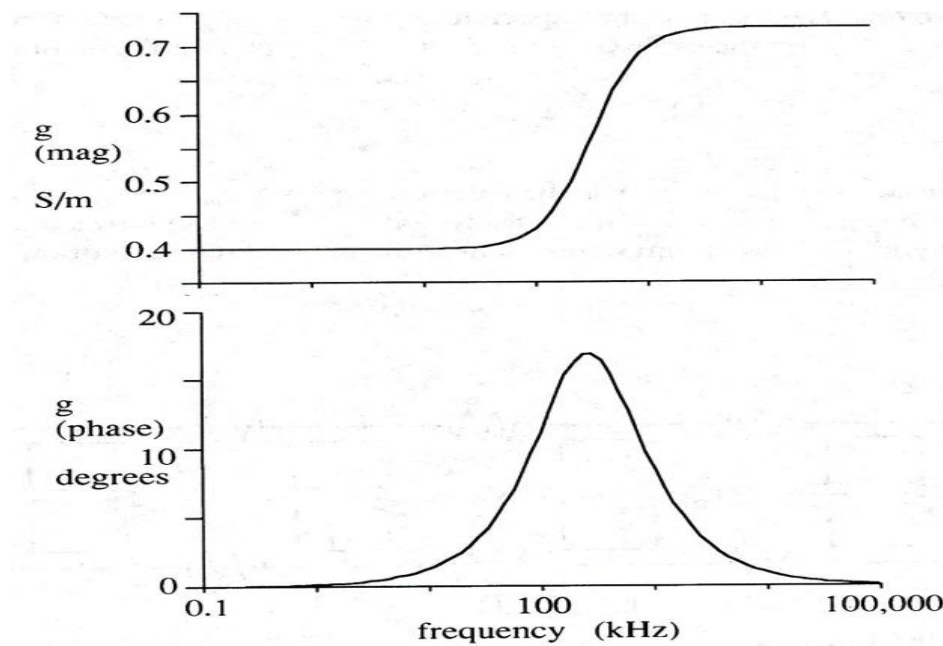


Figure A.2: The magnitude of the effective conductivity respect to the frequency, for a suspension of spherical cells: f = 0.5; a= 20 μm; $\sigma_e$=1 S/m; $\sigma_i$=0.5 S/m; $G_m$ = 0; $C_m$ = 0.01 F/m2

When the electrical field is perpendicular to the fibers' direction then a suspension of the fibers appears as in Figure A.3 considering that the circles then represent the cross-section of the cylindrical fibers. Then, the effective transverse conductivity of cylindrical cells of radius "a" and intracellular conductivity $\sigma_i$ placed in a saline solution of conductivity $\sigma_e$ and where volume fraction is f is given by:

$$g_T = \frac{(1-f)\sigma_e + (1+f)\sigma_i^*}{(1+f)\sigma_e + (1-f)\sigma_i^*}\sigma_e$$

which becomes at DC (assuming Gm = 0):

$$g_T = \frac{(1-f)}{1+f}\sigma_e$$

A new behavior happens when the electrical field is along to the fibers since the effective longitudinally conductivity then depends on the length (L) of the tissue. Considering one-dimensional cable theory, a single nerve or skeletal muscle fiber can be approximated by the circuit shown in Figure A.3 where, per unit length, $r_i$ and re respectively represents the intracellular and extracellular resistance ($\Omega$/m) while $r_m$ is the membrane resistance ($\Omega$/m) and $c_m$ its capacitance (F/m).
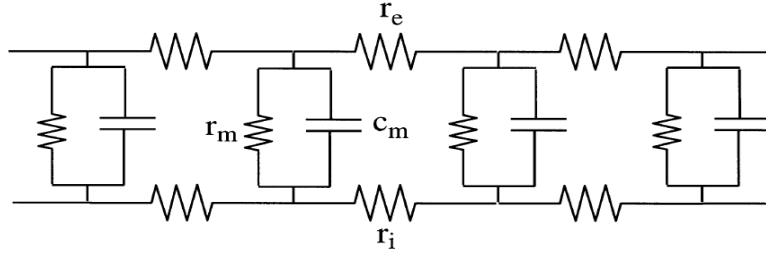


Figure A. 3: One dimensional electrical circuit of a nerve or skeletal muscle fiber.

The transmembrane potential $V_m$ is governed by the cable equation:

$$\lambda^2 \frac{\partial^2 V_m}{\partial x^2} = \tau \frac{\partial V_m}{\partial t} + V_m$$

where $\tau$ is the time constant $(r_m\, c_m)$ and $\lambda$ is the length constant $(\sqrt{r_m/r_i + r_e})$. For a truncated fiber with sealed ends and length L (m), and with a steady-state current I (A) inserted into the extracellular space at one of ends and exited from the other end, the solution to the cable equation becomes:

$$V_m = I\, r_e\, \lambda\, \frac{\sinh(x/\lambda)}{\cosh(L/2\lambda)},$$

where the origin of the x-axis is at the midpoint between electrodes. The extracellular potential ($V_e$) has two terms: one proportional to x, and the other one is $i_e/(r_i + r_e)\,V_m$. With evaluating $V_e$, the voltage drop ($\Delta V_e$) between the electrodes at the two ends of the fiber is:

$$\Delta V_e = \frac{r_i r_e}{r_i + r_e} I \left[ L + \frac{r_i}{r_e} 2\lambda \tanh(L/2\,\lambda) \right]$$

Two cases are of interest: when L is much larger or much smaller than $\lambda$. When $L \gg \lambda$, the drop in the extracellular voltage is given by:

$$\Delta V_e = \frac{r_i r_e}{r_i + r_e} L\,I \qquad L \gg \lambda$$

where the leading factor is the parallel combination of ri and re . When L is much smaller than $\lambda$, the extracellular voltage drop is:

$$\Delta V_e = r_e\,L\,I \qquad L \ll \lambda$$

where the leading factor is now the extracellular resistance alone. So, when $L \gg \lambda$, the current is redistributed completely between the intracellular and extracellular spaces while in the opposite situation ($L \ll \lambda$), the current cannot penetrate in the fiber and is restricted to the extracellular space. In both cases, the effective conductivity ($IL/A\Delta V_e$) where A is the cross sectional area of the tissue strand, does not depend on L. In the case where $L \approx \lambda$, then the effective conductivity is influenced by the size of the sample. When longitudinal conductivity is expressed in spatial frequency k (rad/m) the length of the sample used for the experimental measurements is no more required. Then, the spatial frequency dependence is on the tissue property not on the source. The DC effective longitudinal conductivity is then:

$$g_L = \frac{(1-f)\sigma_e + f\sigma_i}{1 + \frac{f\sigma_i}{(1-f)\sigma_e} \frac{1}{1+\left(\frac{1}{\lambda k}\right)^2}}$$

where $1/k$ takes the place of L in previous equations. Amplitude and phase of the longitudinal and transverse effective conductivities as functions of the temporal (dashed lines) and spatial frequencies are shown in Figure A.4 for the parameters indicated.
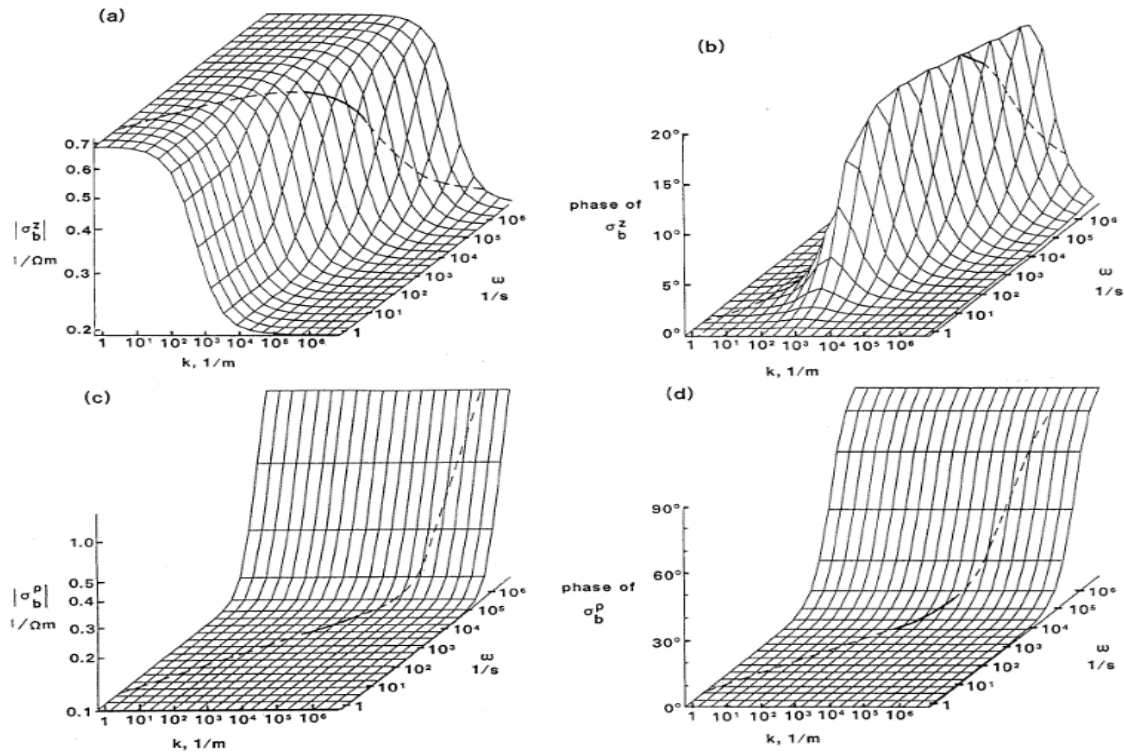
Figure A.4: Spatial, k (full lines) and temporal, **ω**, frequency model (dotted lines). (a) amplitude of the effective longitudinal conductivity and (b) its phase. (c) amplitude of the effective transverse conductivity and (d) its phase. The applied parameters were: Gm = 1 S/m2; C = 0.01 F/m2; f= 0.9; a = 20 **μ**m; $\sigma_i$ = 0.55 S/m; and $\sigma_e$ = 2 S/m.

Conductivity measurements are made with a traditional 4 electrodes setup where two electrodes are used to inject current while the 2 others are used to measure the potential as shown in Figure A.5.



Figure A.5: Four-electrode method, measuring tissue conductivities. Current, I, is flowed toward the two distanced electrodes, and the potential, V, is measured between the two close ones. The equidistance electrode is s.

An example of such measurements is given in Figure A.6 while typical macroscopic effective conductivities and microscopic tissue parameters of skeletal muscle are presented in Table A.1 from 3 different studies.
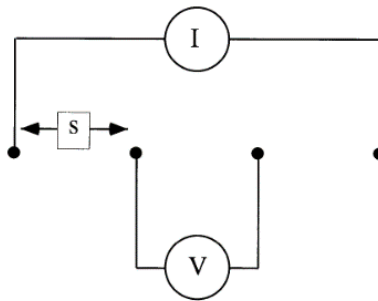
Table A.1 Skeletal muscle conductivity values

| Ref. | $g_L$ | $g_T$ | Note |
|---|---|---|---|
| Macroscopic Effective Conductivities (S/m) | | | |
| Gielen et al., 1984 | 0.35 | 0.086 | 10 Hz, IED = 3 mm |
| | 0.20 | 0.092 | 10 Hz, IED = 0.5 mm |
| Epstein and Foster, MBEC, 21:51 | 0.52 | 0.076 | 20 Hz, IED = 17 mm |
| | 0.70 | 0.32 | 100 kHz, IED = 17 mm |
| Rush et al., Circ Res, 12:40 | 0.67 | 0.040 | 0.1 sec pulse |

| | $\sigma_i$ (S/m) | $\sigma_e$ (S/m) | f | $C_m$ (F/m$^2$) | $G_m$ (S/m$^2$) |
|---|---|---|---|---|---|
| Microscopic Tissue Parameters | | | | | |
| Gielen et al., MBEC, 24:34 | 0.55 | 2.4 | 0.9 | 0.01 | 1.0 |

*Note:* (IED = interelectrode distance).

In addition to the Roth chapter, we consulted some of Gabriel et al., articles and considered of interest for biological tissues conductivities.

In the 1990 decade, research was being conducted on electromagnetic dosimetry and there was a need to know what where the dielectric properties of biological tissues at various frequencies but no consensus was then available on such data. Gabriel et al. [27] thus made a literature review on dielectric data covering the previous 50 years.

The dielectric properties of a biological tissue caused by the interaction of electromagnetic radiation altogether with its constituents at the cellular and molecular level. The significant features of the dielectric spectrum of a biological tissue can be briefly explained as below:

1. The relative permittivity of a tissue may get values of up to 106 or 107 at range of frequency below 100 Hz.

2. The relative permittivity also decreases at high frequencies in three main ranges which are known as α, β, γ dispersions.

3. The γ dispersion, in the range of GHz (gigahertz), is because of the polarization of water molecules.

4. The β dispersion, in the range of hundreds of KHz (kilohertz), majorly is because of the polarization cellular membranes. This polarization treats as barriers to the movement of ions between the intra and extra cellular media. Rest of contributions in the β dispersion results from the polarization of protein and other organic macromolecules.

5. The α dispersion, in the range of the low frequencies, is caused by ionic diffusion processes at cellular membrane.

6. The finite ionic conductivities of tissues commensurate with behavior and magnitude of their ionic content and ionic mobility.

Reports regarding to the properties of tissues before 1950s were few and most of them are based on historical presentations instead practical records. The reports during 1950s and 1960s was still limits to few researchers. The data gathered from human tissue and in vivo measurements were in preference to data acquired from animal tissue and in vitro. Data, for in vitro measurements, gathered at very similar temperatures of the body and also very close time after death. The significant parts of the data were in graphical and logarithmic presentations rather than tabular and linear format. After that the tables were commonly used, a wider range of frequencies was considered.

Data presentations of different tissues in a range of frequency were graphically illustrated, also, temperature of the measurements, tissues details and references are mentioned at the legend. Moreover, to compare the different authors results, the same scale was applied except for those cases that the conductivity of tissue decreases lower than 0.01 S/m.

Gabriel et al [1996] their review includes all the main tissues for which there are 3 or more literature articles. Here we only present those related to our model where layers of skin, fat, muscle and bone are only considered. Also, being only interested to a less than 1 Khz frequency range we only present here that part of their figures. These tissues was illustrated in Figure A.6.

Conductivity and relative permittivity being two significant properties of biological tissues; there are many of web page references that offer those values for human body's tissues in different frequencies. Amongst them, there is a site where Gabriel et al., data are presented where characterizations of various tissues for frequencies from 10 Hz to 100 GHz are presented [42].

Several information (e.g. conductivity [S/m], relative permittivity, loss tangent, wavelength [m], penetration depth [m]) for about 58 tissues of human body can also be found in the site.
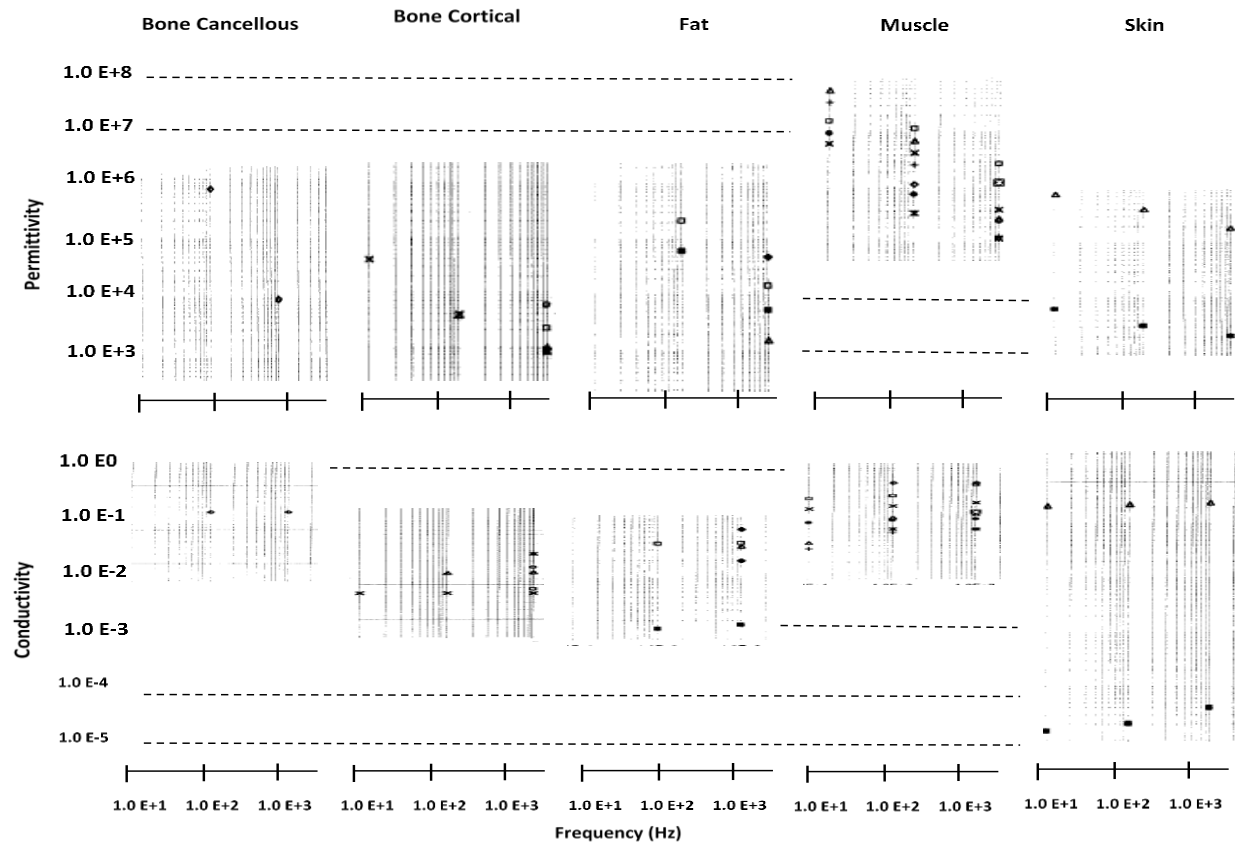


Figure A.6: Measured conductivity and relative permittivity from different researcher for bone cancellous, bone cortical, fat in range of low frequency 1 KHz. (From: http://niremf.ifac.cnr.it/ tissprop/htmlclie/htmlclie.htm).

Conductivity and relative permittivity can also be seen graphically in an interesting range of frequency as in Fig. A.7.

Figure A.7: Conductivity vs. relative permittivity for a specific tissue and in an interest range of frequency (from: http://www.itis.ethz.ch/virtual-population/tissue-properties/database/tissue-frequency-chart/).

## APPENDIX B:  DIFFERENT CONDUCTIVITY VALUES

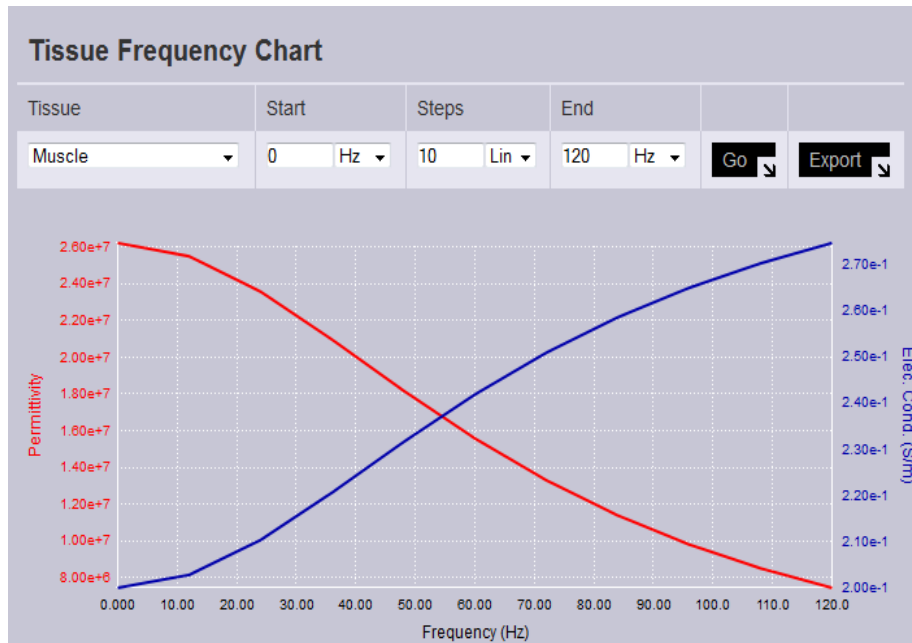Due to investigation the effect of conductivities in different tissues, a concentric multi-layer cylindrical model representing the tissues of the upper limb is simulated in COMSOL multiphysics software (version 4.4). Conductivity and relative permittivity of different tissues from 0 to 1 KHz can be seen in Figure B.1.
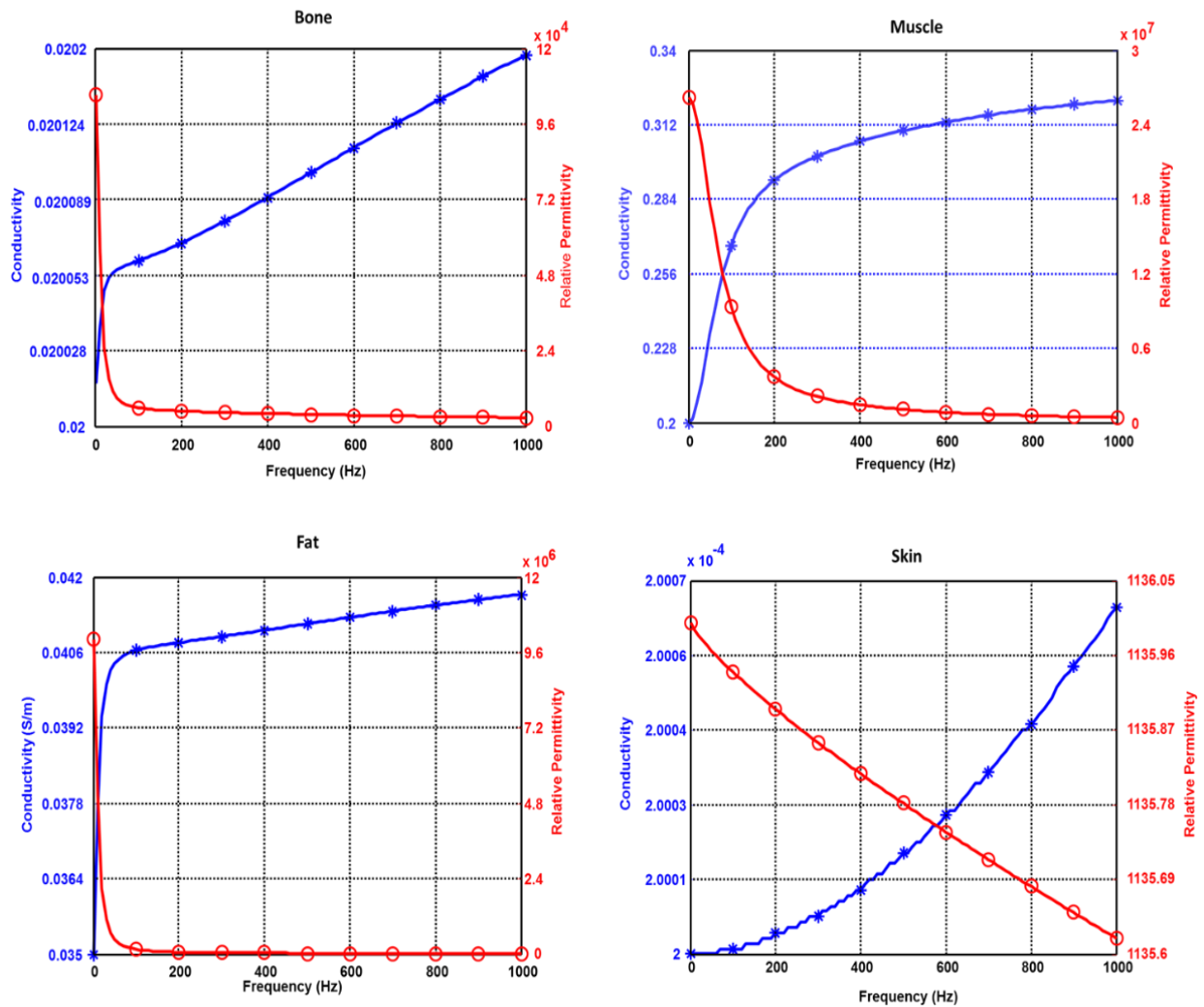


Figure B.1: Conductivity and relative permittivity of different tissues between 0 to 1 KHz frequencies [25]. The red curves illustrate relative permittivity and the blue curves illustrate the conductivity (S/m).

Different values of conductivity for one specific layer were examined while the conductivity values of other layers were the same as the values at the Table B.1. As an example, the conductivity of bone at frequency 100 Hz (the frequency is set to 100 Hz and the relative permittivity is assumed

to be zero) is 0.02 S/m (Table B.1) then the model was examined with 7 different values for conductivity of the bone (from very bigger than 0.02 to the very smaller than the real conductivity value) and the other tissues have the basis conductivities as the mentioned table. The dimensions of different layers, which are demonstrated in the Table B.1, are based on one of our real subjects (Subject No.1).

Table B.1: **(Above):** The dimensions of different layers in concentric multilayer model of upper limb. The term "r_" denotes the radial of the tissues. **(Below):** The current dipole characterization.

| Circumference (cm) | r_Skin (cm) | r_Fat (cm) | r_Muscle (cm) | r_Bone (cm) |
|---|---|---|---|---|
| 30 | Circumference/2*pi | 0.96*(r_Skin ) | 0.75*(r_Skin ) | 0.24*(r_Skin ) |

| radial (rho) (cm) | angular (phi) (deg) | height (Z) (cm) | intensity ($\mu$ A/m) |
|---|---|---|---|
| ((r_Bone+r_Muscle)/2) | 90 | (length_BB*/2)+1 | 0.09 |

A current dipole is positioned at the middle radial of the muscle tissue and 1 mm higher than the middle of the total height. The dipole's characterizations is shown in figure B.2, also, 10 pairs of equidistance electrodes were located over the superficial (skin) layer to record the voltages.

 The distance between consecutive electrodes, also, the distance between each pair electrodes in two different rows are 1.5 cm. The longitudinal distance between each row and the current dipole is 0.75 mm which means the dipole is placed in the middle of the rows respect to the Z axis. Finally, the differential of each pair of electrode at two rows is calculated. Figure B.2 illustrates the model.

The results of different conductivity values can be seen in Figure B.3. It can be found that, with variation of conductivity values for bone and skin layer, the potentials at the electrodes points do not change considerably while for fat and especially for muscle layer varying conductivity values affect the recorded potentials. Effect of various conductivity values for skin tissue is shown in Figure B.3B. The skin layer is the tiniest layer in the model, so variation of conductivity values from $10^{-7}$ to $10^{-3}$ could not considerably change the potentials of the electrodes. However, effect of conductivity values for skin layer is much higher than bone layer. The fat tissue shows more

changes to conductivity values compare with two previous tissues. Since the thickness of fat is not large in our model (4%), then the effect of this layer may not be crucial however, it seems this layer is significant layer in the model. Finally, the most crucial tissue is muscle layer which shows maximum range of potential. This layer is the largest volume in the model and obviously it is more sensitive than the others.
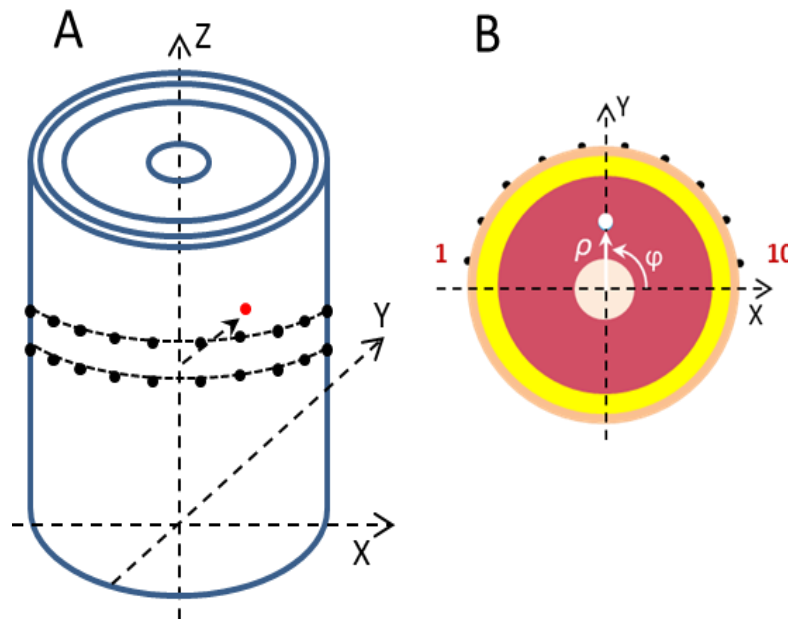


Figure B.2: **A:** Model of the upper limb with four concentric tissues (i.e. bone, muscle, fat and skin). 10 pairs of electrodes located over the skin and a current dipole is put in the center of the med-height the model and at the half radial of the muscle tissue. **B:** the cross section of the model.

To illustrate variations of conductivity values in different way than the next figure (Figure B.3), only electrode number 31, which is the closest electrode to the dipole, was considered in Figure B.4 and logarithmic scale was used.

As it can be seen from Figure B.4A, while the conductivity of bone is varied considerably  from $10^{-7}$ to $10^{-3}$, there is no significant change in potentials recorded by electrodes over the skin layer (potentials varied between 129 and 135 μV). Since the current dipole is located in the middle radius of the muscle layer which is roughly far from the bone layer, so the bone layer does not affect

directly to the electrodes' potentials and it just bounces a tiny portion of the dipole to the skin layer. Therefore, the effect of the bone conductivity is negligible.
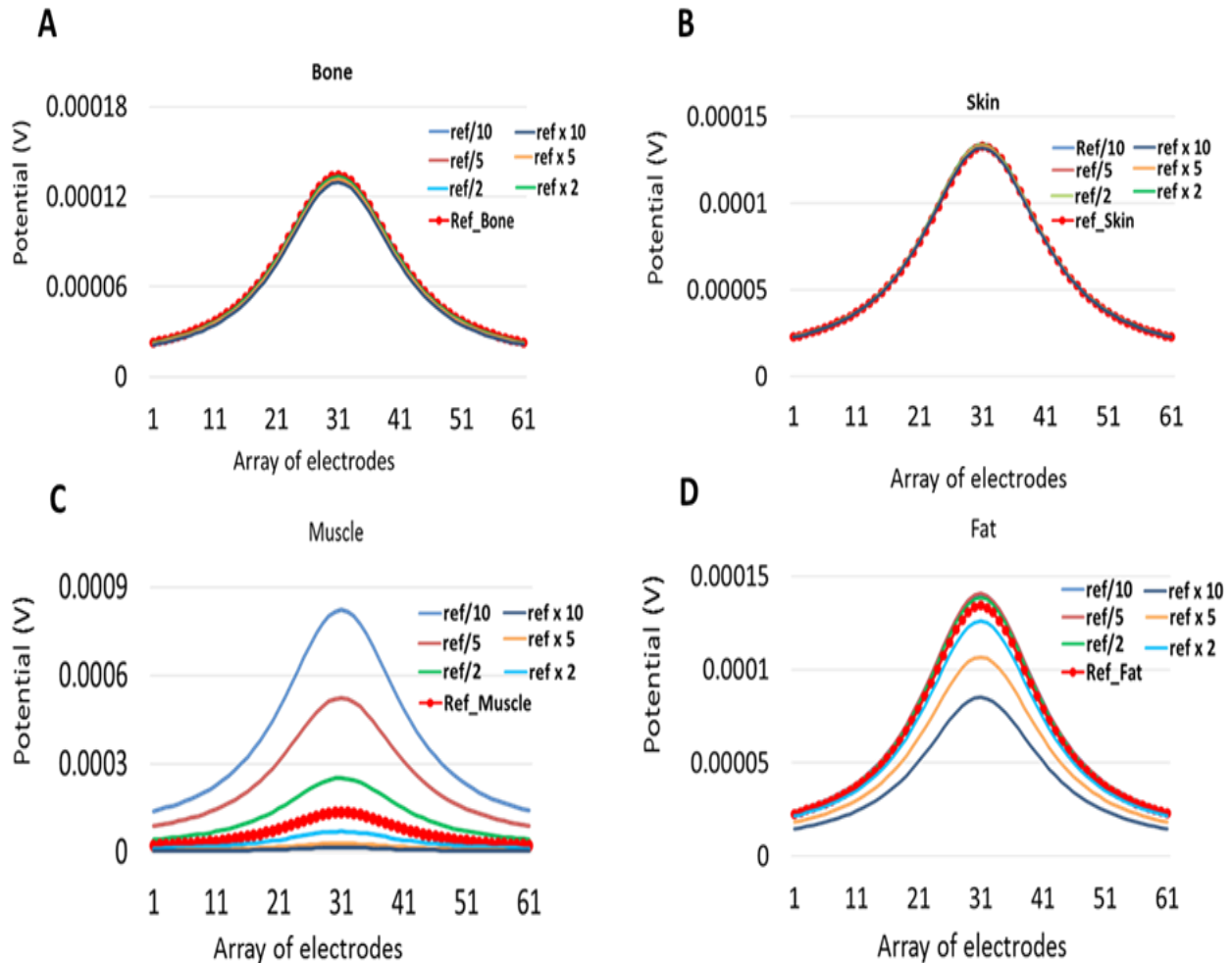


Figure B.3: Effect of different values for conductivity of a specific tissue in a 4-layer model of upper arm. The layers are: bone, muscle, fat and skin. The conductivities of that specific tissue was chosen as: half (ref/2), one fifth (ref/5), one tenth (ref/10), double (ref × 2), five (ref × 5) and ten (ref × 10) times of the basis conductivity value of the tissue. The conductivity of other tissues were fixed as their basis (Table 3.3). The red-dotted curve is result of conductivity of that tissue at 100 Hz as a basis for comparison (these values are lower and higher than the correct value as in Table 3.3). In the legends of the panels, the term "ref" refers abbreviation of "reference" at 100 Hz. Different conductivity values for **A:** Humerus bone. **B:** Skin **C:** Muscle **D:** Fat.
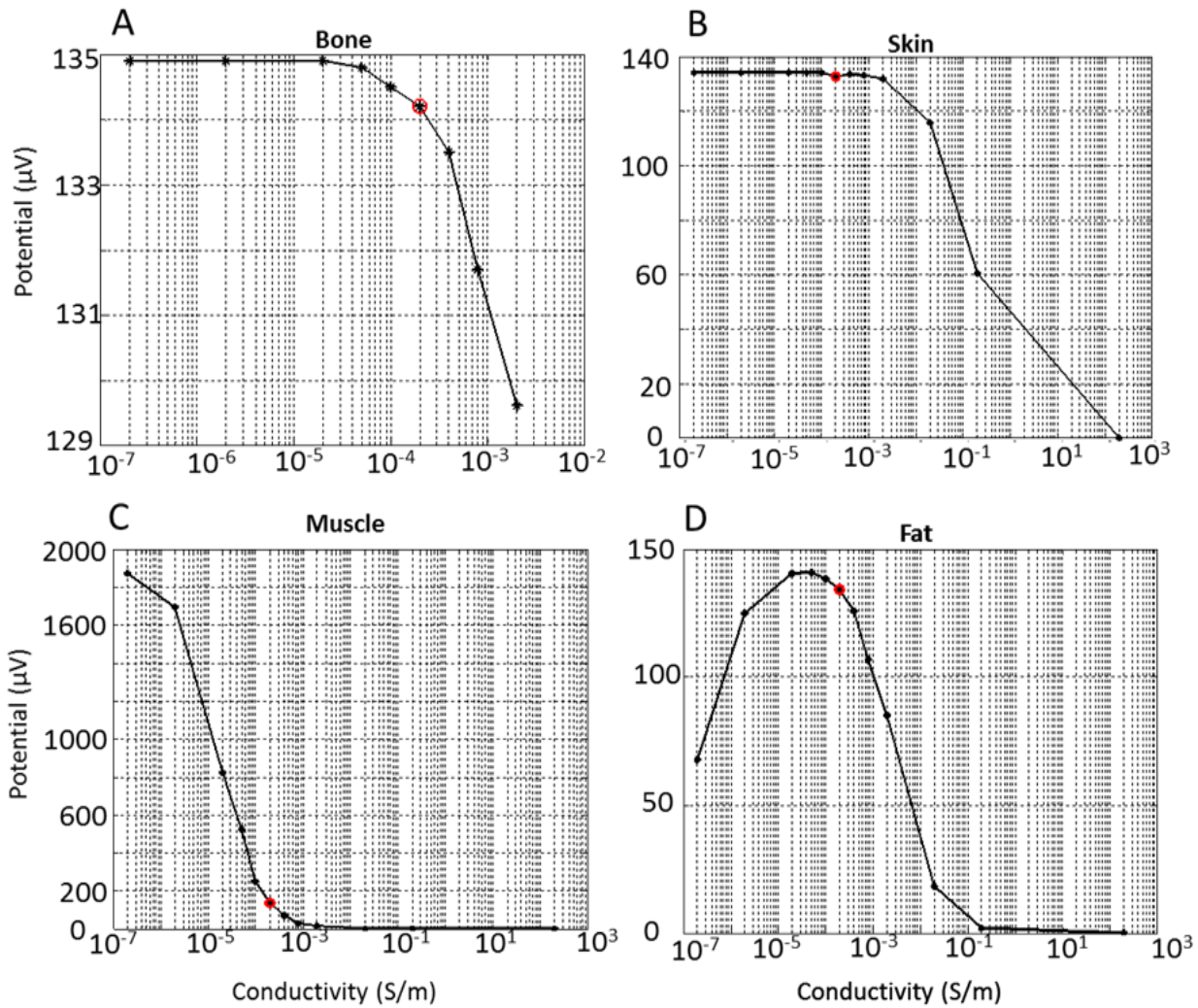
Figure B 4: Different range of conductivity values for a specific layer (**A:** Bone **B:** Skin **C:** Muscle and **D:** Fat) amongst four layers of an upper arm model. The conductivities of that specific tissue was chosen as: half (ref/2), one fifth (ref/5), one tenth (ref/10), double (ref × 2), five (ref × 5) and ten (ref × 10) times of the basis conductivity value of the tissue. The conductivity of other tissues were fixed as their basis (Table 2.1). The red marker specifies the basis value of each tissue at 100 Hz.

# APPENDIX C:  RMS CALCULATION FROM EMG SIGNALS

Samples of 3 EMG signals collected by an electrode pair while the subject was in the seated position with the hand pronated and producing a 20% MVC (maximal voluntary contraction).



Figure C.1 Three consecutive trials of 5 s long EMG signals (electrode pair #2 of subject S2).

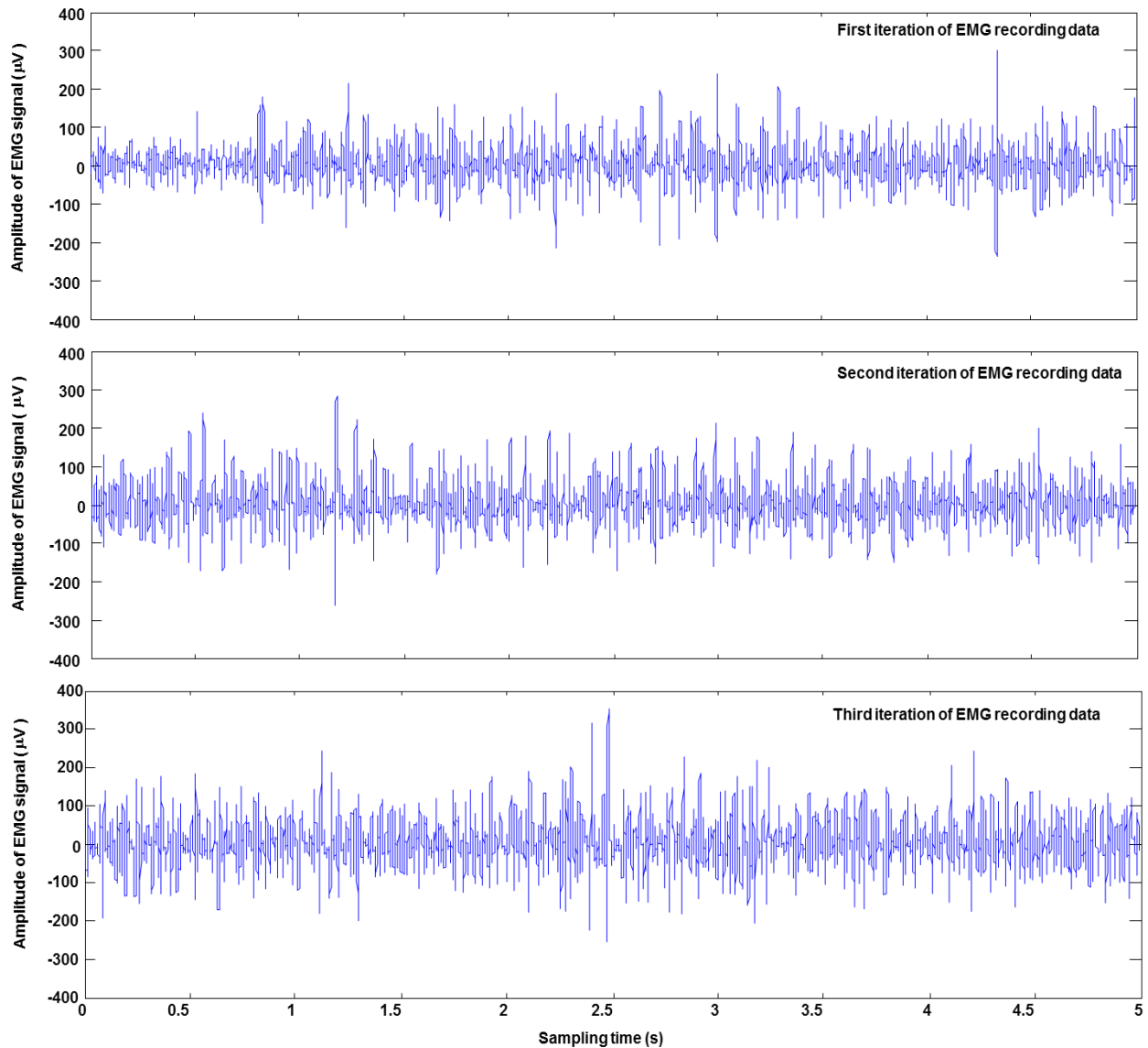RMS values of each of those signals are shown in Table C-1 for the 10 recording sites and their mean values appear at the bottom row. It is those values which are illustrated in Figure 3.2 (p.59).

Table. C.1. RMS values of each repeated EMG experiments with 5 second long and the also the final average of those three RMS values (µV) for each channel.

| Pronation | 1 | 2 | 3 | 4 | 5 | 6 | 7 | 8 | 9 | 10 |
|---|---|---|---|---|---|---|---|---|---|---|
| RMS1 | 49.37 | 47.99 | 36.21 | 29.03 | 36.46 | 26.21 | 28.61 | 19.52 | 16.55 | 17.55 |
| RMS2 | 50.77 | 52.73 | 39.76 | 31.43 | 39.60 | 27.86 | 28.23 | 20.73 | 17.28 | 15.59 |
| RMS3 | 53.81 | 59.07 | 44.01 | 33.29 | 41.30 | 27.36 | 26.60 | 20.61 | 17.39 | 14.56 |
| Average | 51.32 | 53.26 | 39.99 | 31.25 | 39.12 | 27.14 | 27.81 | 20.29 | 17.07 | 15.90 |
| Rounded | 51 | 53 | 40 | 31 | 39 | 27 | 28 | 20 | 17 | 16 |

From the average RMS values, the initial estimation of dipoles characteristics was obtained with the peak fitting method. From the above 10 RMS values distributed around a circle representing the arm, 4 dipoles were identified as shown in Figure C.2 where they are represented by colored circles with a size proportional to their relative intensity (I). Cylindrical coordinates (angular ($\varphi$) and radial ($\rho$)) are used for their positioning.
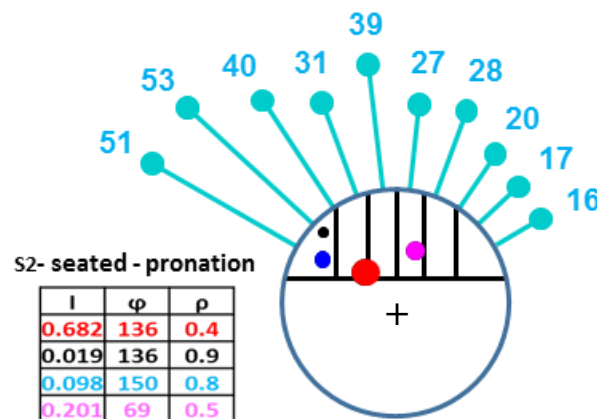


Figure C.2. Upper arm circle model with the BB compartments and dipoles. The RMS values are shown with spokes around the model. Presented at the left, are the dipoles characteristics which were obtained with the peak fitting method.

# APPENDIX D:  POSITION OF ELECTRODES

To examine if the 10 electrodes array was enough to adequately represent the potential distributions associated with the modified position of the dipoles, simulations were done considering that 120 pairs of electrodes were positioned all around the modelled arm. Results obtained for subject #4 are shown in Figure D.1 where it can be seen that the 10 pairs of electrodes placed over the biceps do not miss any main features displayed by the 120 recording sites.
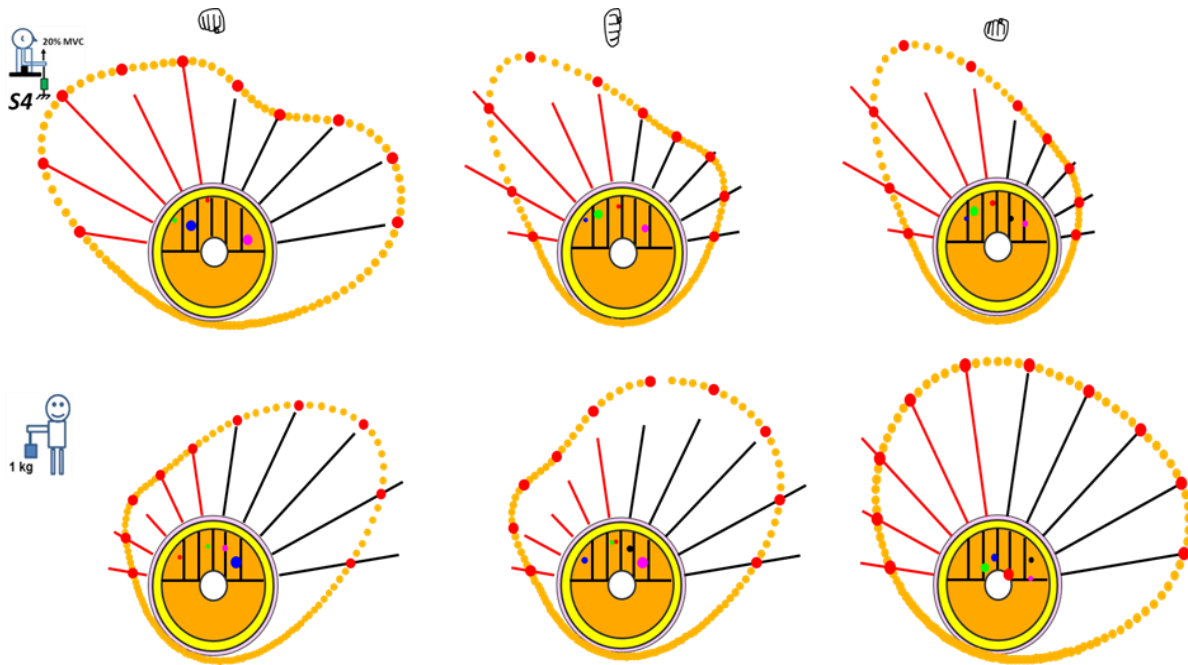


Figure D.1. From the modified dipoles positions, 120 recording sites were considered to examine if additional information would be provided over the one provided by the 10 recording sites used with our subjects. Results with dipoles associated to S4 while seated and standing up with the hand in pronation, neutral or supination are displayed. The orange dots around the outer circle represent 120 potentials equally distributed around the circumference of the cylinder arm model.  The length of the 5 red and 5 black spokes are proportional to the experimental RMS values. Red dots within the orange ones represent the COMSOL simulation results. Colored dots of various dimensions within the yellow circle represent dipoles positions within the muscle tissue.

## APPENDIX E: MATLAB CODES

This MATLAB script is an example of communication between COMSOL and MATLAB to have a better control on COMSOL simulation. To get familiar with local server of the COMSOL and thow to link MATLAB to COMSOL, the best source is webpage of COMSOL. To facilitate the design of our geometrical upper arm model and its modifications, we worked directly in COMSOL. The MATLAB code below was for S1 in the seated position and hand pronated.

```matlab
%% written by Peyman Aghajamaliaval


close all;
clearvars -except model
clc;


%% ****** C O M S O L   LOADING  ********
% mphstart;
% model=mphload('S1_Seated_Pro_ML_iso_VS_aniso_22april2015'); %
Command %to load COMSOL file in MATLAB (server)


% mphsave(model,'S1_Seated_Pro_ML_iso_VS_aniso_22april2015'); % To
save %results



% ModelUtil.disconnect; % disconnect model from server
% ModelUtil.remove('Model1');% Remove model from server while server is
%active


% mphstart(<portnumber>);% activation of the port which is 2036 by default
% list = ModelUtil.tags % to check whether model is in server or not
% mphnavigator;
% help mli

%% parameters used in COMSOL (Based on S1)
model.param.set('circum',   '26.5[cm]',   'Circumference   of   a
Subject');
model.param.set('r_skin', 'circum/(2*pi)');
```

```matlab
model.param.set('r_fat', '1*(0.96*r_skin)');
model.param.set('r_muscle', '0.8*r_skin');
model.param.set('r_bone', '0.24*r_skin');
model.param.set('ZBB', '16.5[cm]', 'BicepceBrachii Length (hight
of %tank');

model.param.set('tita1', '90[deg]-(4.5*tita_center)','Position of first
%electrode');
model.param.set('tita2', '(360[deg])/(circum/1.5[cm])', 'Position
of Electrodes');
model.param.set('Zrow1',  '((ZBB/2)-((1.5/2)[cm]))+1[cm]',  'Z  of
Electrodes Row1');
model.param.set('Zrow2',  '((ZBB/2)+((1.5/2)[cm]))+1[cm]',  'Z  of
Electrodes Row2');

%%*** Peak fitting results(first estimation of Dipoles characteristics **%%
% setting model in MATLAB
% r_skin=10/8;
% rm=0.8*r_skin;
% ro=rm.*[0.7 0.7 0.7 0.8 0.8 0.8];% radius of Dipoles
% Dphi=[96 68 143 31 46 126];% angle of dipoles
% ampD=[0.413 0.248 0.127 0.094 0.067 0.051];
% col_1=[1 0 0]; color code1
% %%%%%%% Ttl3='S1 Seated, Pro, "Peak fitting"';

% commands to load COMSOL
% model.param.set('i1', '0.413*1e-7');
% model.param.set('i2', '0.248*1e-7');
% model.param.set('i3', '0.127*1e-7');
% model.param.set('i4', '0.094*1e-7');
% model.param.set('i5', '0.067*1e-7');
% model.param.set('i6', '0.051*1e-7');
%
% model.param.set('r1', '0.7*r_skin', 'Radial Coord of Dipole
No.1');
% model.param.set('r2', '0.7*r_skin', 'Radial Coord of Dipole
No.2');
```

```
% model.param.set('r3', '0.7*r_skin');
% model.param.set('r4', '0.8*r_skin');
% model.param.set('r5', '0.8*r_skin');
% model.param.set('r6', '0.8*r_skin');
%
% model.param.set('phi1', '96[deg]', 'Angular Coord of Dipole
No.1');
% model.param.set('phi2', '68[deg]', 'Angular Coordof Dipole
No.2');
% model.param.set('phi3', '143[deg]');
% model.param.set('phi4', '31[deg]');
% model.param.set('phi5', '46[deg]');
% model.param.set('phi6', '126[deg]');

%%% ** A f t e r   a d j u s t m e n t   t h e   d i p o l e s **%%%
r_skin=10/8;
k=0.8;
rm=k*r_skin;
ro=rm.*[0.7 0.7 0.7 0.8-0.1+0.1 0.8 0.8];% radius of Dipoles
Dphi=[96 68-10 143 31-25-10 46+10 126+35];% angle of dipoles
ampD=[0.413 0.248 0.127 0.094 0.067 0.051];

% col_1=[0.7 0.2 1];
col_1=[0 0.4 0];

%  %  %%%%%%%Ttl3='S1   Seated,   Pro,r_4-0.1,phi_2-10,phi_4-
%25,phi_5+10,phi_6+35';

model.param.set('i1', '0.413*1e-6');
model.param.set('i2', '0.248*1e-6');
model.param.set('i3', '0.127*1e-6');
model.param.set('i4', '0.094*1e-6');
model.param.set('i5', '0.067*1e-6');
model.param.set('i6', '0.051*1e-6');
```

```
model.param.set('r1',  '0.7*r_muscle',  'Radial  Coord  of  Dipole
No.1');

model.param.set('r2',  '0.7*r_muscle',  'Radial  Coord  of  Dipole
No.2');

model.param.set('r3', '0.7*r_muscle');

model.param.set('r4', '(0.8-0.1+0.1)*r_muscle');

model.param.set('r5', '(0.8)*r_muscle');

model.param.set('r6', '(0.8)*r_muscle');


model.param.set('phi1',  '(96)[deg]','Angular  Coord  of  Dipole
No.1');

model.param.set('phi2',  '(68-10)[deg]','Angular  Coordof  Dipole
No.2');

model.param.set('phi3', '(143)[deg]');

model.param.set('phi4', '(31-25-10)[deg]');

model.param.set('phi5', '(46+10)[deg]');

model.param.set('phi6', '(126+35)[deg]');


%%%%%%%%%%%%%%%%%%%%%%%%%
model.param.set('Zdipoles', '(ZBB/2)+1[cm]', 'Elevation (Z) of all
%Dipoles_Posision');

model.param.set('Zmoment',      '16.5[cm]',       'Moment      of
Dipoles_Direction');



%% Conductivity
model.physics('ec2').feature('cucn1').set('materialType',
'from_mat');


%%%%% ISO SITUATION %%%%%%%%%%%%%
model.physics('ec2').feature('cucn2').set ...
    ('sigma', {'0.26671'; '0';'0'; '0'; '0.26671'; '0'; '0'; '0';
'0.26671'});
```

```
%%%%% ANISO SITUATION %%%%%%%%%%%%
% model.physics('ec2').feature('cucn2').set ...
%     ('sigma', {'0.26671/5'; '0';'0'; '0'; '0.26671/5'; '0'; '0';
'0'; '0.26671'});


model.physics('ec2').feature('cucn2').set('sigma_mat',
'userdef');
model.physics('ec2').feature('cucn2').name...
    ('Current Conservation (anisotropy property of Muscle)');


%% Commands to execute COMSOL from MATLAB
model.geom('geom2').run; % Geometry loading
%
% %model.mesh.create('mesh2', 'geom2'); % mesh generating
% % model.mesh('mesh2').feature.create('ftet1', 'FreeTet');
%  model.mesh('mesh2').feature('size').set('hauto',  1);%changing
the %mesh
% % size;1==Extremly fine, 2==extra fine, 3==finer, 4==fine,...
model.mesh('mesh2').run;


model.sol('sol1').runAll; % if solver does not converge, then
soloutin %should be updated by command below.
model.sol('sol1').updateSolution;


%% Input Data
circum=26.5; %%%%circumference of subjects'arm
RMS=[13 17 19 21 30 27 29 23 18 19];% RMS values of S1


%% reading data (tables) from COMSOL
% % model.result.table.create('tbl3', 'Table');
% % model.result.table('tbl3').comments('Row1 (V2)');
% model.result.numerical('pev2').selection.set([2 7 9 14 20 47 51
55 57 62]); % reading electrodes in COMSOL mesh
% model.result.numerical('pev2').selection.set([2 7 9 15 20 47 51
55 57 62]); % reading electrodes in COMSOL mesh
```

```matlab
% model.result.numerical('pev2').set('probetag', 'none');

model.result.numerical('pev2').name('Row1');

model.result.numerical('pev2').set('solrepresentation',
'solnum');

model.result.numerical('pev2').set('table', 'tbl3');

model.result.numerical('pev2').setResult;

Row1 = (model.result.table('tbl3').getRealRow(0))'; % Row #1 of
%electrodes

Row1=Row1(2:end);% First column is frequency values (100HZ)



% % model.result.table.create('tbl4', 'Table');

% model.result.table('tbl4').comments('Row2 (V2)');

% model.result.numerical('pev3').selection.set([3 8 10 15 21 48 52
56 58 63]);

% model.result.numerical('pev3').selection.set([3 8 10 16 21 48 52
56 58 63]);

% model.result.numerical('pev3').set('probetag', 'none');

model.result.numerical('pev3').name('Row2');

model.result.numerical('pev3').set('solrepresentation',
'solnum');

model.result.numerical('pev3').set('table', 'tbl4');

model.result.numerical('pev3').setResult;

Row2 =(model.result.table('tbl4').getRealRow(0))'; % Row

Row2=Row2(2:end);


%% Design of Diferent layers i.e. Skin, Fat, Muscle and Bone

Npts=1000; % Number of points to show circle

theta=linspace(0,2*pi,Npts);

theta=theta(1:end-1); %0 and 2*pi are same so 2*pi is neglacted


% radias of different circle

rs=10/8;% Superficial Circle rSkinrs=rs

rm=0.8.*rs;%Muscle r2

rb=0.2*rs;%rBone r3
```

```
rf=0.96*rs;%rFatr r4


% cordinate of circles
x1=rs.*cos(theta);
y1=rs.*sin(theta);
x2=rm.*cos(theta);
y2=rm.*sin(theta);
x3=rb.*cos(theta);
y3=rb.*sin(theta);
x4=rf.*cos(theta);
y4=rf.*sin(theta);


d2r=pi/180; % degree tp radian or command: phirad=degtorad(phi);
r2d=180/pi; % radian to degree
```

%% Electrodes`s  locations.  Matlab  works  with  radian  so  degree should %be

```
%converted to the radian
ElecDist=1.5;           %Distance between two Electrodes
%circum=26.5;           %circumference of subjects'arm
r=circum/(2*pi);        %radial of subjects'arm
ElecAngl=ElecDist/r;  %angle between two Electrodes respoct to the
radial of the subject's arm
AngDeg=ElecAngl*r2d;  %changing the angle to the degree
HalfDeg=4.5*(AngDeg); %there are 5 electrodes in Lh and SH so the
%total  angle  up  to  LH,SH  border  becomes  4  and  half  degree  of
distance %between Electrodes
Offsetdeg=(90-HalfDeg)/2; %half from zero degree and half from 180
%degree
phi=linspace(0+Offsetdeg,180-Offsetdeg,10); %angles of electrodes
on %the superficial circle
phirad=phi.*d2r;        %angles in radian
xphi=cos(phirad);
yphi=sin(phirad);
```

```matlab
%% Processing of Data (Voltages) came From Simulation(COMSOL) &
%Experiments
% Nurmalization of Voltages
% Data interval will nurmalized between [1.2:3.2]
MinNurm=1.2;% Minumun of output
MaxNurm=3.2;% Maximun of Output
% Nurmalisation of RMS
% RMS=[];
MaxRMS=max(RMS);
MinRMS=min(RMS);


RMS_array=zeros(1,length(RMS));
for pq=1:length(RMS)
RMS_array(pq)=MinNurm+((RMS(pq)-MinRMS)*(MaxNurm-
MinNurm)/(MaxRMS-MinRMS));
end


%Nurmalisation of Simulation data from COMSOL
% Row1=[];
% Row2=[];
Diff_abs=abs(Row1-Row2);
MaxRows=max(Diff_abs);
MinRows=min(Diff_abs);


Max2Min_simulation=(MaxRows-MinRows);


Sim_array=zeros(1,length(Diff_abs));
for p=1:length(Diff_abs)
Sim_array(p)=MinNurm+((Diff_abs(p)-MinRows)*(MaxNurm-
MinNurm)/(MaxRows-MinRows));
end


RMSNurms=RMS_array(end:-1:1);
```

```
SimNurms=Sim_array(end:-1:1);  %changing the electrodes'order as
Prof. %Mathiue Jornal
```

```
%% Comparing RMS and Simulation

Diff_R1R2=Diff_abs';

Dif=(RMSNurms(end:-1:1)-SimNurms(end:-1:1))';%difference between
Experimental and Simulation

% RootMeanSq=rms(Dif)

RootSumSq=rssq(Dif)/10;

num=rssq(Dif);

dinum=rssq(RMSNurms);

ErNorm=(1/10)*(num/dinum)
```

```
%% *********Data to Excle file***********
%% Titles
% filename='Mat2Excl';
% % A0={'Er','ErNorm'};
% sheet=1;
% % xlrange1='Q4';
% % xlswrite(filename,A0,sheet,xlrange1)
% % B0={'Dif(R1,R2)'};
% % xlrange2a='E7';
% % xlswrite(filename,B0,sheet,xlrange2a)
% % B1={'Dif(Exp,Sim)'};
% % xlrange2b='E8';
% % xlswrite(filename,B1,sheet,xlrange2b)
% %% data2Excle
% % Error and Error Normalized
% A1={RootSumSq,ErNorm};
% xlrange1='Q10:R10';
% xlswrite(filename,A1,sheet,xlrange1)
% % dif(r1r2)
% xlrange3='F9:O9';
% xlswrite(filename,Diff_R1R2',sheet,xlrange3)
```

```matlab
% % dif(exp,sim)
% xlrange4='F10:O10';
% xlswrite(filename,Dif',sheet,xlrange4)
%% Design of Dipoles Locations


Dphi_rad=Dphi.*d2r;% degree to radian converter
DNumbr=length(ro);%numner of Dipoles
xdipoles=zeros(1,DNumbr);
ydipoles=zeros(1,DNumbr);
for j=1:DNumbr
xdipoles(j)=ro(j).*cos(Dphi_rad(j));
ydipoles(j)=ro(j).*sin(Dphi_rad(j));
end
%% Plots
figure;
plot(x1,y1,'LineWidth',1.5);
hold on
plot(x2,y2,'LineWidth',1);
plot(x3,y3,'LineWidth',1);
plot(x4,y4,'LineWidth',1);
deg1=acos(rb*sin(pi/8)/rm);
a1=[rb*cos(pi/8)          rm*cos((pi/2)-deg1)];b1=[rb*sin(pi/8)
rb*sin(pi/8)]; %right horinzontal line
a2=[rm.*cos(pi/2)          rb.*cos(pi/2)];b2=[rm.*sin(pi/2)
rb.*sin(pi/2)];%middle vertical
a3=-a1;b3=b1;
a4=[rm*cos(0.9845)          rm*cos(0.9845)];b4=[rb*sin(pi/8)
rm*sin(0.9845)];%angle=0.9845radian==>56.4077deg
a5=[rm*cos(1.30268)          rm*cos(1.30268)];b5=[rb*sin(pi/8)
rm*sin(1.30268)];%angle=1.30268radian==>74.6381deg
a6=[rm*cos(1.5708+(1.5708-1.30268))          rm*cos(1.5708+(1.5708-
1.30268))];
b6=[rb*sin(pi/8) rm*sin(1.5708+(1.5708-1.30268))];
a7=[rm*cos(1.5708+(1.5708-0.9845))          rm*cos(1.5708+(1.5708-
0.9845))];
b7=[rb*sin(pi/8) rm*sin(1.5708+(1.5708-0.9845))];
```

```
line(a1,b1,'color','black','LineWidth',3.5);%right    horinzontal
line

line(a2,b2,'color','black','LineWidth',3.5);%middle vertical

line(a3,b3,'color','black','LineWidth',3.5);%left     horinzontal
line

line(a4,b4,'color','black','LineWidth',3.5);% most right vertical
line

line(a5,b5,'color','black','LineWidth',3.5);

line(a6,b6,'color','black','LineWidth',3.5);

line(a7,b7,'color','black','LineWidth',3.5);


% Electrodes and their amplitudes

for i=1:5

X=[rs.*xphi(i)  RMSNurms(i).*rs*xphi(i)];%**

Y=[rs.*yphi(i)  RMSNurms(i).*rs.*yphi(i)];%**

line(X,Y,'LineWidth',3.5,'Color',[0 0 0])

%
plot(RMSNurms(i).*rs.*xphi(i),RMSNurms(i).*rs.*yphi(i),'MarkerSiz
e',17,...

%       'Marker','.','LineStyle','none')

end

for i=6:10

X=[rs.*xphi(i)  RMSNurms(i).*rs*xphi(i)];%**

Y=[rs.*yphi(i)  RMSNurms(i).*rs.*yphi(i)];%**

line(X,Y,'LineWidth',3.5,'Color',[1 0 0])

%
plot(RMSNurms(i).*rs.*xphi(i),RMSNurms(i).*rs.*yphi(i),'MarkerSiz
e',17,...

%       'Marker','.','LineStyle','none')

end

col=[1 0 0;0 1 0;0 0 1;1 0 0.5;1 0.5 0;0 0.5 0.3];% different
colors for dipoles

% simulation results

for i=1:10

% X1=[SimNurms(i).*rs.*xphi(i) RMSNurms(i).*rs.*xphi(i)];%
```

```
% Y1=[SimNurms(i).*rs.*yphi(i)  RMSNurms(i).*rs.*yphi(i)];%
%             line(X1,Y1,'LineWidth',3,'LineStyle','--','Color',[0
0.498039215803146 0]);


plot(SimNurms(i).*rs.*xphi(i),SimNurms(i).*rs.*yphi(i),'MarkerSiz
e',25,...
    'Marker','.','LineStyle','none','color',col_1);%
0.498039215803146
end
% %Dipoles Plots
for l=1:length(ampD)
plot(xdipoles(l),ydipoles(l),'MarkerSize',15+30*ampD(l),'Marker',
'.','LineStyle','none','Color',col(l,:));
end
axis([-4.5 4.5 -2 4.5]);
axis equal
hold off
% % % axis off
% % % grid
%% Plots
figure(2);
plot(x1,y1,'Color',[0 1 0],'LineWidth',1);
hold on
% simulation results
for i=1:10
plot(SimNurms(i).*rs.*xphi(i),SimNurms(i).*rs.*yphi(i),'Marker','
hexagram',...
    'MarkerSize',10,'MarkerFaceColor',[1              1
1],'MarkerEdgeColor',[0 0 0],...
   'LineWidth',1.45,'Color',[0 0 0]);
end
axis([-4.5 4.5 -2 4.5]);
axis equal
hold off
```